Towards Detection of User-Intended Tendon Motion with Pulsed-Wave Doppler Ultrasound for Assistive Hand Exoskeleton Applications

by

Kelly J. Stegman

B.Sc. Honours (Physics and Astronomy), University of Victoria, 2007
Diploma (Physics), Camosun College, 2003

A Thesis Submitted in Partial Fulfillment
of the Requirements for the Degree of

MASTER OF APPLIED SCIENCE

in the Department of Mechanical Engineering

© Kelly Stegman, 2009

University of Victoria

Supervisory Committee

Towards Detection of User-Intended Tendon Motion with Pulsed-Wave Doppler Ultrasound for Assistive Hand Exoskeleton Applications

by

Kelly Stegman

B.Sc. Honours (Physics and Astronomy), University of Victoria, 2007
Diploma (Physics), Camosun College, 2003

Supervisory Committee

Dr. Edward J. Park, Department of Mechanical Engineering
Co-Supervisor

Dr. Ronald P. Podhorodeski, Department of Mechanical Engineering
Co-Supervisor

Dr. Nikolai Dechev, Department of Mechanical Engineering
Departmental Member

Abstract

Current bio-robotic assistive devices have developed into intelligent and dexterous machines. However, the sophistication of these wearable devices still remains limited by the inherent difficulty in controlling them by sensing user-intention. Even the most commonly used sensing method, which detects the electrical activity of skeletal muscles, offer limited information for multi-function control. An alternative bio-sensing strategy is needed to allow for the assistive device to bear more complex functionalities. In this thesis, a different sensing approach is introduced using Pulsed-Wave Doppler ultrasound in order to non-invasively detect small tendon displacements in the hand. The returning Doppler shifted signals from the moving tendon are obtained with a new processing technique. This processing technique involves a unique way to acquire raw data access from a commercial clinical ultrasound machine and to process the signal with Fourier analysis in order to determine the tendon displacements. The feasibility of the proposed sensing method and processing technique is tested with three experiments involving a moving string, a moving biological beef tendon and a moving human hand tendon. Although the proposed signal processing technique will be useful in many clinical applications involving displacement monitoring of biological tendons, its uses are demonstrated in this thesis for ultrasound-based user intention analysis for the ultimate goal of controlling assistive exoskeletal robotic hands.

Supervisory Committee

Dr. Edward J. Park, Department of Mechanical Engineering
Co-Supervisor

Dr. Ronald P. Podhorodeski, Department of Mechanical Engineering
Co-Supervisor

Dr. Nikolai Dechev, Department of Mechanical Engineering
Departmental Member

Table of Contents

List of Tables

List of Figures

Acknowledgments

First and foremost, I am extremely grateful to my supervisors Dr. Ed Park and Dr. Ron Podhorodeski. Their expertise, guidance, mentorship and patience were essential to the success of this research. Words cannot describe how thankful I am to be given the opportunity to work on such an interesting project and to ultimately contribute my expertise to help those with disabilities.

I would also like to express my gratitude to Dr. Nick Dechev. His kind words, inspiring discussions and encouragement over the years have been pivotal to my success.

A special thanks to Ed Haslam for his technical wizardry, positive spirit and support.

I am also forever grateful to my fiancé Jason Brooks, to whom this work and all my love is dedicated to.

Last, but certainly not least, I wish to express my thanks to my friends, my family and my lab colleagues for their unwavering support.

Chapter 1

Introduction

The present idea of wearable robotics stems from historical artificial limbs, which were mostly used as a supplement for balance and cosmetic appearance. The earliest artefacts discovered were two Egyptian toes (a wooden toe and a paper-mache toe) dating from as early as c.664 BC, and a Roman bronze leg from c.300 BC (Figures 1A, B). During the 15th and 16th centuries, many soldiers lost their limbs during battle and consequently they wore iron prosthetic arms, hands and legs afterwards. A French army surgeon, Ambroise Pare, is attributed to the design and implementation of the first mechanical hand, arm and articulated knee joint (Figures 1C - E) [1]. Lighter, wooden prosthetics soon followed during the Civil and World Wars along with advances in antiseptic and anaesthesia techniques (Figure 2A). These wars first introduced devices with artificial tendons and then emphasized creating life-like prostheses by using new plastics and computer aided design after World War II [2].

Recently, robotic industrial grippers are being designed to mimic the hand's anatomy [3, 4]. This is because the traditional end-effector tools are designed specifically for a task (or a family of similar tasks). Thus, different types of tools would be required in order to pick up various parts. It would be much more convenient to design a flexible hand robot to pick up various items by reconfiguring itself, instead of a rack of tools being constantly interchanged. These hand-like robots would be most useful in high precision or semi custom manufacturing (Figure 2B), and in biomedical applications such as a mobility extension on a wheelchair or testing software [4].

(A)   (B)
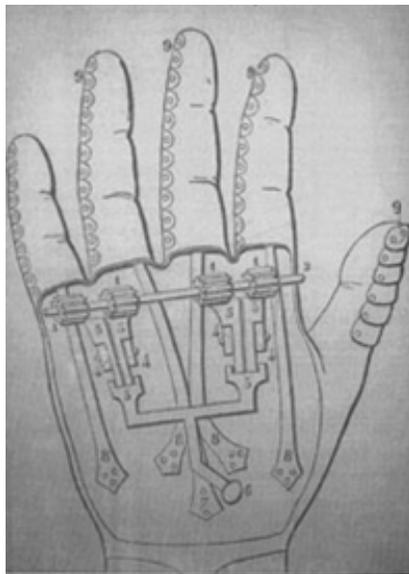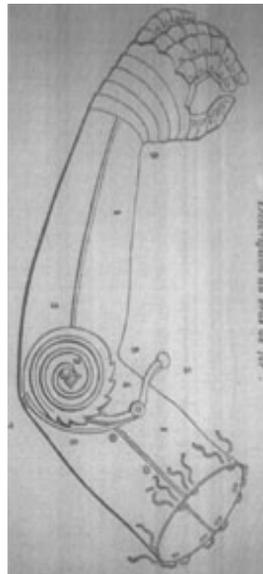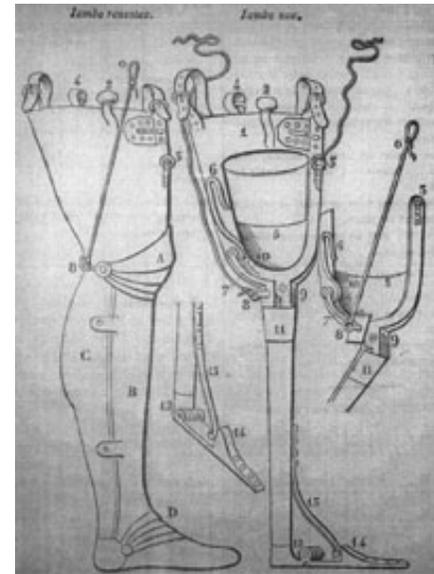
(C)   (D)   (E)

Figure 1: (A) Egyptian toe prosthesis c.664BC [5], (B) Roman bronze leg prosthesis (copy) [6], and a 16th century hand (C), arm (D) and leg prostheses (E) designed by Ambroise Pare [7].
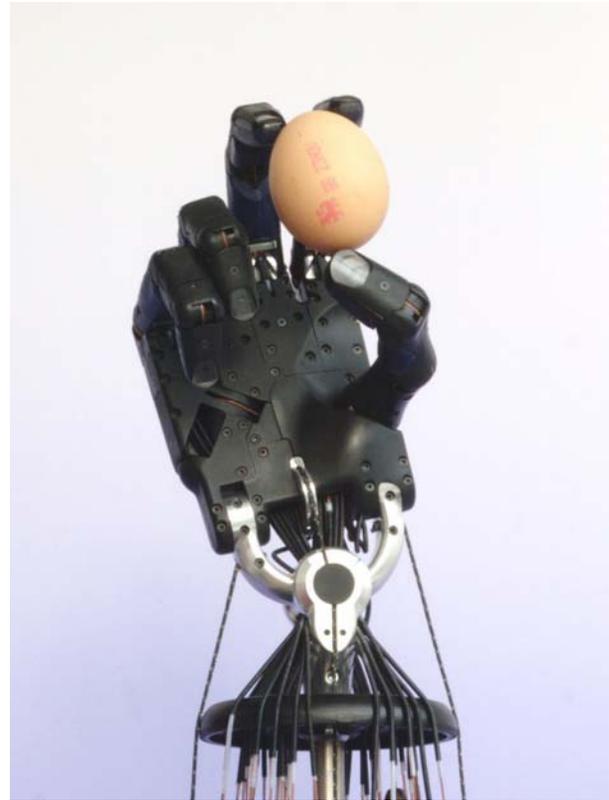
(A)   **(B)**
Figure 2: (A) Civil War Leg Prostheses circa 1865 [7], and (B) the Shadow Hand dexterous manipulator [8].

Although prosthetic devices have been introduced as early as ancient Egypt, exoskeletons have a much later history. First conjured up for fictional stories in the 1930's, the actual development of a light-weight and compact usable exoskeleton system has only recently been initiated [9-19]. Although the research in this area is limited, the increasing amount of reported hand injuries and disorders demonstrates a growing need for such an assistive device. These assistive devices serve as a general mobility aid by enabling the disabled and elderly to remain independent for longer periods (Figure 3). This may in turn help relieve the strain on the healthcare systems and help restore a significant quality to the lives of those affected. Such a permanent wearable device would have significant promise for use with hand injuries, reduced motor function, musculoskeletal disorders, and post stroke therapy of the hand.

In terms of hand injuries, it has been shown that the stiffening of the hand joints and muscles was lessened when motion exercises were used more frequently [20-21]. Also, approximately 795,000 people suffered a stroke in the United States alone last year

with about two-thirds of this group surviving the incident, but with many resulting issues in hand mobility [14, 17, 22-23]. The exoskeletons uses for those with easily fatigued hands could also range from astronauts losing muscle mass on long space flights to other musculoskeletal disorders such as early ALS (Amyotrophic Lateral Sclerosis) and MS (Multiple Sclerosis), as well as certain spinal fractures and work place injuries. In regards to work-related hand injuries, according to a WorkSafe BC study, injuries to fingers and hands ranked the highest in workplace incidents (more than 40% in 2006) [24]. This is an average of 14,500 hand injuries that is reported in BC per year, with 1 in 7 being work-related. These work-related hand injuries cost approximately $6,000,000/year for healthcare and worker benefits to compensate over 50,000 lost workdays per year.

Most of these disabled or injured people solely rely on rehabilitation therapists for treatment. However, due to a disproportionate ratio of patients to therapists, patients are often only seen once or twice per week. More frequent hand activity of patients would certainly be more beneficial, and this is where an assistive device for the hand will be useful. Unfortunately, most analogous mechanical devices on the market are rather large and rehabilitative in nature which makes it difficult to extend this technology for the purpose of assisting activities of daily living (Figure 4).
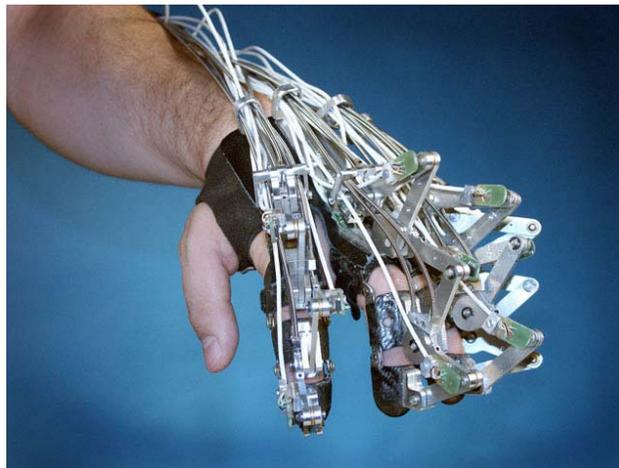
Figure 3: An assistive exoskeleton device for the hand [19].

Figure 4: The Hand Mentor ^{TM} from Kinetic Muscles Inc. is a rehabilitative hand exoskeleton used for therapeutic treatment [25].

The successful design of a wearable hand robot includes safety assessment, comfort, ease of use and interaction with the environment, mechanism optimization and most importantly, control strategies. Surprisingly, existing hand exoskeletons and prosthetics are generally less capable than that of service industrial robots. This is largely due to the man-machine interface and control problem. This fundamental task is quite daunting to many engineers because every mechanical design has the same problem of figuring out how the device can sense user intention to control the wearable robot. Real-time intention recognition by sensing a user and its environment is thus a very important function for man-machine interaction. Topics related to vehicle sensors, energy management, virtual reality, military/security and biomedical applications, all require research into this fundamental topic in order to perfect the human-machine interface [26-32].

Using the natural body as a sensing mechanism is an elegant solution to enhance the usability and functionality of wearable robots. These bio-sensors take advantage of the natural control processes which are optimized in humans (reasoning, planning and executing) in order to clearly identify user intention. On the other hand, mechanical sensing can reveal important information about positions, motions and forces which are crucial in control and design planning of wearable robots, and are often used in

conjunction with bio-sensors. Currently, electromyographic (EMG) signals dominate the bio-sensing market to detect user intention, while electroencephalography (EEG) or magnetoencephalography (MEG) signals are thought to be the future of user intended control. Other bio-sensing control methods to detect user intention may include myokinemetric (MK) signals, mechanomyography (MMG) signals, electrooculograpic (EOG) signals, voice-recognition control, tendon activated pneumatic (TAP), and ultrasonic sensing.

1.1   Thesis Objectives

The primary goal of the research presented in this thesis is to introduce a novel sensing strategy which uses Pulsed-Wave Doppler ultrasound for detecting user intended hand grasping. This new bio-sensing strategy is developed here specifically for the future application of hand exoskeleton control for persons with some residual hand function. In particular, the following **objectives** of this research are defined:

1)   To determine the difficulties in the current strategies to sense user intention for bio-robotic control, based on a thorough literature review.

2)   To identify the anatomical and functional capabilities of a healthy hand in order to determine an optimal sensing strategy to restore some of the motor abilities in disabled patients.

3)   To develop an original sensing strategy using Pulsed-Wave (PW) Doppler ultrasound to detect the velocity and displacement of a moving tendon in the wrist for the eventual use on an assistive exoskeleton.

4)   To develop a signal processing technique to test the feasibility of this new bio-sensing method.

5)   To perform three experiments in order to test the accuracy of the new signal processing technique. These experiments include:

(i) accurately measuring the small velocity and displacements of a moving string,

(ii) accurately measuring the small velocity and displacements of a moving beef tendon, and

(iii) accurately measuring the small velocity and displacements of a human

biological tendon and demonstrating the control of a robotic finger test-bed using the acquired measurements.

6)   To comment on the implications of the experimental results and the ability to expand into future works.

1.2   Thesis Contribution

Overall, the ability to detect tendon motion with Doppler ultrasound has significant academic contributions to current research in bio-robotic control and other medical sciences. Intended contributions to current research include:

- Improving a method to non-invasively detect tendon motion and to quantify the tendon displacements,

- Introducing a method to acquire and process raw Doppler signals from a commercial ultrasound machine,

- Providing a novel sensing approach by using user-intended tendon motion for the eventual use of assistive hand exoskeleton control.

1.3   Thesis Organization

This thesis is divided into 10 chapters in order to address the above research objectives, and is outlined as the following. In Chapter 1, the background of wearable robotics, prostheses, exoskeletons and control strategies are introduced. The project objectives are also outlined in order to show the structure of this thesis. In Chapter 2, a literature review of the control strategies that are currently used for sensing user intention are described in detail. In Chapter 3, a healthy hand's anatomical and functional structure is described in order to understand the hand's capabilities and limitations. Chapter 4 describes the physics of ultrasound. This chapter forms the basis to understand the background of the new bio-sensing method presented in this thesis. Chapter 5 describes the ultrasound device components and signal processing for Duplex Imaging. In Chapter 6, the proposed techniques and methodology of the three experiments are outlined. In Chapter 7, the displacement measurement accuracy test for the string and beef tendon is described in detail. In Chapter 8, the robotic finger demonstration using the proposed

processing technique is described in detail. Chapter 9 provides a discussion of the research presented in this thesis. In Chapter 10, conclusions are drawn concerning the feasibility of this new bio-sensing idea and the future potential is discussed.

Chapter 2

Background: Sensing User Intention

In order to implement a wearable assistive exoskeleton, a sensing and control strategy must be optimized. As previously stated, there exist several anatomically correct and sophisticated industrial robotic hands which are controlled by computers to perform pre-determined tasks. However, they cannot be used as a wearable assistive device for humans because there is no current way of detecting user intention to fully control these multi-DOF (degree-of-freedom) machines. Current bio-sensing methods which detect user intention include using electromyographic (EMG) signals, electroencephalography (EEG) signals, magnetoencephalography (MEG) signals, myokinemetric (MK) signals, mechanomyography (MMG) signals, electrooculograpic (EOG) signals, voice-recognition control, tendon activated pneumatic (TAP), and ultrasonic sensing.

2.1 Electromyography (EMG) Control

Electromyography (EMG) is a technique used in the medical industry, in which an electrode is inserted into the body to record and evaluate physiological properties of muscles while in motion and at rest. It is often used by neurologists to detect the electrical potential generated by the muscle cells in order to determine if certain pathologies exists. The electric potential of muscles was first documented by Francesco Redi in the late 1600's using an electric ray fish, and has evolved to be used in many clinical and biomedical applications [33].

Surface EMG signals have been used to non-invasively detect user intention to control bio-robots such as prosthetics [2, 32]. The surface EMG sensors are non-invasively placed on suitable muscle sites on top of the skin. These sensors can detect the onset of a voluntary muscle contraction in order to control a wearable robot. In order to use this control method, the EMG signals need to be acquired from suitable muscle sites, the signal needs to be pre-processed, dimensionally reduced and feature extracted. Finally, the pattern for motion intention must be recognized in order to implement a

prosthetic robot [34]. Successfully using the EMG signal for prosthetic hand control will depend on the level of amputation or disability, signal strength and the fatigue level of the muscle (because the EMG signal changes with fatigue) [35].

Current commercially available hand prosthetics use EMG signals to provide very few practical degrees-of-freedom (DOF), mainly from the flexion and extension of the upper arm muscles to open and close the robotic hand [2]. Extensive signal processing efforts are currently researched to gain extra information from the EMG signal to improve the DOF using time-frequency domains, wavelet analysis, neural network and fuzzy classification [15-18, 34-36]. The resulting DOF are still inadequate to fully control a prosthetic; however they are commercially acceptable and have dominated the market. Considered the most advanced commercial prosthetic hand, the iLIMB™ hand has individually powered digits, built in detection for sufficient grip and locks into place until the open signal is triggered [2]. Due to the EMG signal limitations, the user must manually position the thumb in two different positions in order to change between the key and pinch grips. Other EMG-controlled hand prosthesis is the OttoBock Sensor Hand™ [37], FluidHand™ [38] and the Southampton Hand™ [39]. Although these hands mainly differ by weight, materials, speed, and touch sensors, they are still limited by low DOF based upon detecting the EMG signal from the user.

EMG prosthetic control technology has been extended into rehabilitative and assistive exoskeletons. In particular, even though several EMG lower extremity exoskeleton designs have been successively launched, hand exoskeletons still remain quite bulky. The same underlying issues still exist with hand exoskeletons because the EMG signal is usually taken from the extrinsic muscles which are responsible for many different hand configurations. Due to the low DOF available with EMG control, many designs involve developing hybrid systems in order to gain more information about user intention [40-41]. The EMG controlled exoskeletons which are used for rehabilitation do not have the same design constraints as assistive systems. Because of this, rehabilitative systems can be bulkier in size and can have more suitable EMG sites on the limb [17, 25].

2.2 Electroencephalography (EEG) and Magnetoencephalography (MEG) Control

Electroencephalography (EEG) is a non-invasive technique to measure the electrical activity produced by the brain and is often used by neurologists in behavioural and seizure testing. In a typical surface EEG, electrodes are placed on the scalp with a conductive gel and the consequential signal is digitized and filtered. The resulting wave can reveal any abnormalities in brain function, and is thus a useful tool for clinicians. EEG technology is also used in creating brain-computer interfaces (BCI) to be used in biomedical fields and gaming industries [42-48]. Perhaps the most interesting of EEG devices are those being developed at Duke University Medical Center by Miguel Nicolelis and other collaborators. Using electrodes implanted on a monkeys brain, the monkey successfully controlled an exoskeleton arm to reach for food by the monkeys own thoughts. Later, the monkey was able to control a robot to mimic its motions on a treadmill with its own brain. Although this technique is invasive, it is an impressive demonstration of wearable robot technology [43]. Conceivably even more inspiring is the bio-robot being developed at the University of Reading. It is solely controlled by a biological brain made from cultured brain neurons from a rat. These 50,000 to 100,000 active cultured rat neurons are placed onto a multi electrode array (MEA) with about 60 electrodes which pick up the generated signals from the cells. When the robot nears an object, these signals are directed by electrodes to stimulate the brain. The responded brain output is then used to drive the wheels of the robot or steer left and right to avoid hitting the object. The next step is to determine if the brain can learn and remember [48].

Magnetoencephalography (MEG) signals are often used in conjunction with EEG signals to complete a more accurate data set to be used as control for the brain-machine interface (BMI). MEG is an imaging technique used by clinicians and researchers to measure the magnetic fields produced by electrical activity in the brain. The main difference in quality between EEG and MEG signals is that magnetic fields are less distorted by the resistive properties of the skull and cap [49]. One study compared simultaneous EEG and MEG recordings of hand motions, and decoded the signals with a 67% success rate [50]. Although these results are promising, the accuracy of the decoded

signal is not coherent enough to fully control a wearable robot. In addition, MEG or EEG systems are expensive and require long training periods for accurate system calibration and repeatable results.

2.3   Myokinemetric (MK) Control

The use of myokinemetric signals (MK) was first documented in 1999 as a solution to the limitations of using EMG signals to solely control a wearable robot [51,52]. Myokinemetric signals are derived from measurements in the dimensional changes in the muscle normal to the skin during contractions. This signal is measured using a socket-located Hall Effect based transducer. With errors of about 10%, amputee subjects were able to follow a series of trajectories, hence showing promise in potentially controlling a fully functional prosthetic. Recent contributions have started to compare EMG and MK signals for degree of control, and the results are still pending [52]. Currently, there is no published research in MK exoskeleton control which may merit further investigation; however, there is still questionable information on whether multi-functional control is even possible with MK signals.

2.4   Mechanomyography (MMG) Control

Mechanomyography (MMG) is the study of the sound that is generated by the muscles during contraction which represent muscle dimensional changes. It is widely researched for kinesiology purposes in determining muscle fatigue and muscle responses [53-55]. MMG control is limited in wearable robotic technology because it is very sensitive to external factors like muscle temperature, outside noise, skin fold thickness and sensor attachment [56-59]. Even with these problems, a MMG-based prosthesis was successfully controlled with 2 DOF, which shows significant insight to other control methods not currently used in the commercial market [56].

2.5   Electrooculograpic (EOG) Control

Electrooculograpic (EOG) is the electrical signal produced by the potential difference between the highly electrically-active retina and cornea of the eye [60]. EOG

technology has been used to control a prosthetic eye to mimic the movements of an existing healthy eye, and in prosthesis control for patients with serious spinal injuries [61-62]. Because devastating spinal injuries leaves few voluntary actions available, EOG signals from eye gaze direction were measured and used as bio-control to move a robot arm [62]. This non-verbal control method shows promise in severely injured or disabled people to control prosthetic limbs and equipment in order to participate in daily tasks.

2.6   Voice-Recognition Control

Usually used for high-level spinal injured patients, voice-controlled prosthesis and rehabilitation equipment have shown to improve the quality of life and independence of those affected. Prosthetics, exoskeletons and wheelchairs have shown to be controlled by 80 words or more, and are proven successful in operating difficult tasks like writing and controlling orientation [63-65]. Voice control has also been used in toy robots [66-67], communication controls in cars [26], as well as surgical equipment control [68]. The main issue with voice activation systems is non-recognition because of similar sounding words. Sometimes other languages are adopted for more sophisticated control, or a smaller vocabulary is used [63].

2.7   Tendon Activated Pneumatic (TAP) Control

First documented in 1999, Tendon Activated Pneumatic (TAP) control sensors are pneumatic sensors that are placed in the socket of a prosthetic arm to detect residual tendon motion for multi-digit control [69]. The sliding motion of the residual tendon causes soft tissue displacement between the skin and the socket, and the measured resulting pressure differential was used to demonstrate binary or proportional prosthetic control. TAP sensors were noted to fail if the tissues were too fatty or damaged and are limited to residual tendon function. Over the last decade, few updates were available from using TAP sensors, and have yet to be fully implemented in an exoskeleton or fully functional prosthetic device [70].

2.8   Mechanical Sensor Control

Mechanical sensing is often used in conjunction with other user detection control sensors to complete the desired task for the wearable robotic device. The all-important human-robot interface uses these sensors in order to drive an action, provide feedback and can monitor the status of the device. Knowing the angular and linear joint displacements, velocities, accelerations, forces, torques and pressures are fundamental requirements in properly controlling a wearable robot. These sensors can include encoders, magnetic sensors, potentiometers, electrogoniometers, MEMS inertial sensors, accelerometers, gyroscope, piezoelectric sensors & polymers, capacitive force sensors, strain gauges and pressure gauges [2, 17, 71-74]. Although these sensors have useful properties, they should not be used to solely detect user intention to control an assistive exoskeleton. For example, these sensors can detect when a joint is starting to rotate through an angle which can be interpreted as user intention, since the targeted market for this device has this ability. However if there was resistance detected by a shape, bend, touch or force sensor, there would be no way to confidently determine whether the person just had stiff joints while the exoskeleton was in motion, if the person wanted to stop the exoskeleton motion, or if the persons fingers touched the object with sufficient grip to stop the motion. Not being able to uniquely determine the difference between these actions can be dangerous, hence a conjunction of mechanical and bio-sensors should be used for ultimate exoskeleton control.

2.9   Ultrasonic Control

Ultrasonography is a non-invasive imaging technique used in the medical industry in which high sound frequency is transmitted through the body and is then reflected off of tissue boundaries. This is a safer imaging technique than X-ray or CT (computed tomography) scans because it does not use ionizing radiation; it uses high-frequency sound, which has little effect on the body. Some literature reports side effects such as local heating, a tendency to have left handed offspring, as well as an ill effect on the brains of mice when exposed to long, high frequency ultrasound. Inconclusive evidence of brain malformation has been reported for humans [75-79].

A typical ultrasound set up includes a computer connected to a transducer probe which emits high frequency (1-20 MHz) sound waves into the body. These sound waves travel until they hit a boundary between tissues, where some of the waves reflect back to the probe, while the rest continue on until another boundary is encountered. The reflected waves that are detected by the probe are relayed to the computer, where the probe-boundary distance is calculated in order to display the image or perform other user specified applications.

The transducer probe works by using the piezoelectric effect, which was first discovered by the Curies in 1880. When an electric current is applied to piezoelectric crystals, they rapidly change shape and vibrate. These vibrations produce sound waves that travel outwards. These crystals also emit electric currents when a sound wave hits them, so they can be used to send waves and detect incoming waves.

Ultrasound devices contain many different modes for imaging and software settings for different applications. Early sonography started with the 1-D (1-Dimensional) A-scan, and progressed to include the 2-D B-Scan, 3-D imaging and Doppler imaging. The use of ultrasound for medical diagnostic purposes has been used since the early 1950's. Regarded as an early pioneer in ultrasonography, Dr. John Wild developed a prototype one dimensional (A-mode) ultrasound device and successfully imaged the colon. He subsequently expanded to 2-D (B-mode) ultrasound imaging and published many papers on imaging brain tumours and living tissue structures. Ultrasound imaging was later extended to include Doppler imaging in the 1970s and 1980s and 3-D imaging towards the 1990s. With recent developments in software and computing power, biomedical ultrasonography is the more popular, least invasive and economical choice for most diagnosticians. Medical ultrasound technology is usually used in general imaging, blood flow measurements, strain measurements, needle guided anaesthesia, stabilizing the moving ultrasound machine by means of a manipulator, kinesiology, and surgery [80-84].

2.9.1   A-Scan Ultrasound

In the original 1-D scanner, the A-Scan plots the amplitude of the reflection on the y axis against time on the x axis as the wave is reflected through the tissue boundaries

(Figure 5). This type of ultrasound is obsolete, as it can be inaccurate and computationally time consuming. This is because the probe has to be located in the proper area of interest, which may not be obvious from the body surface. If the imaged object is moving, Doppler shifts of these lines would have to be computed, which often uses inefficient methods like cross correlation to track the line shift [41]. A-Scan ultrasonography has shown uses in ophthalmology, where the absence or deformation of a peak may represent a certain eye ailment [85].

2.9.2 B-Scan Ultrasound

The 2-D B-Scan is the most common type of ultrasound. The machine displays the probe-boundary calculated distances and intensities of the echoes as a 2-dimensional greyscale pie-shaped image on the screen (Figures 6, 7 A and B). B-Scan images are taken and displayed in real-time, and are often saved in video format for later retrieval. Recently, researchers have developed 3-D ultrasound imaging which uses a rotating probe, 2-D B-scans and special software to combine images. The images are quite remarkable, and can better detect smaller features (Figure 8).
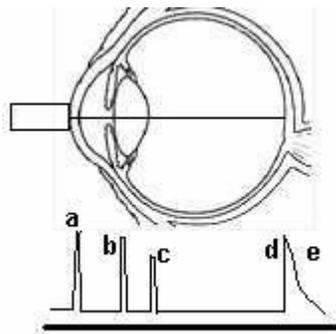
Figure 5: A-Scan of the eye [85].

Figure 6: B-Scan image of the vascular system [86].
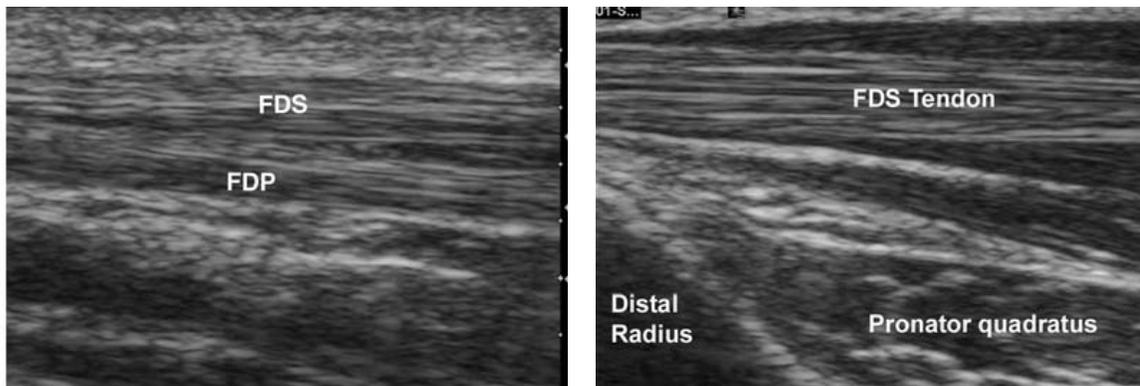
(A)   **(B)**

Figure 7: (A) Comparison image taken with a 13 MHz linear array probe for the flexor (FDS and FDP) tendons in the wrist, and (B) the FDS tendon and hand muscle [87].

Figure 8: 3D Ultrasound imaging [88].

2.9.3   Doppler Functions

Most ultrasound systems that can display a B-Scan image usually have Doppler imaging to determine the presence or absence of flow, velocities and displacements. When ultrasound waves are reflected from a moving surface, the frequency is shifted revealing information on the velocity of the moving object. This "Doppler Effect" is successfully used for calculating blood flow and other tissue motion [89-97]. Common Doppler functions on a clinical ultrasound machine include Continuous Wave Doppler (CW), Pulsed Wave Doppler (PW) and Duplex Doppler imaging.

Continuous Wave Doppler (CW) devices continuously emit and receive ultrasonic signals using a double element transducer (Figure 9). These instruments do not have range discrimination and any movement in the sensitive regions contribute to the Doppler shift. Thus, blood motion from a vessel as well as tissue motion is displayed simultaneously. These machines are generally less expensive than other Doppler devices, and are typically used to detect the presence of a fetal heart beat or other motion occurrences.

Unlike a CW instrument, Pulsed Wave (PW) Doppler devices transmit pulses of ultrasound and then switch to receive mode (Figure 10). The received signal is gated, so only relevant information at the desired depth is used. A PW output plot usually shows velocity (or Doppler frequency) of the sampled region as a function of time. From this spectral plot, the mean velocity, peak velocity, displacements and envelope curve can be displayed depending on the software.
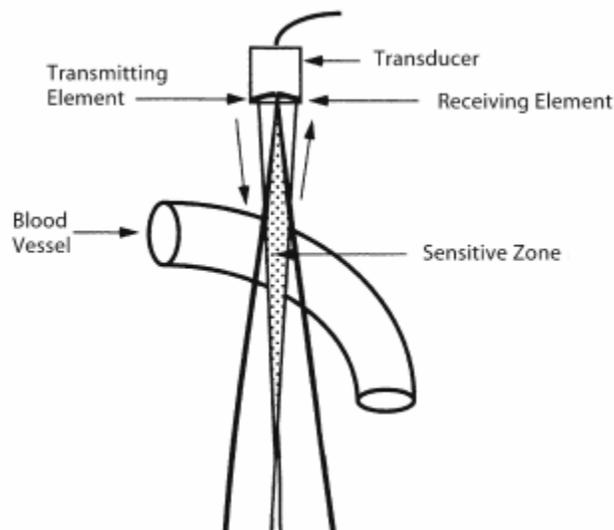
Figure 9: Continuous Wave Instrument [98].
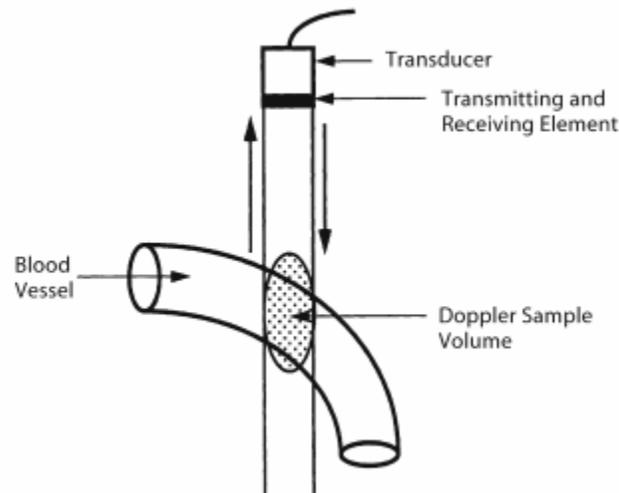
Figure 10: Pulsed Wave Instrument [98].

2.9.4   Duplex Imaging

In order to successfully locate the region of interest and sample volume, Duplex Doppler imaging is used (Figure 11). A duplex system combines real time B-Scan images with Doppler capabilities by superimposing a scan line and gate on the image. This will ensure proper sample volume detection and accurate velocimetric quantifications.

Figure 11: Duplex Imaging with the B-Scan above and PW Doppler plot below [86].

Obtaining quality B-Scan images are important in order to accurately determine where to measure the velocity for the PW Doppler function. In order to optimize a B-Scan image and PW Doppler spectra data, several constraints are investigated. For B-

Scan images frequency, gain, dynamic range, depth, focus position, and focus number along with different presets are explored; while gate, angle correction, pulse repetition frequencies, aliasing and wall filter are considered for PW Doppler spectra. These parameters are defined as the following:

Frequency: Trades penetration depth for sensitivity and resolution; i.e., the higher the frequency, the shallower the depth that can be successfully imaged.

Gain: Increases or decreases the amount of echo in the image by brightening or darkening the image.

Dynamic Range (DR): Controls how the echo intensities are converted to shades of grey.

Focus position, #: Allows user to move the focus zones to better focus the image.

Gate, Angle Correct Line, and Vector Line: Referring to Figure 12, a vector line, gate and angle correction line are superimposed on the B-Scan image. The vector line starts at the probe and moves out radially. The cursor moves the gate and angle correction around the image. The gate is used to select a sample volume in which only the velocities of the moving tissues which lie between the gate lines is displayed. For the case of hand tendons, this is made as small as possible (1 mm) using the ultrasound machine's software. The angle correct line is the angled line intersecting the vector line and projecting through the gate. This line should be pointed in the direction of tendon flow, so that it accurately measures velocities flowing at that specific angle. However, because only velocity components moving towards the probe or away from the probe can be measured, the angle correct line must not be around 90 degrees.
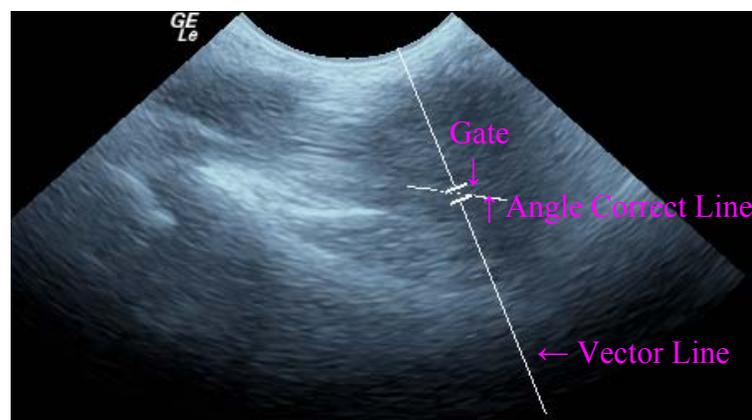
Figure 12: Screen shot showing the gate, angle correction and vector line.

Pulse Repetition Frequency (PRF): Adjusts the velocity scale to allow for faster or slower moving tissue.

Aliasing: The maximum Doppler frequency, f_D, that can be measured is half of the sampling or pulse repetition frequency (PRF). If the $v(cos\theta)$ term in the Doppler frequency formula (Equation (13) from Chapter 4) gives a Doppler shift frequency, f_D, value greater than half of the PRF, ambiguity occurs. This effect can also be seen in western movies where the wagon wheel appears to move backwards due to the low frame rate of the film.

Wall Filter: Removes the noise caused by vessel or heart wall motion at the expense of low flow velocity.

2.9.5   Sensing User-Intention with Ultrasound

Because ultrasonography can image moving tissue in real time, it also has the potential to be used for controlling an upper limb prosthetic device. This concept is demonstrated in the literature by using an ultrasound system to detect the thickening of a forearm muscle when the wrist extends and flexes in normal subjects, and when the forearm muscle is flexed in amputees [40]. In this case, the forearm muscles motion was taken with a B-Scan ultrasound, and the data was later analyzed. A tracking and matching algorithm had to be employed offline in order to track the muscle changes from each B-Scan image frame. Although this technique was not in real time, it resulted in correlating the muscle tissue deformation as a function of the wrist angle. A simpler approach was later employed, using a hybrid system consisting of a 1-D A-Scan ultrasound sensor and an EMG device [41]. The hybrid system was supposed to be a more economical approach; however a B-Scan ultrasound system had to be initially employed in order to locate the proper forearm muscle before positioning the A-Scan transducer. Also, skeletal muscles work as a group to perform certain motions, and only one muscle was investigated in this study. Thus, it may be difficult to extend this sensing idea to control a multi-functional device. EMG and 1-D ultrasound sensor position are also reported to be difficult to place when the muscles investigated were small. Although several issues were noted, both experiments showed a correlation between muscle deformation and

wrist contraction angle, which showed promise in sensing user intention for eventual prosthetic control.

2.10   Comparison of Intention Recognition Methods

Over the years, electromyographic (EMG) devices have become the best solution for non-invasive control. However, despite all of these efforts, EMG prosthetics and exoskeletons are limited by many processing and usability difficulties. Many researchers have reported complications with detecting the onset of movement correctly as well as processing issues to avoid signal cross-talk [34]. There are also many limitations with the overall usability of the robot because of the high level of training required. This usually results with low productivity, low degrees of freedom and user fatigue. Commercially available devices recognize these issues and have explored EMG hybrid systems in attempts to extract additional degrees of freedom for more sophisticated devices. Because of the noted issues, using EMG sensors for our purposes of controlling an assistive exoskeleton would not be an appropriate solution.

Using a brain controlled neuroprosthesis is perhaps the most sophisticated solution to restorative treatment. These devices are controlled by sensing the user's electric (EEG) and magnetic (MEG) brain activity to recognize intention. Overall, EEG signals are presently not an effective solution for prosthetic and exoskeleton control. This is because non-invasive techniques require long training periods and provide relatively low information and invasive methods are still in its research infancy. Invasive EEG measurements are not a suitable control solution because the targeted users in our research are otherwise fairly mobile and wouldn't likely undergo such extreme necessary surgery. EEG, MEG, EOG and voice activation control systems would be most suited for severely handicapped patients, who require these techniques to gain independence and mobility.

Other intention recognition sensors like MMG, MK and TAP control are innovative sensing methods, but they do not show significant merit in multi-functional control. This is because the published results are either too inaccurate or only suited for certain amputees or situations. Also, mechanical sensors are usually included for a hybrid system and it would not suffice to use them alone to sense user intention.

As demonstrated in [40] and [41], ultrasound signals can be used to detect muscle thickening which showed promise in detecting user intention. It would be inadequate to measure muscle deformation to control an exoskeleton because the same extrinsic muscles are used for different hand motions. The resultant exoskeleton would need multiple sensors on several different extrinsic and intrinsic muscle sites in order to interpret user intention for uniquely defined hand motions. This design would not be low-profile or computationally efficient because all of the ultrasonic information would have to be combined in real time to implement an exoskeleton. Also, the extrinsic muscles which produce individual finger movements are not functionally subdivided [99]. That is, the extrinsic muscles in the forearm are not separated into parts which define individual finger motions. This would ultimately lead to a low degree of freedom device because of the lack of available sensing information. This problem resembles the same fundamental limitation that EMG controlled prosthetics and exoskeletons have.

2.11   A New Approach to Assistive Hand Exoskeleton Control

Doppler ultrasonic sensing has never been presented in the literature to potentially control an assistive exoskeleton. In this thesis, an improved real-time approach to Doppler ultrasonic sensing is developed for intention recognition to ultimately control a multi-functional hand assistive exoskeleton. Our requirements for a novel exoskeleton design include real-time sensing of tendon motion from small user intended motions of the disabled and weak fingers. These tendons, which are used for flexion in the fingers, have a maximum displacement in the longitudinal direction during finger joint motion [100]. These flexor tendons are also attached to individual joints in the hand. Due to this, ultrasonic measurements of these flexor tendons can be used for real-time sensing of user intention in uniquely defined hand motions. These tendons are located in the same geographic area, which will make multiple sensing easier. The original idea presented in this thesis uses B-Scan and Pulsed-Wave (PW) Doppler ultrasound. This is because PW Doppler can focus on a small desired area of the B-Scan and output the velocity of this area in real time. Once the velocity of the active tendons is above a certain threshold, the exoskeleton motion can be implemented.

Previous ultrasonic prosthetic control studies have used B and A-Scan ultrasound imaging coupled with lengthy offline image tracking analysis techniques to reveal a correlation between muscle deformation and wrist angle [40, 41]. These studies did not actually test this method on a prosthetic device. Also, ultrasonic imaging of the flexor tendons has been discussed intensely in carpal tunnel disorder and hand surgery research. Many of these research groups also write flow tracking algorithms which track how an object on a B-Scan ultrasound image moves between frames. However, some of their approaches do not have the ability to locate and track an object in real time, have a low tracking success rate or require initial tracking intervention from a user [101-105]. A-Scan measurements have shown to be able to track motion by looking at the peak shifts; however, for a tendon moving perpendicular to the image plane, no motion would be detected. Also, it could be difficult to accurately determine which peak corresponds to which moving areas on A-Scan images.

In order to present the new Doppler sensing protocol in this thesis, the following chapters explore the hand's physical and functional anatomy, describe the properties of ultrasound and PW Doppler processing, and finally demonstrating the feasibility of this approach by performing three experiments.

Chapter 3

The Anatomical and Functional Structure of the Hand

In order to successfully create an assistive hand exoskeleton, the designer must fully understand the capabilities of the patient. Knowing the hand anatomical structure and possible joint articulations, along with the types of grips and grasps which can be restored, allows the designer to create an assistive device which maximizes the ability of the patient.

3.1   Physical Anatomy

3.1.1   Bones and Joints:

The normal human hand contains 27 bones, having 14 of them in the phalanges of the fingers [106]. There are 8 carpal bones in the wrist, 5 metacarpal bones in the main body of the hand, and 14 bones in the phalanges of the fingers and thumb (Figure 13). The fingers have three phalanges (proximal, intermediate and distal phalanges), while the thumb has two (proximal and distal) phalanges. There are also small Sesamoid bones that are usually found near the bases of the metacarpal bones in the phalanges or in the wrist which provide extra tendon leverage to reduce pressure on the underlying tissue. There are four joints in each of the fingers: CMC (carpometacarpal), MCP (metacarpophalangeal), PIP (proximal interphalangeal) and DIP (distal interphalangeal) joints. The thumb has the CMC, MCP and the IP (interphalangeal) joints. The CMC joints lie between the carpals and metacarpal bones, the MCP joints lie between the metacarpals and the phalanges, and the IP joints (proximal, intermediate and distal) lie between the phalanges (respectively). The CMC joint in the thumb is considered a saddle joint with 2 degrees-of-freedom (DOF), the MCP joints in the fingers and thumb are considered condyloid and 'hinge-like" joints (respectively) each with 2 DOF, and the IP joints of the fingers and thumb are hinge joints with 1 DOF [107].

Although there are some variations on the anatomy, like additional fingers or metacarpal bones, the typical average length of an adult male hand is 189 mm with a breadth of 84 mm, while the average length for the adult female hand is 172 mm with a breadth of 74 mm [108]. Other measurements are available in Table 1.
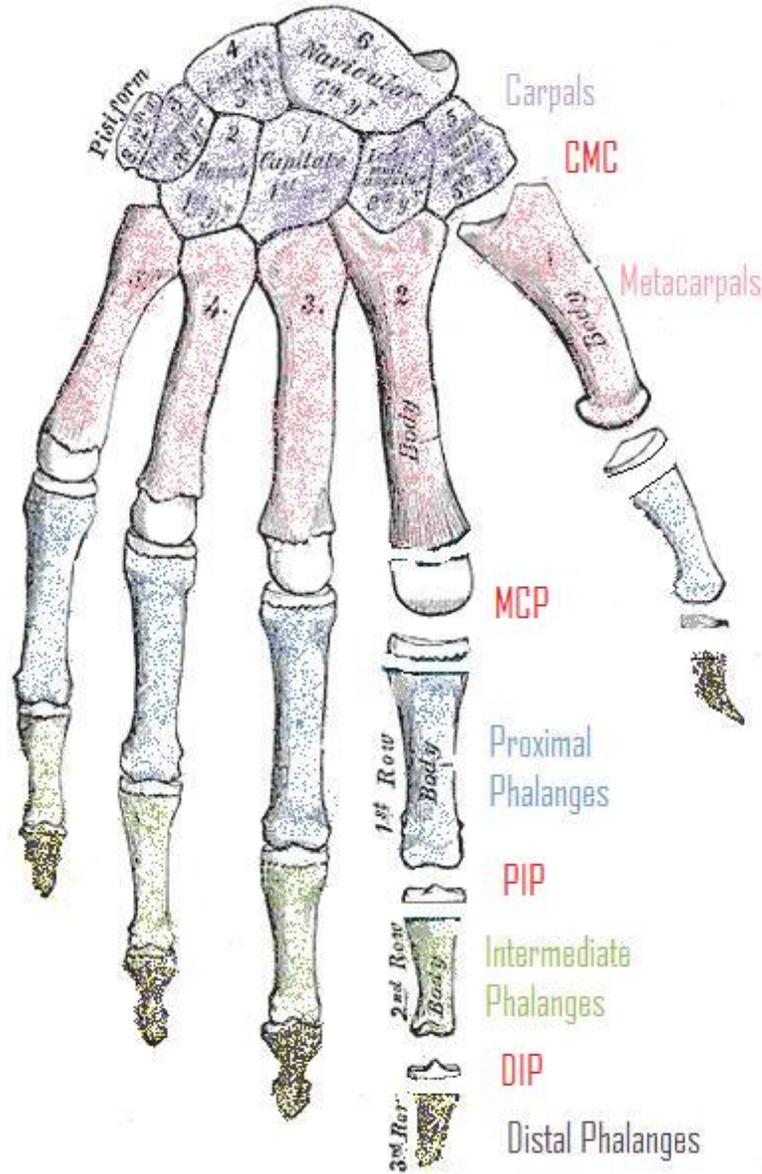
Figure 13: The bones and joints in the human hand. Adopted from [109].

Table 1: Phalange lengths as a percent of hand length for males and females [106].

Phalanx	Proximal	Medial	Distal
Thumb	17.1	-	12.1
Index	21.8	14.1	8.6
Middle	24.5	15.8	9.8
Ring	22.2	15.3	9.7
Little	17.7	10.8	8.6

3.1.2 Muscles & Tendons:

Skeletal muscles move bones by attaching to either side of a joint in order to actively contract and shorten. A second set of muscles is required to return the limb to its original position, because the reverse action is not possible with soft tissues. Therefore some muscles called agonists act as primary movers while others, usually on the other side of the joint, act as antagonists counteracting and opposing the motion. Because of this, typically one set of muscles is active while the opposite set is relaxed [106]. The muscles which produce finger motion are divided into intrinsic and extrinsic groups depending on their origin. The smaller intrinsic muscles originate in the hand, and provide precise coordination for the fingers (Table 2). These muscles are classified into three groups: thenar, hypothenar and midpalmer muscle groups. The thenar muscles include the abductor pollicis brevis, opponeus pollicis, flexor pollicis brevis and adductor pollicis. The hypothenar group refers to the palmarus brevis and the abductor, flexor and opponeus digiti minimi muscles. The midpalmer group consists of the lumbricals as well as the dorsal and palmer interossei.

Table 2: Intrinsic muscles of the hand [106].

Group	Name	Nerve	Function
Thenar Muscles	Abductor pollicis brevis	Median	Abducts Thumb
	Opponens pollicis	Median	Pulls thumb to little finger
	Flexor pollicis brevis	Median	Flexes thumb
	Adductor pollocis	Ulnar	Adducts thumb
Hypothenar muscles	Palmaris brevis	Ulnar	Folds skin on ulnar side of palm
	Abductor digiti minimi	Ulnar	Abducts little finger
	Flexor digiti minimi	Ulnar	Flexes little finger
	Opponens digiti minimi	Ulnar	Pulls little finger toward thumb
Midpalmar muscles	Lumbriclas	Median, Ulnar	Flex proximal phalange
	Dorsal interossei	Ulnar	Abduct fingers
	Palmar interossei	Ulnar	Adduct fingers

The larger extrinsic muscles originate in the forearm and mainly provide strength (Table 3). These muscles divide into flexor tendons on the anterior (palm) side of the forearm and extensor tendons on the posterior side of the forearm. The flexor tendons of the fingers include the flexor digitorum superficialis (FDS) and the flexor digitorum profundus (FDP), which attach to the base of the intermediate and distal phalanx, respectively (Figure 14-16). The flexor tendons of the thumb are the flexor pollicis brevis and longus which attach at the base of the proximal and distal phalanges, respectively. The extensor tendons of the fingers include the extensor digitorum tendon which attaches to the base of both the intermediate and distal phalanges of the fingers and the extensor indicis which attaches to the extensor digitorum of the index finger. The extensor digitorum tendons are also connected to each other by bands on the middle and ring fingers. The extensor pollicis brevis and longus attach to the thumb at the base of the proximal and distal phalanges, respectively. Tendons, like ligaments and cartilage, are part of the connective tissue group which transmit forces and provides structural integrity to the musculoskeletal system. Tendons are primarily composed of parallel bundles of collagen fibres, with non-linear stiffness characteristics and with a modulus of elasticity of 0.94 GPa [110].

Table 3: Extrinsic muscles [106].

Group	Name	Nerve	Function
Anterior, Superficial	Flexor carpi radialis	Median	Flexes and adducts hand
	Palmaris longus	Median	Flexes hand
	Flexor carpi ulnaris	Ulnar	Flexes and adducts hand
Middle	Flexor digitorum superficialis	Median	Flexes phalanges and hand
Deep	Flexor digitorum profundus	Median, ulnar	Flexes phalanges and hand
Posterior,Superficial	Extensor carpi radialis longus	Radial	Extends and abducts hand
	Extensor carpi radialis brevis	Radial	Extends hand
	Extensor digitorum	Radial	Extends little finger
	Extensor digiti minimi	Radial	Extends little finger
	Extensor carpi ulnaris	Radial	Extends and adducts hand
Deep	Abductor pollicis longus	Radial	Abducts thumb and hand
	Extensor pollicis brevis	Radial	Extends thumb
	Extensor pollicis longus	Radial	Extends thumb
	Extensor indicis	Radial	Extends index finger
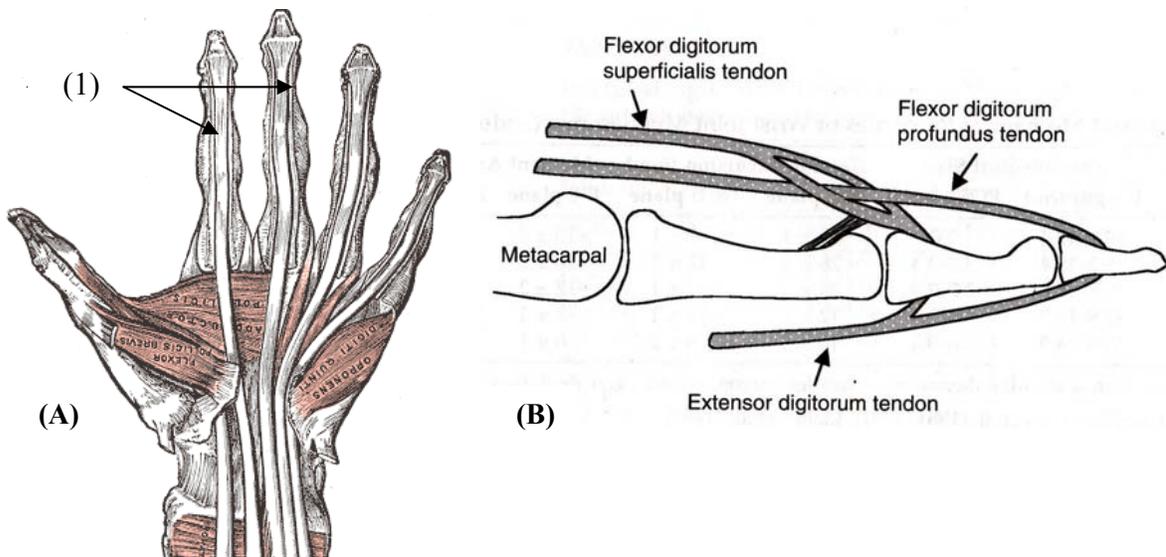
Figure 14: (A) The FDP flexor tendons in the palmar side of the hand attach to the distal phalanx (1) [109], and (B) the FDS flexor tendon splits at the PIP joint in the finger to allow the deeper FDP tendon through [106].

FDS Tendon   FDP Tendon
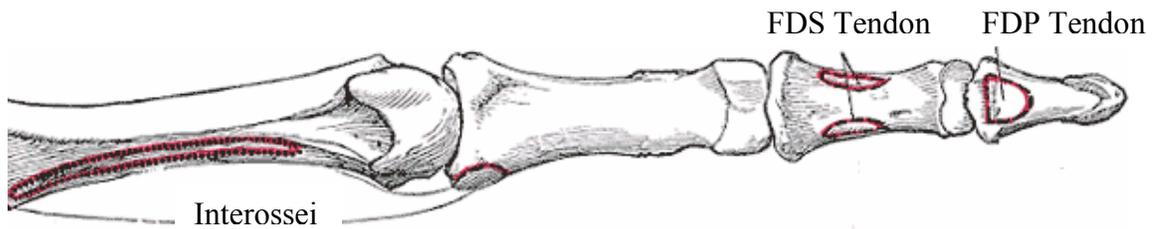
Interossei

Figure 15: The red outline on the palmar side of the finger indicates where the Interossei and the flexor tendons attach [109].
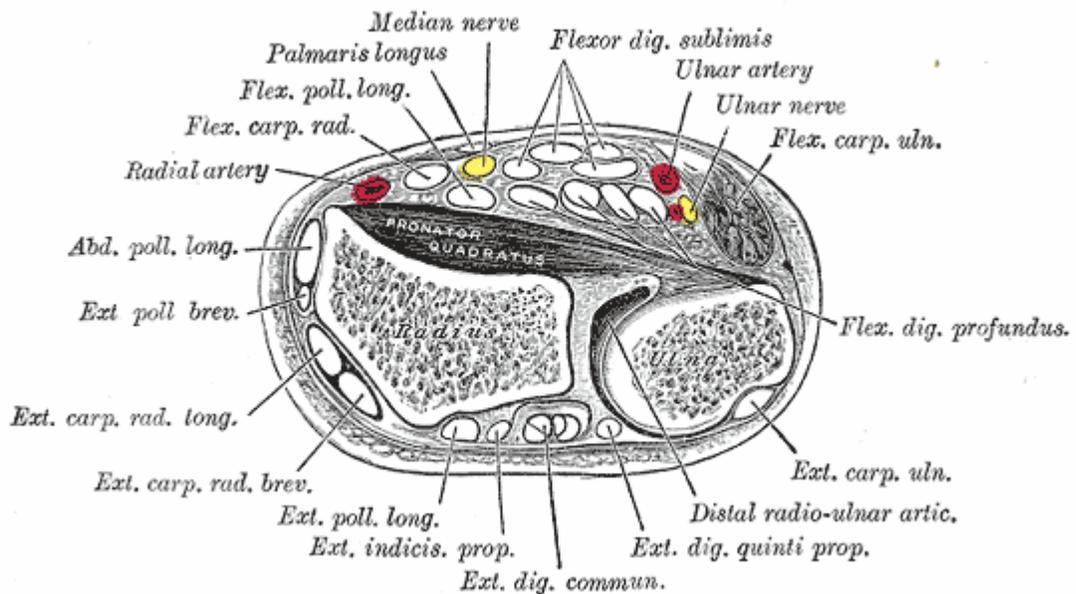
Figure 16: The cross section of the hand at the wrist level, with the palm side up. The FDS tendon is shown above the FDP tendon [109].

3.2   Functional Anatomy

3.2.1   Joint Articulations

Knowing the abilities and limitations of joints, muscles and tendons in a healthy hand is important to determine an optimal design to restore some of the motor abilities in disabled patients. In order to perform the grips and grasps of daily tasks, the hand joints must be able to have flexion/extension, abduction/adduction, circumduction and opposition depending on the motion involved.

Flexion is defined as the movement of a joint that results in a decrease of the angle between two bones at the joint, while extension refers to the increase of the angle at

the joint (Figure 17 A, C, E). Adduction is a movement of the joints which brings the fingers closer to the sagittal plane (midline of the arm and hand), and abduction is the opposite motion of moving away from the sagittal plane (Figure 17 B, D). Circumduction is defined as the movement pattern which moves the limb in a circular pattern using a combination of flexion/extension and abduction/adduction (Figure 17 G). Opposition motions refer to the combinations of flexion and abduction and axial rotation of the joints. One of the most remarkable motions of the human hand, opposition of the thumb sets humans apart from many animals by opposing (or turning back) against the other four fingers which allows for refined grip (Figure 17 F).

Referring to Figure 13, the MCP, PIP and DIP joint articulations form the basis for finger motion while the CMC, MCP and IP joints allow for motion of the thumb. Even though the CMC joints in the fingers are stabilized by the interosseous ligament to form a relatively immobile joint, its main function is to allow the hand to conform to objects being handled [106]. The CMC joint in the thumb however permits flexion/extension in the plane of the palm of the hand, abduction/adduction in a plane at right angles to the palm, circumduction, and opposition. The MCP joints in the fingers and thumb allows for flexion/extension, abduction/adduction (when not flexed) and circumduction motions. The interphalangeal joints only permit flexion and extension in the finger and thumb. The intrinsic muscles and tendons involved with flexion, extension, abduction, adduction of the fingers and thumb are summarized in Table 4 and shown in Figure 17 A-G.

Many researchers have categorized the hands functional position when manipulating objects. These classifications are not universally standardized, but convenient names are often adopted. The main grips and grasps are shown in Figure 17 H-K. One of the unique characteristics of human hands is their ability to conform around many different objects. Although several other variations of these grips exist, the index pinch, key grasp, hook and power grips may adequately describe hand prehension patterns. It is hard to quantify how often these configurations are used throughout the day, although some papers suggest various percentages for the average human [111]. Overall, disabled persons wish to restore quality to their lives by having the ability to feed, clean and dress themselves. All of these tasks can usually be completed by the

index pinch, key grasp, hook and power grips.

Table 4: The intrinsic muscles and tendons involved with flexion, extension, abduction, adduction of the fingers and thumb.

Motion	Phalanx	Joint	Muscle
flexion	all fingers	MCP	Lumbricals/Flexors
	"	"	dorsal interossei
	"	"	palmer interossei
	little finger	"	digiti minimi brevis
	thumb	"	flexor pollicis brevis
	all fingers	PIP	flexor digitorum superficialis
	all fingers	DIP	flexor digitorum profundus
	thumb	IP	flexor pollicis longus
extension	all fingers	all joints	extensor digitorum
	"	"	extensor carpi ulnaris
	index	"	extensor indicis
	little finger	"	extensor digiti minimi
	all fingers	DIP/PIP	lumbricals
	"	"	dorsal interossei
	"	"	palmer interossei
	thumb	MCP	extensor pollicis brevis
	"	IP	extensor pollicis longus
adduction	fingers	MCP	palmer interossei
	thumb	"	adductor pollicis
abduction	fingers	"	abductor digiti minimi
	"	"	dorsal interossei
	thumb	CMC/MCP	abductor pollicis longus
	"	CMC/MCP	abductor pollicis brevis
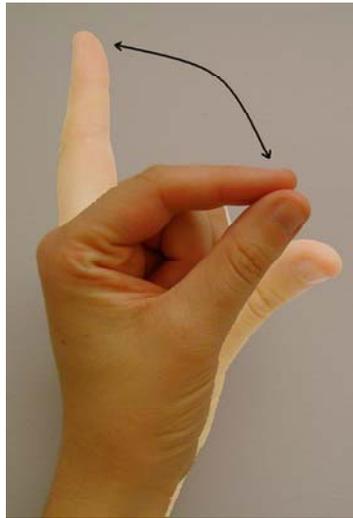
(A) Flexion (towards thumb) and extension (away from thumb) of the MCP, PIP and DIP joint of the index finger.
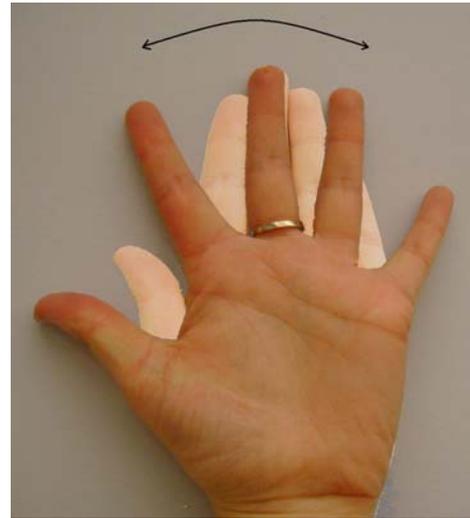
(B) MCP finger adduction (towards each other) and abduction (away from each other).
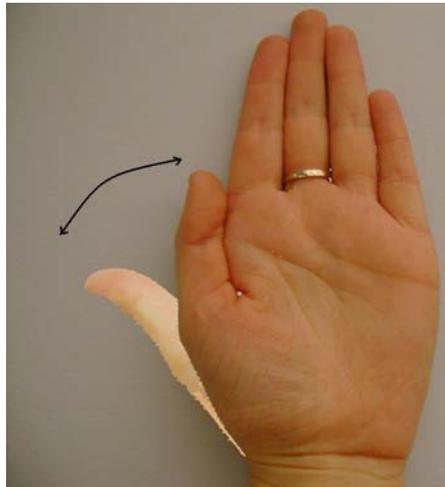
(C) Thumb CMC joint flexion (towards the index finger) and extension (away from the index finger).
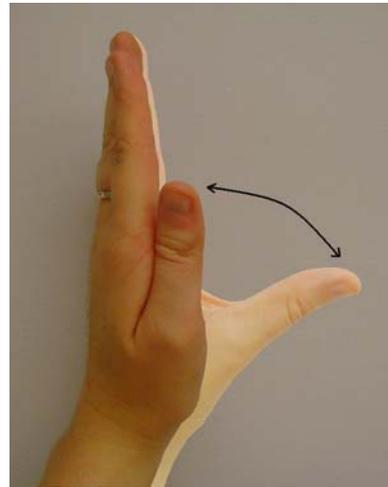
(D) Thumb CMC joint adduction (towards the index finger) and abduction (away from the index finger).

Figure 17 (A)-(K): Joint articulations and grip configurations of the hand.
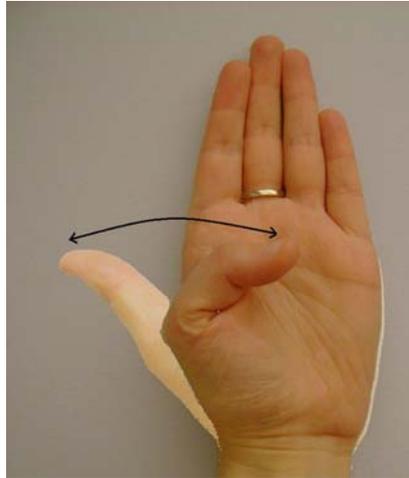
(E) Thumb MCP, PIP and DIP flexion (towards the palm) and extension (away from the palm).
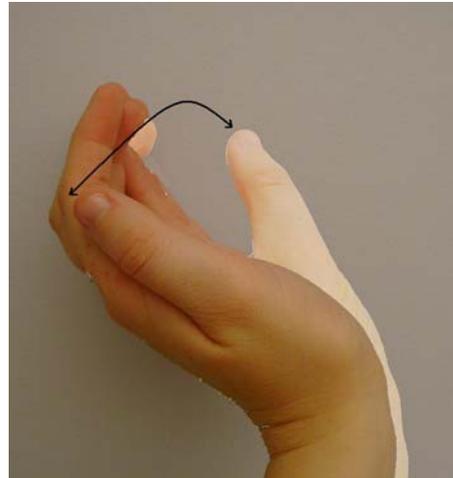
(F) Thumb opposition. The thumb is rotated towards the little finger.
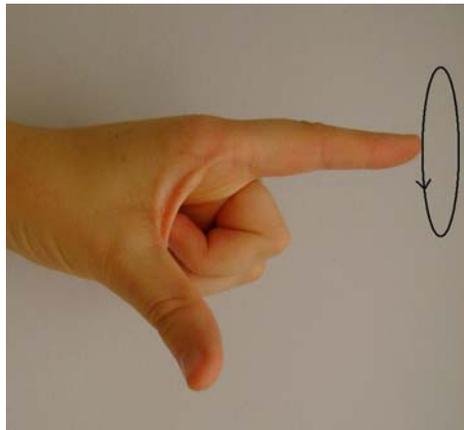
(G) Index finger MCP circumduction while keeping the PIP and DIP joint fixed.

(H) Hook Grip
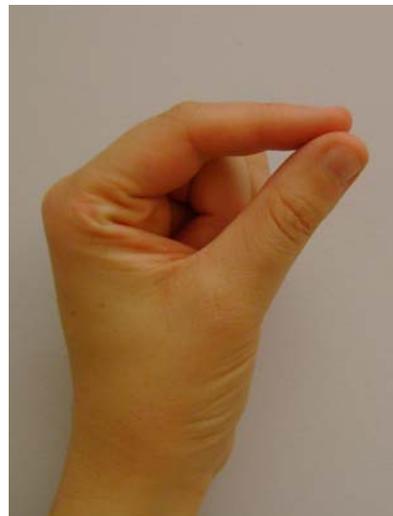
(I) Pinch Grip

Figure 17 continued.
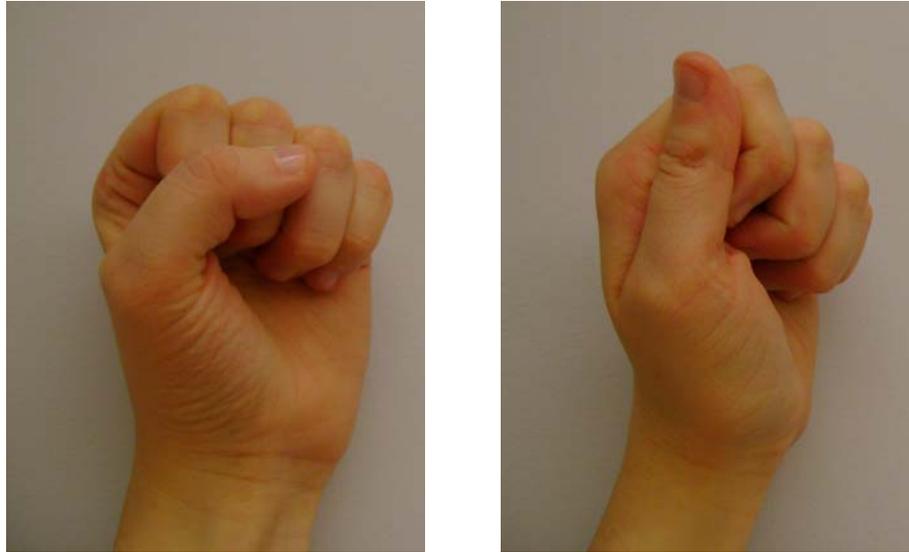
(J) Power Grip   (K) Key Grip

Figure 17 continued.

3.2.2   Tendon Excursion

When a person decides on a particular hand motion, brain signals are translated to the forearm muscles which in turn activate the tendons to articulate the hand joints in about 30-50 ms, depending on the motion. To accomplish a hand grasp, several muscles work together in order to perform the desired grip, mostly to optimize the body from becoming too fatigued. As previously mentioned, there are typically two sets of muscles around a joint: one set as an active primary mover, and the other set passively opposing. Therefore, the active muscle set is contracting and shortening, hence moving the tendon more than the passive muscle. This idea can be extended to quantify the differences in tendon excursion under passive and active motion. Many of the results in the literature require this knowledge for rehabilitative research, and one groups findings show the mean excursions of FDS and FDP tendons in cadavers were 1 mm on passive flexion, respectively, as compared to 14 mm and 10 mm on active flexion, respectively [112]. Although this study measured tendon excursion on cadavers, as well as during and after operative repair, other tendon displacement studies on healthy subjects showed the same pattern of passive motion having a lower measurement than passive, as expected.

Traditionally, tendon displacements (or excursions) are obtained by non-invasive estimations using joint rotation angles and moment arms of the fingers [90,107].

Generally, this technique has limitations because it assumes the tendon is without interconnections, free to move, and constant throughout the rotation of the finger [107]. In actuality, the tendons have interconnections which will alter the actual displacement of a tendon during rotation. Furthermore, the moment arm is not constant throughout full joint rotation [113]. Other invasive methods to determine tendon excursion have used X-ray images with surgically placed metal markers [114]. These experiments are mostly research-based and have limited clinical applications. Other studies have used cadaver hand specimens in order to estimate passive tendon excursions [95,100]. Since passive tendon excursion is smaller than active excursion, it is difficult to determine the actual excursion experienced during different grip configurations using this method [112].

Chapter 4

The Physics of Ultrasound

4.1   Ultrasound Propagation

Sound waves are a form of mechanical energy that propagate as a pressure wave through a solid, liquid or gas medium. They are usually called compressional or longitudinal waves, and are produced by a vibrating source. During vibration, the forward movement of the sound source causes a pressure rise in the adjacent medium. Likewise, as the source moves backwards, there is a pressure drop in the medium such that the molecules move apart [98]. This constant push-pull action of the sound source results in alternating molecular compression and rarefaction in the propagating medium (Figure 18).
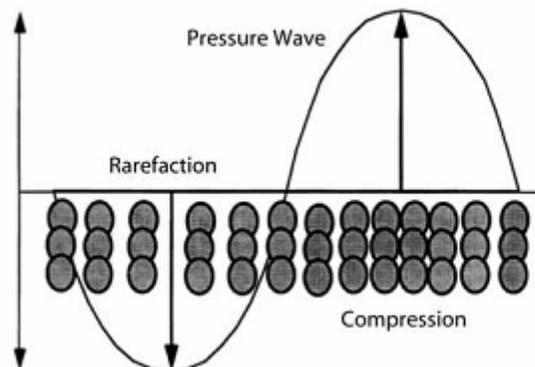
Figure 18: Propagation of sound [98].

The speed of ultrasound propagation c (m/s), in a medium such as soft tissue can be expressed as Equation (1) [115]:

$$c = \left(\frac{k}{\rho_o} \right)^{1/2} \tag{1}$$

Where:

k is the bulk modulus, measured in N/m^2, and is a measure of the stiffness (hardness) of a medium, or its resistance to compression.

ρ_o is the mass density, measured in (kg/m^3).

A propagating ultrasonic wave is subject to a progressive pressure amplitude and intensity decline. This is known as attenuation and is mainly caused by reflection, refraction, scattering, absorption and nonlinear propagation. Many of these factors are strongly frequency dependent, thus limiting the imaging depth with increasing frequency. The attenuation, a (dB), can be approximated by Equation (2) [115]:

$$a = 0.5fL \tag{2}$$

Where:

f is the transducer frequency, measured in MHz.

L is the imaging depth, measured in cm.

The attenuation coefficient, a_c (dB/cm) is approximated by Equation (3) [115]:

$$a_c = 0.5f \tag{3}$$

In soft tissues for example, there is approximately 0.5 dB of attenuation per cm for each MHz of frequency [115]. Other common attenuation coefficients, penetration and frequencies can be found in Table 5 for soft tissue and Table 6 for other media.

Table 5: Attenuation Coefficients and penetration depth for soft tissue [115].

Frequency (MHz)	Attenuation Coefficient (dB/cm)	Penetration (cm)
2.0	1.0	30
3.5	1.8	17
5.0	2.5	12
7.5	3.8	8
10.0	5.0	6
15.0	7.5	4

Table 6: Attenuation Coefficients for other media [116].

Tissue	Attenuation Coefficient (dB/cm)
Blood	0.200
Muscle	1.500
Liver	0.700
Brain (adult)	0.800
Brain (infant)	0.300
Bone	10.00
Fat	0.600
Water	0.002
Soft Tissue (average)	0.700
Castor Oil	1.000

Reflection is a type of attenuation which is quantified in terms of acoustic impedance differences at interfaces. The acoustic impedance of a medium, z (rayls), is a measure of the medium's resistance to sound transmission. Inhomogeneties of the medium's impedance form the basis of ultrasonic and Doppler imaging. This is because boundaries between adjacent media with different impedance values change the characteristics of sound transmission. As a result of these changes, sound waves undergo reflection and refraction at these differing interfaces.

Reflection is also a special case of scattering which occurs at flat and smooth boundaries (Figure 19 A). The amplitude of this reflection, a_r, is directly related to the magnitude of the differences in the acoustic impedances at the interface, and is given by Equation (4) [115]:

$$a_r = a_i \left(\frac{z_2 - z_1}{z_2 + z_1} \right) \tag{4}$$

Where:

a_i is the incident amplitude

$z1, z2$ are the impedances of media 1 and 2, respectively
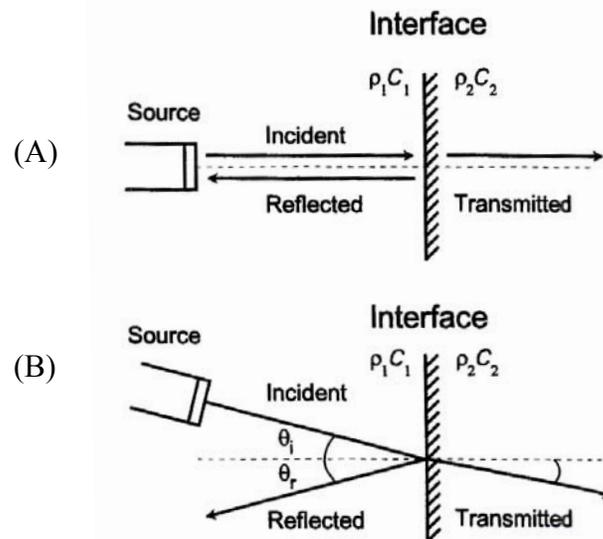
Figure 19: (A) Reflection of ultrasound at a plane boundary, and (B) reflection and refraction on a plane boundary (oblique angle) [116].

Table 7 demonstrates the ratio of reflected amplitude to the incident amplitude for various interfaces. It is useful to note that this is only an estimate because various errors exist in determining the speed of sound. Table 8 tabulates various media of interest in

medical ultrasonics along with their corresponding average speed c, and their acoustic

impedance z.

Table 7: Ratio of reflected amplitude to the incident amplitude for various interfaces [116].

Reflecting interface	Ratio of reflected to incident wave amplitude	Percentage energy reflected
Fat/Muscle	0.10	1.08
Fat/Kidney	0.08	0.64
Muscle/Blood	0.03	0.07
Bone/Fat	0.70	48.91
Bone/Muscle	0.64	41.23
Lens/Aqueous Humour	0.10	1.04
Soft Tissue/Water	0.05	0.230
Soft Tissue/Air	0.9995	99.90
Soft Tissue/ PZT Crystal	0.89	80
Soft Tissue/ Castor Oil	0.07	0.43

Table 8: Speed of sound and acoustic impedances of various media [116].

Material	Speed (m/s)	Acoustic Impedance (rayles) $*10^6$
Air	330	0.0004
Amniotic fluid	1510	-
Aqueous humour	1500	1.50
Blood	1570	1.61
Bone	3500	7.80
Brain	1540	1.58
Cartilage	1660	-
Castor Oil	1500	1.43
CSF	1510	-
Fat	1450	1.38
Kidney	1560	1.62
Lens of eye	1620	1.84
Liver	1550	1.65
Muscle	1580	1.70
Perspex	2680	3.20
Polythene	2000	1.84
Skin	1600	-
Soft tissue average	1540	1.63
Tendon	1750	-
Tooth	3600	-
Vitreous humour	1520	1.52
Water at 20°C	1480	1.48

If the wavefront strikes the media at an oblique angle, the beam also undergoes reflection and refraction (Figure 19 B). The angle of reflection is at an equal but opposite angle to the incident wave, with an amplitude given by Equation (5) [106]:

$$a_r = a_i \left(\frac{z_2 \cos\theta_i - z_1 \cos\theta_T}{z_2 \cos\theta_i + z_1 \cos\theta_T} \right) \tag{5}$$

Where:

a_r is the amplitude of the reflected wave

a_i is the amplitude of the incident wave

θ_i is the incident angle

θ_T is the transmitted angle

Refraction is the deviation of the wave as it crosses the boundary of differing media. The angle of propagation is given by Snell's Law in Equation (6) [116]:

$$\frac{\sin\theta_i}{\sin\theta_T} = \frac{c_1}{c_2} = \mu \tag{6}$$

Where:
c_1, c_2 are the speed of sound in media 1 and 2, respectively
μ is the index of refraction

If the boundary is not flat and smooth and the surface discontinuities are not smaller than a wavelength, some of the energy of the wave is scattered in many directions (Figure 20). These discontinuities may be changes in density or compressibility of the media. Scattering is a very important factor in ultrasound because it permits imaging of tissue boundaries not along the direction of the wave's propagation.
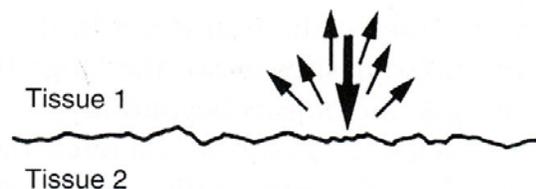
Figure 20: Scattering from a rough boundary [115].

Another process that contributes to the wave's attenuation is absorption. Absorption is the process in which sound is converted into heat. Absorption also increases rapidly with sound frequency propagating in the tissue and is responsible for thermal bio-effects.

Lastly, because the medium of interest is attenuating, nonlinear propagation also occurs. This is because the speed of sound is faster in higher pressure portions of the wave than the lower pressure portions. This affects the original smooth sinuosoid by changing its shape (Figure 21). This new nonsinusoid waveform propagates nonlinearly, and contains additional frequencies called harmonics which are even and odd multiples of the original frequency.
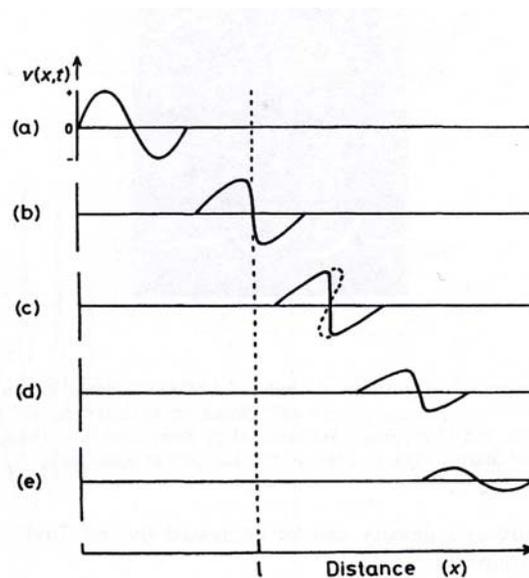
Figure 21: Non-linear propagation of a sinusoidal wave as it travels from (a) to (e) [116].

4.2   Doppler Physics

The Doppler Effect was first described by the Austrian physicist Christian Andreas Doppler (1803-1853) after a number of incorrect velocity measurements of moving stars [116]. Many industries today rely on the Doppler Effect for research. This includes the military, police, meteorologists, astronomers and medical professionals. Doppler ultrasound was first used in medicine in the late 1950's and has steadily become

an indispensable tool in several clinical applications. It is an especially important tool for non-invasive detection of many moving structures as well as determining velocities and displacements within the body.

The Doppler Effect is due to the change in the observed frequency of a wave due to motion of the source or receiver, away or towards each other. When the receiver moves towards the source, the observed frequency f_r increases and is given by Equation (7) [117]:

$$f_r = f_T \left(\frac{c+v}{c} \right) \tag{7}$$

Where:

f_T is the transmitted frequency

v is the receiver velocity

If the receiver moves at an angle θ, v is replaced by $v(\cos\theta)$ as in Equation (8):

$$f_r = f_T \left(\frac{c + v\cos\theta}{c} \right) \tag{8}$$

When the receiver is stationary and the source is moving with a velocity v, the observed frequency f_r is calculated by Equation 9:

$$f_r = f_T \left(\frac{c}{c-v} \right) \tag{9}$$

Or, if the source is moving at an angle θ, the observed frequency is given by Equation (10):

$$f_r = f_T \left(\frac{c}{c - v\cos\theta} \right) \tag{10}$$

In medical ultrasound, the ultrasonic beam is backscattered by moving tissue or blood. The source signal is Doppler shifted by the moving receiver (blood or tissue) (Figure 22 A). The blood or tissue now becomes the moving source as the wave is bounced back to the receiver (transducer) (Figure 22 B). The returning echo received at the transducer will thus use both Equation (8) and Equation (10) from above. The resulting observed frequency is given by Equation (11):

$$f_r = f_T \left(\frac{c}{c - v \cos \theta} \right) \left(\frac{c + v \cos \theta}{c} \right)$$

$$f_r = f_T \left(\frac{c + v \cos \theta}{c - v \cos \theta} \right) \tag{11}$$

Now, the Doppler frequency, f_D, is the received frequency subtracted from the transmitted frequency (f_r - f_T), and is given by Equation (12):

$$f_D = f_r - f_T = f_T \left(\frac{c}{c - v \cos \theta} \right) \left(\frac{c + v \cos \theta}{c} \right) - f_T$$

$$f_D = f_T \left(\frac{c + v \cos \theta - (c + v \cos \theta)}{c - v \cos \theta} \right)$$

$$f_D = \frac{f_T}{c} \left(\frac{2v \cos \theta}{1 - \frac{v}{c} \cos \theta} \right) \tag{12}$$

Because $v \ll c$, (or $v/c \ll 1$), Equation (12) can be approximated by:

$$f_D \cong \frac{f_T}{c} (2v \cos \theta) \tag{13}$$

Equation (13) is known as the Doppler Equation in medical ultrasound.
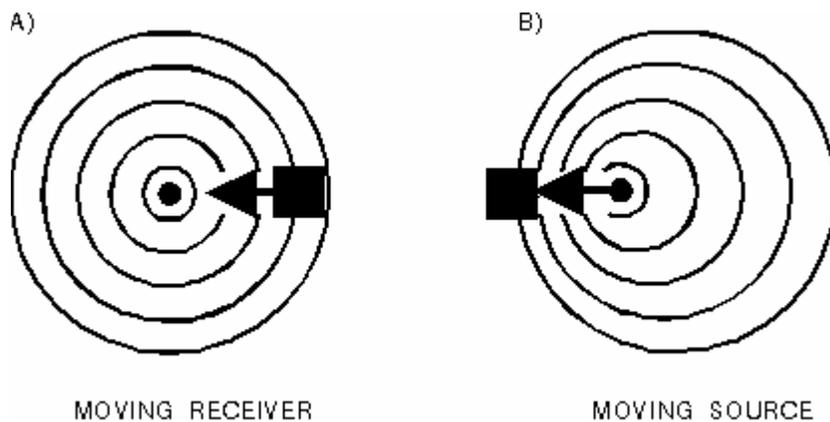
Figure 22: Doppler Effect with (A) the moving receiver and (B) the moving source [117].

Chapter 5

Device Components and Signal Processing for Duplex Imaging

5.1   Basic Ultrasonic Device Components for B-Scan Imaging

Sonographic instruments that are used in industrial and medical environments vary in design based on the required function. However, most ultrasonic machines share similar general components like a transducer, beamformer, signal processor, image processor and display (Figure 23).
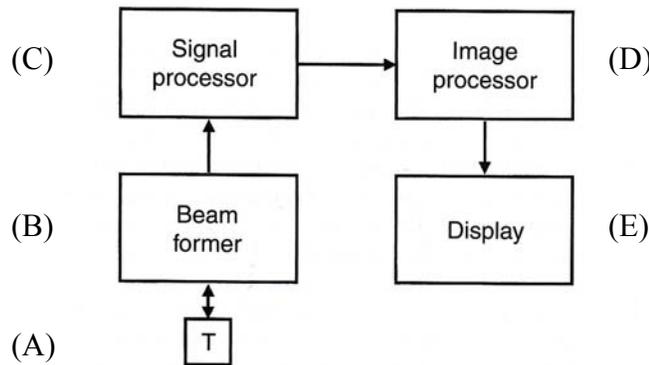
Figure 23: **A block diagram of a pulse echo imaging system with (A) the transducer, (B) the beamformer, (C) the signal processor, (D) the image processor and (E) the display [115].**

5.1.1   The Transducer

Ultrasonic transducers convert sound energy into electrical energy and vice versa. This is achieved by small piezoelectric elements within the transducer. Piezoelectric materials like quartz and some ceramics change shape by vibrating rapidly when an electric current is applied to them. These crystal vibrations in turn produce sound waves. Conversely, when incident sound waves are intercepted by the crystals, electric currents are produced. The most common piezoelectric material used in medical ultrasound is lead zirconate titanate (PZT). This is a ceramic which is manufactured to have piezoelectric properties by applying a strong electric field at high temperature [115]. PZT is sometime used with a polymer to create a composite material with improved acoustic

properties. The piezo element is backed with a damping material and matching layer to improve resolution (Figure 24). Resolution is also improved with beam focusing.
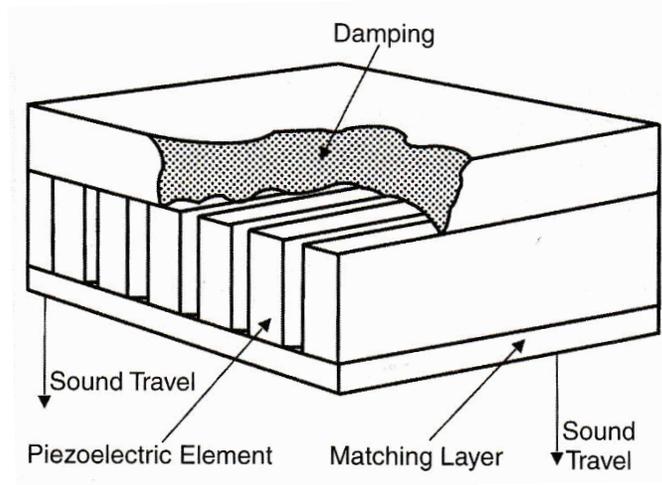
Figure 24: The internal parts to a transducer [115].

Transducers not only emit and receive echoes, but they have to send these waves through many paths in order to produce a cross-sectional image. This property is usually referred to as scanning, sweeping or steering the beam, and is performed by combining several piezoelectric elements on an array. These elements are rectangular (linear array) or curved (convex array) (Figure 25).
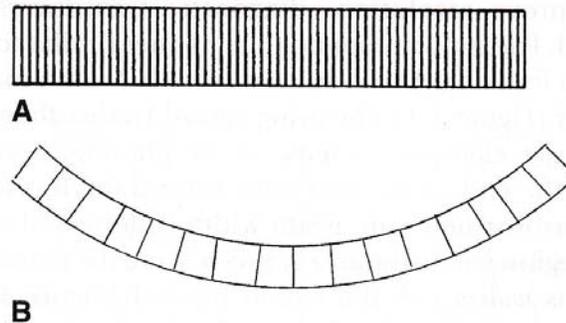
Figure 25: (A) Frontal view of a 64 element linear array and (B) side view of a 16 element convex array [115].

5.1.2   The Beamformer

The beamformer consists of a pulser, pulse delays, transmit/receive switch, amplifiers, analogue to digital converters, echo delays and a summer (Figure 26).
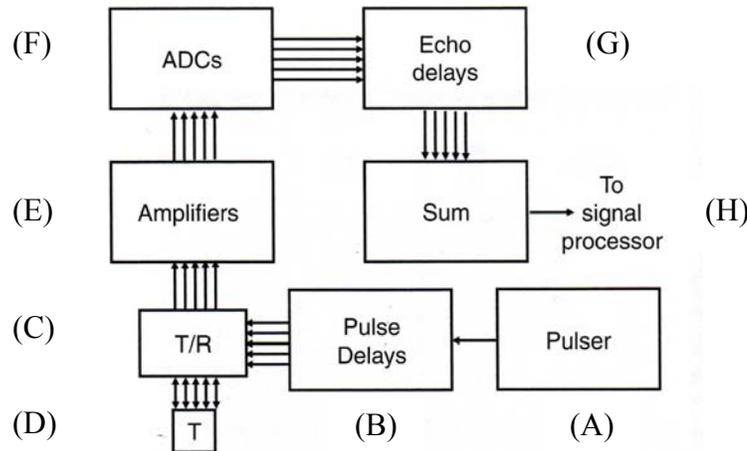
Figure 26: **Beamformer schematic with (A) the pulser, (B) pulse delays, (C) transmit and receive switch, (D) the transducer, (E) amplifiers, (F) analog-to-digital converter, (G) echo delays, and (H) the summer [115].**

- **Pulser and Pulse Delays**

The pulser produces the electrical voltages which forms the ultrasonic beam. The frequency of the voltage pulse determines the frequency of the resultant ultrasonic pulse that travels through the patient. This frequency ranges from 1-20 MHz and the pulse repetition frequency (PRF) ranges from 4 to 30 kHz for medical purposes.

Phase delays are necessary for the complicated sequencing and phasing operations which are involved to control beam steering, scanning and transmission focusing.

- **Transmit/Receive Switch (T/R Switch) and Amplifiers**

The T/R switch directs the pulser's voltage to the transducer during transmission. It also directs the returning voltage from the transducer to the amplifier during reception. The amplifiers then increase the small voltage amplitude received from the transducer.

- **ADC, Echo Delays and the Summer**

After amplification, the echo voltages pass through an analogue to digital converter (ADC). The resulting echoes from all signal channels are delayed to achieve proper focusing and steering. They are then added together in the summer to produce the final echo that is relayed to the signal processor.

5.1.3   Signal Processor

The signal processor receives the digital signals from the beamformer, and then processes them by filtering, demodulation and compression.

- **Filter**

A bandpass filter is often employed to reduce electronic noise. Other Harmonic filtering can improve resolution by using 2nd harmonics produced by nonlinear propagation.

- **Demodulation**

Because the echoes are difficult to use in this form for image processing, the signals are demodulated. Amplitude demodulation is illustrated in Figure 27. The signal is first rectified by inverting half of the waveform (Figure 27 a, b). It is then smoothed by passing it through a low pass filter (Figure 27 c). This removes the high frequency oscillations and retains the slowly varying envelope. This is a useful technique in ultrasound signal processing because only the amplitude of each echo is needed for the grayscale display.

(a)   (b)   (c)
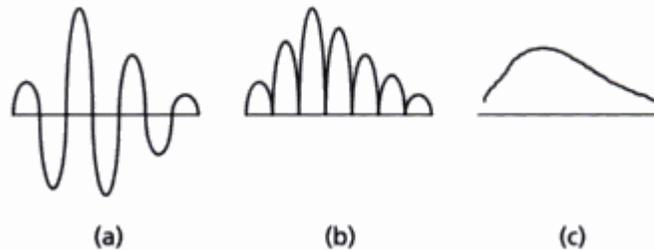
Figure 27 (a-c): Demodulation process [118].

- **Compression**

Compression is the final step in signal processing and reduces the differences between the minimum and maximum voltage amplitude. This transforms the echo data into a more usable range for display purposes.

- **Additional Processing**

Depending on the functions desired on the ultrasound machine, additional signal processing may occur. This includes spectral processing to determine the velocity components on the image.

5.1.4 Image Processor

The signal is now digitized, filtered, demodulated and compressed. The echo data needs to be further processed in order to be displayed on the screen. These processing steps include a scan converter, preprocessor, image memory, postprocessor and DAC (Figure 28).
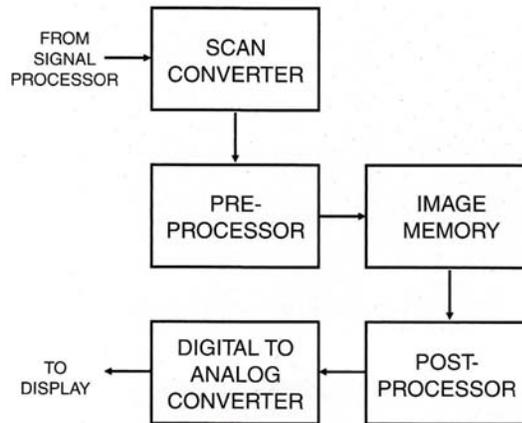
Figure 28: **Image Processor [115].**

The Scan Converter reformats the echo signal into an image form for further processing, storage and display. The image is preprocessed using edge enhancement, pixel interpolation and then stored in memory. Other post processing techniques determine how the echo data is displayed on screen. The data is then converted into a voltage using a digital to analogue converter (DAC), and is then relayed to a monitor where the echo brightness is displayed.

5.2   Pulsed Wave Doppler Signal Processing

There are several noted issues discussed in the literature about using A and B-Scan hybrid systems for prosthesis control. The discussed shortfall inspired the new approach of using PW Doppler to sense user intention for hand exoskeleton applications. The following discussions take a closer look at PW Doppler machines by describing the signal acquisition and processing steps, spectral analysis, errors and approximations. Using these processing techniques, a Matlab^{TM} script is presented in Chapter 6 to show

how the PW Doppler signal can be acquired from a moving tendon and used for

exoskeleton control.

5.2.1   PW Doppler Signal Acquisition & Pre-Processing

PW Doppler technology has been made available to clinicians since the late

1950's. Since this time, PW Doppler devices have become an indispensable tool in

research and medical diagnostics. This is mainly due to the advancement in signal

processing and computing power. This includes increased performance of higher

resolution and efficient systems that remain cost effective to its users.

PW ultrasound velocimetry involves detailed analysis of the shift frequencies that

constitute the Doppler signal. The acquisition & processing steps are outlined in Figure

29 and discussed below.
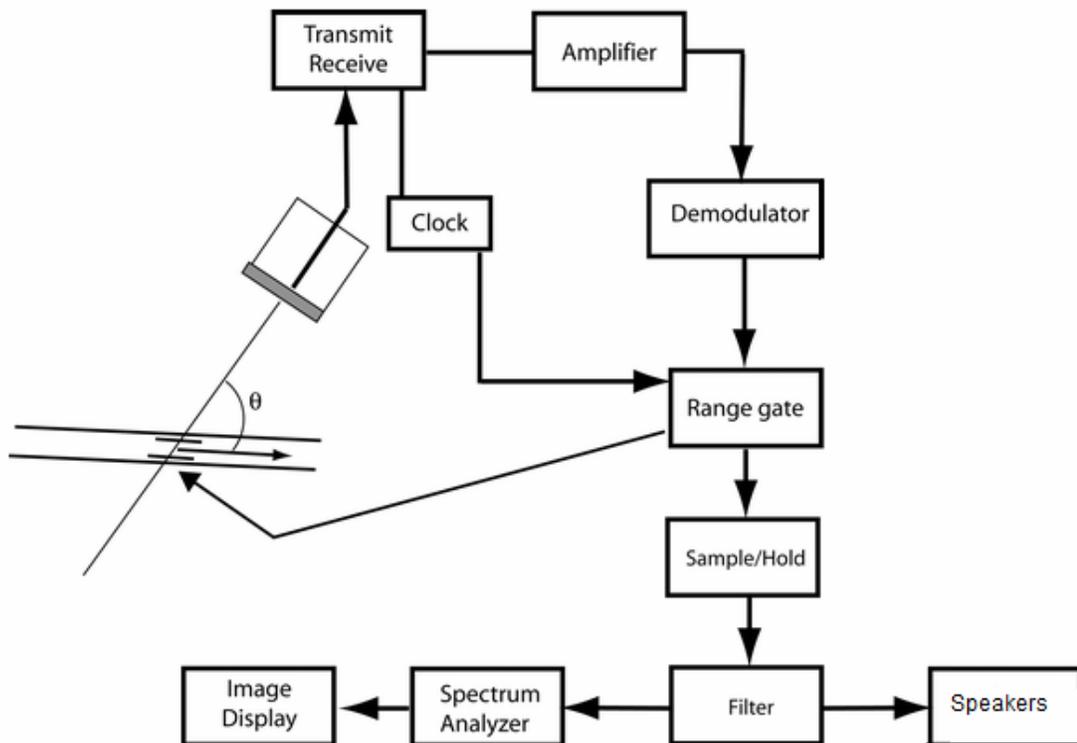
Figure 29: **PW Doppler Processing [119].**

- **Transmitter and Receiver**

The transducer transmits a train of sequential pulses to the desired sample volume in the body. The returning signals are received and then amplified since the returning echo voltages are generally weak.

- **Demodulation**

The total received signal contains the Doppler shifted frequencies and the carrier transmitted frequency. Demodulation refers to the extraction of the Doppler frequencies from the carrier frequency. Furthermore, flow direction away or towards the transducer must be distinguished. Both processes are accomplished by a phase quadrature procedure. This technique mixes incoming signals with the phase shifted signals from the transducer. These reference signals are assumed to be ¼ of a cycle out of phase (90º), hence the name "phase quadrature". This technique results in the generation of the incoming signal and quadrature output. This discriminates direction because when the flow is towards the transducer, the incoming signal lags the quadrature by 90 º. Similarly, flow away from the transducer results in the incoming signal leading the quadrature by 90 º. Thus direction discrimination can be determined by phase information.

- **Range Gate, Sample & Hold, and Filters**

Because only the echo data from the sample volume is desired, the returning signal is gated. This is accomplished by extracting only the received echoes that lie within a particular depth in the beam (or a particular range in time).

The sample and hold gathers all the phase shift and Doppler information from all the sets of pulses within the range gate. This step is necessary because there are many different phase shifts corresponding to the different structures in the range gate. Therefore, the signal is sampled and held until enough time has passed for all reflections within the gate to return. The resulting signal is then bandpass filtered to remove low or high frequency noise.

5.2.2   PW Doppler Spectral Analysis

The Doppler shift signal is now demodulated and filtered, and is represented by variations of amplitude over time (Figure 30).
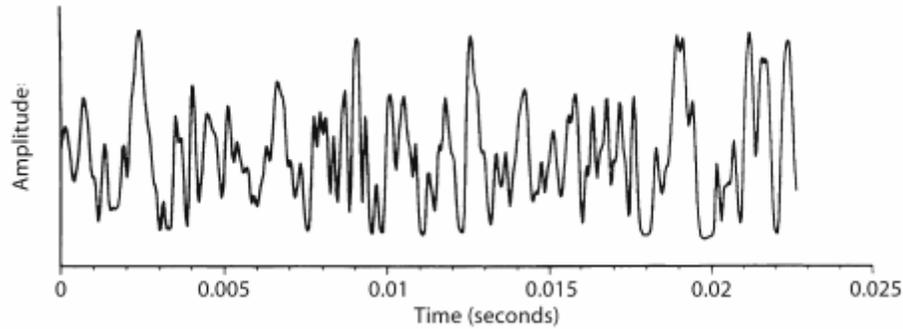
Figure 30: **Doppler signal after demodulation [98].**

This signal is also in an audible output form, and is sent to the speakers, as shown Figure 29. This audible stereo signal is a direct representation of the Doppler frequency shift and particle flow velocity.

At the same time as the audible output, spectral processing occurs in order to quantify the Doppler shift velocities and to display them on a screen in real time. Although various methods exist, Fourier-based analysis is by far the most powerful mathematical tool used in spectral processing. First described in early 1800's, this process breaks down a periodic waveform into its constituent frequencies with amplitude and phase information (Figure 31).
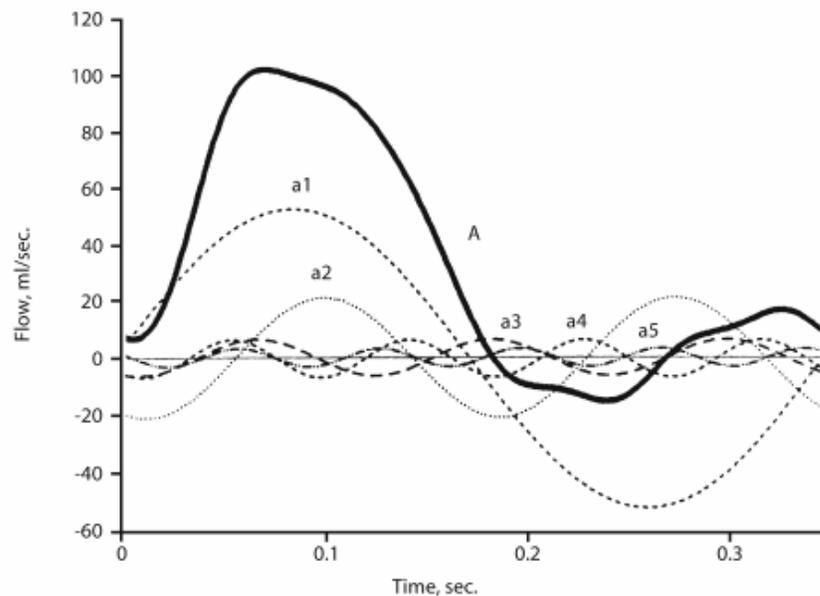
Figure 31: **Principle of Fourier Transform analysis [98].**

This is accomplished by Equation (14) [120]:

$$X(f) = \int_{-\infty}^{\infty} x(t)e^{-2j\pi ft}dt$$

$$x(t) = \int_{-\infty}^{\infty} X(f)e^{2j\pi ft}df$$

(14)

Where:

t is the time

$j = \sqrt{-1}$

f is the frequency

$x(t)$ is the continuous signal in the time domain

$X(f)$ is the continuous signal in the frequency domain.

For practical medical purposes, a sample of data is taken such that a discrete series of frequency points is used. The discrete Fourier Transform (DFT) is given by Equation (15):

$$X(\omega_n) = \sum_{n=0}^{N-1} x(t_n)e^{-jw_k t_n}$$

(15)

Where:

$k = 0, 1, 2, \ldots, N\text{-}1$

ω_k is the kth frequency sample

    For example, if a signal with frequency components 10, 25, 50 and 100 Hz is occurring at all times the signal will have a Fourier transform as illustrated in Figures 32 A and B. However, if these same frequencies exist at different times in the signal, the resulting DFT still shows the four frequency peaks as before (Figures 33 A, B). In this example however, the frequency peaks that are present in the signal do not occur at all times. This example demonstrates the difference between stationary and non-stationary signals. The DFT just shows which frequency components exist, but do not reveal at what times they exist. These non-stationary signals are better analyzed using the Short-Term Fourier Transform (STFT). This method separates the signal into small segments in time, where the signal can be considered stationary. This is known as windowing. The most often used windows are a Hamming window, Bartlett window or a rectangular window (Figures 34 and 35). The windows can also be overlapped to improve resolution.
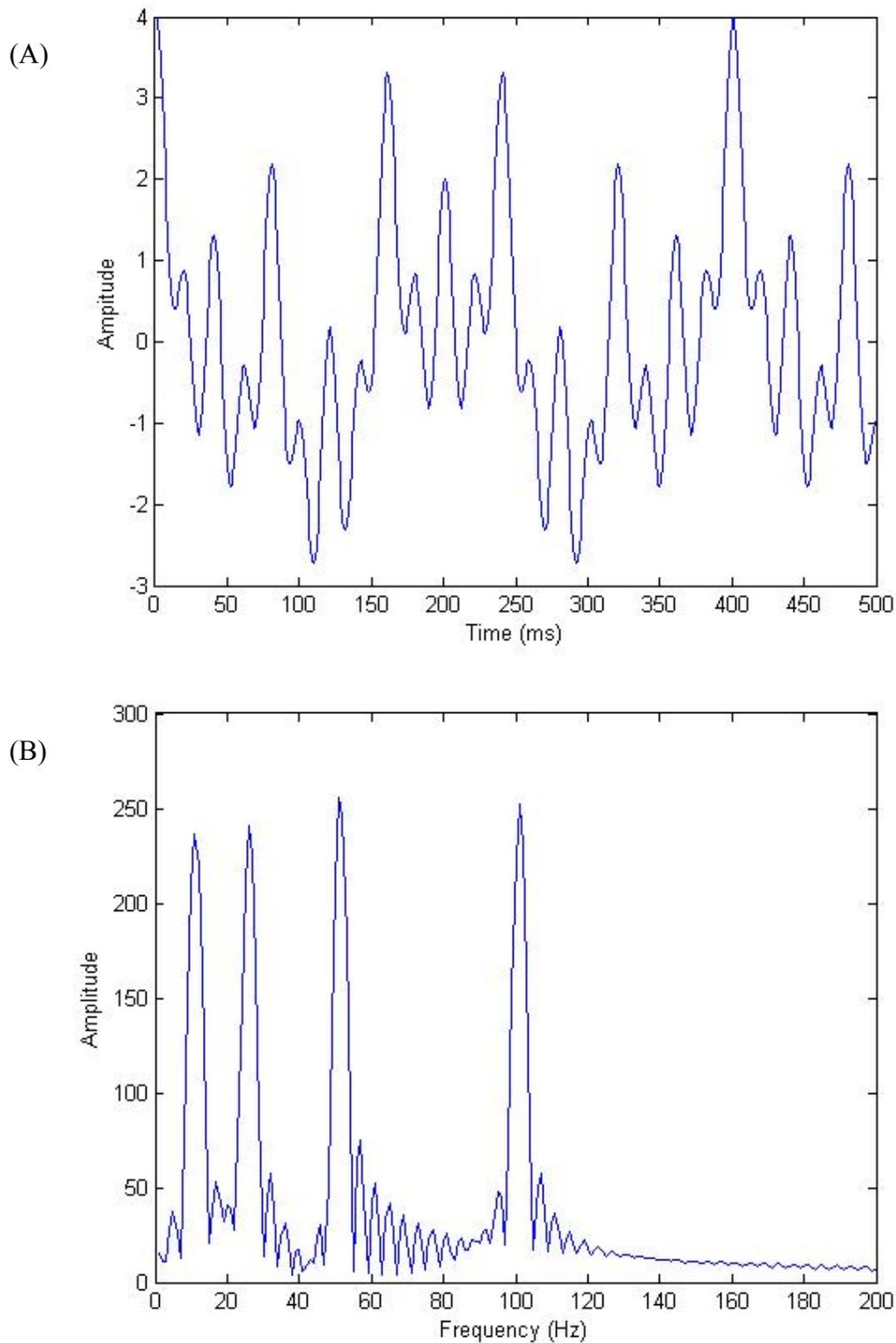
Figure 32: (A) 10, 25, 50 and 100 Hz occurring at all times, and (B) its corresponding Fourier Transform in Matlab[TM]. Note the four peaks in the above figure, which correspond to four different frequencies of 10, 25, 50 and 100 Hz exist at all times.
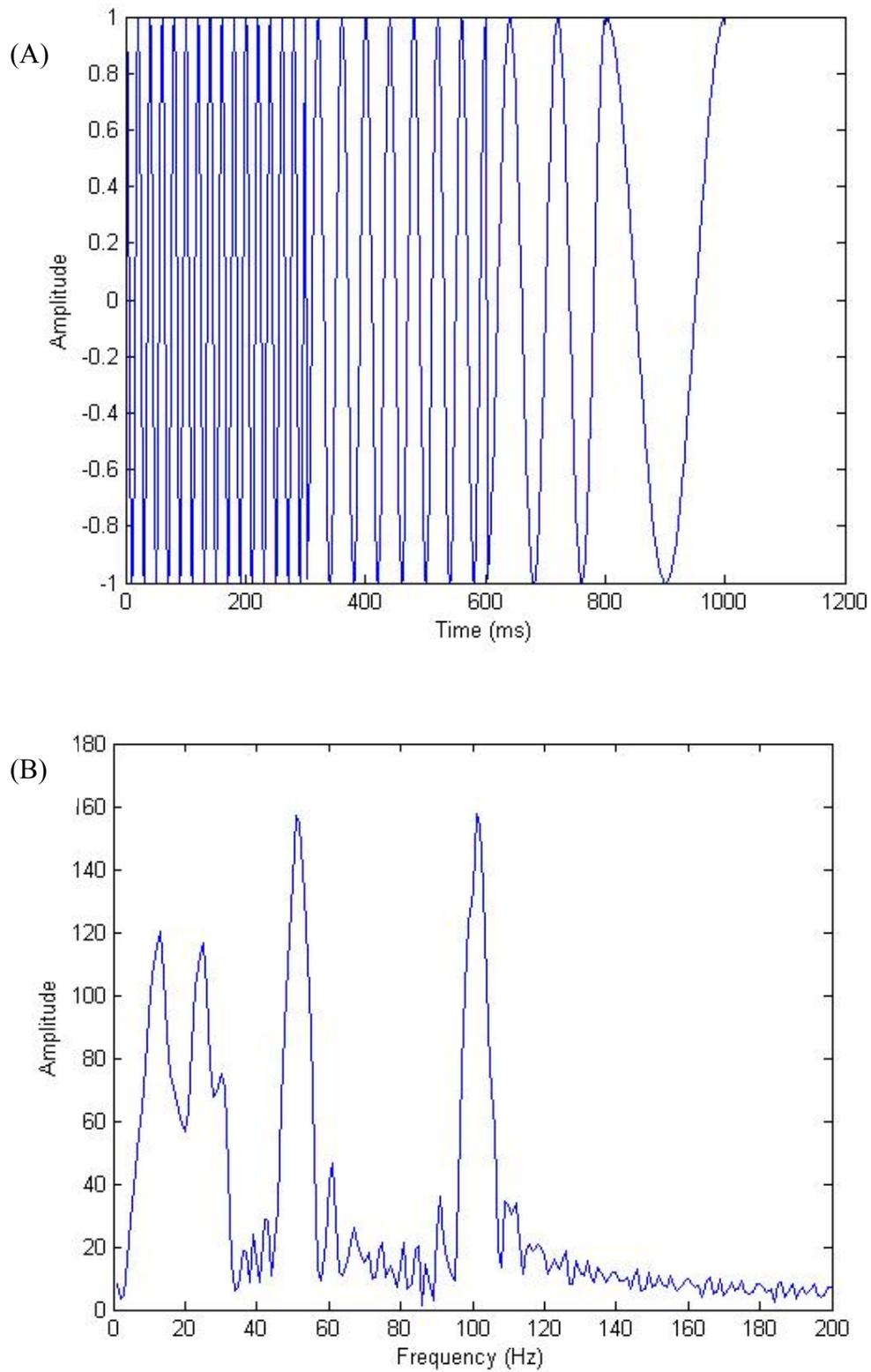
Figure 33: (A) 10, 25, 50 and 100 Hz signal in Matlab^{TM} occurring at different times, and (B) The signal in (A)'s corresponding Fourier Transform in Matlab^{TM}.
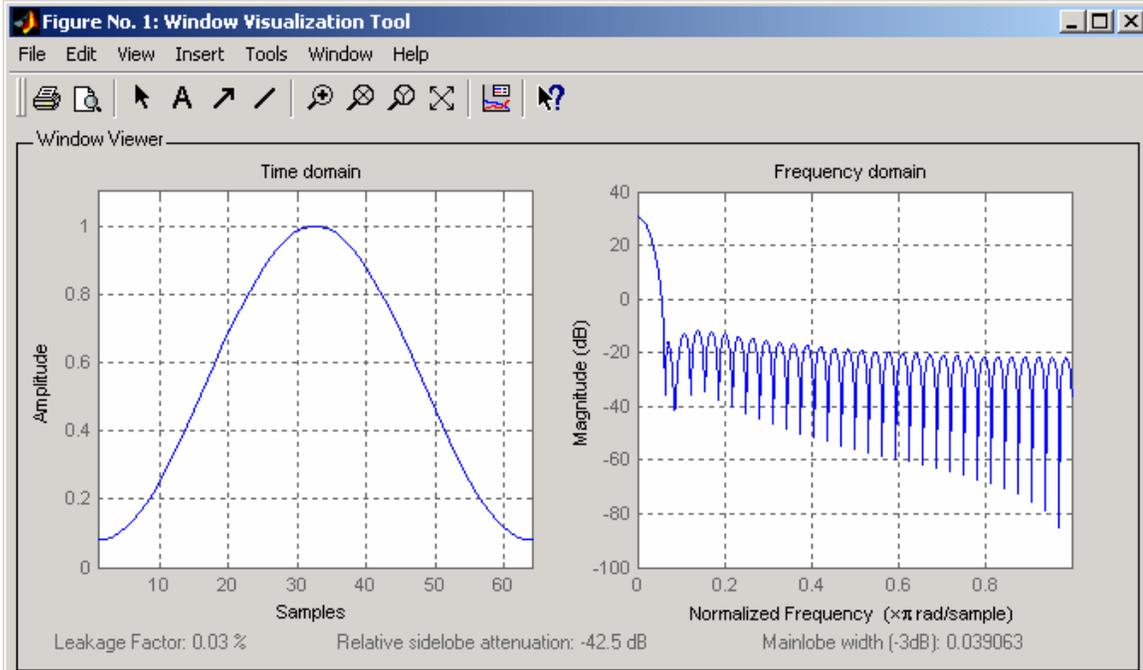
Figure 34: A 64 point Hamming Window from Matlab ™
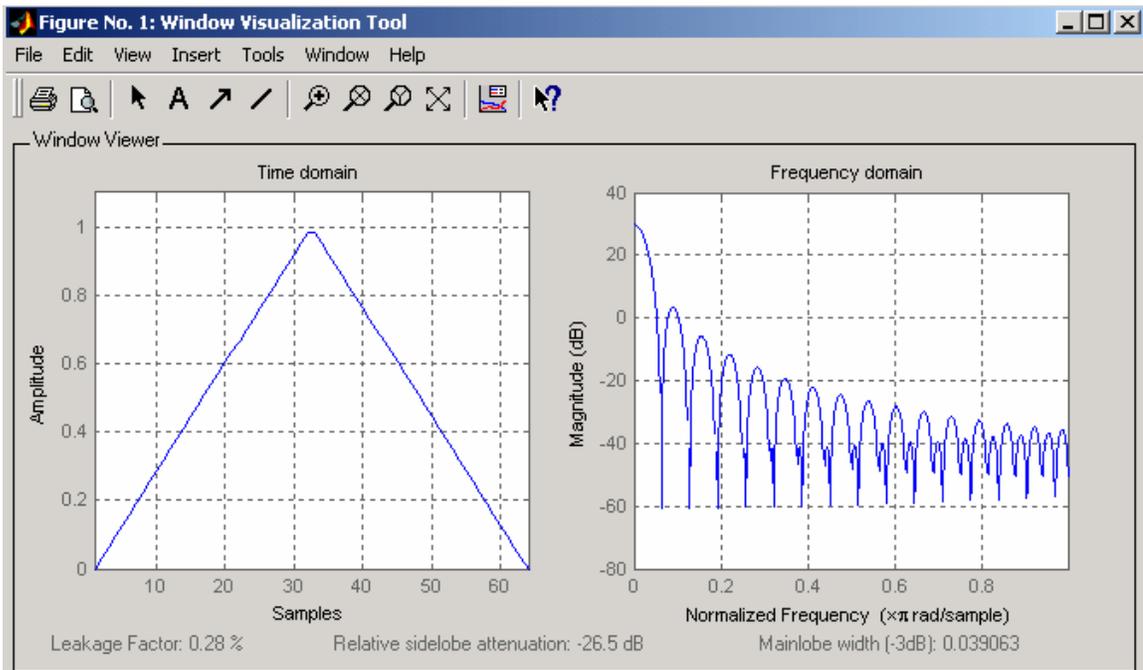
Figure 35: A 64 point Bartlett Window from Matlab ™

Ultrasound machines display the frequency space information in a spectrogram form. This is a 3-D plot representing frequency vs. time in 2-D, and power spectral density in the 3rd dimension. In the frequency vs. time 2-D plot, each "bin" on the plot represents the range of frequencies present during the small time interval (Figures 36 and 37). The length of the "bin" sides are determined by the number of Fourier Transforms, the window size and the window overlap used on each small time interval.
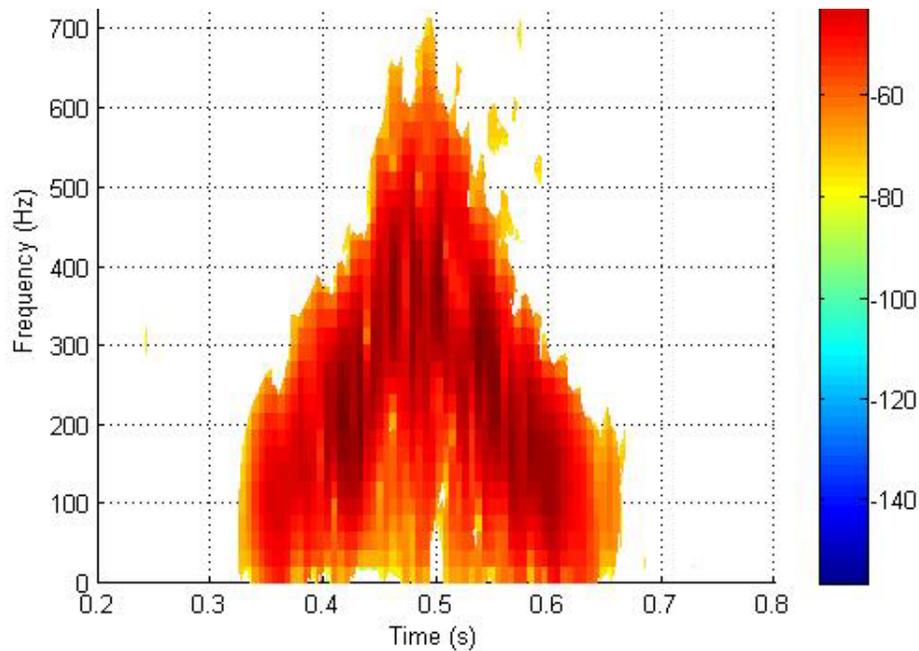
Figure 36: **A typical frequency spectrogram obtained in Matlab ^{TM}. The Doppler frequencies are measured in Hz, and are displayed on the y-axis. The small time intervals are measured in seconds. The power spectral density is measured in dB, and is displayed on the z-axis as a colour-scale.**
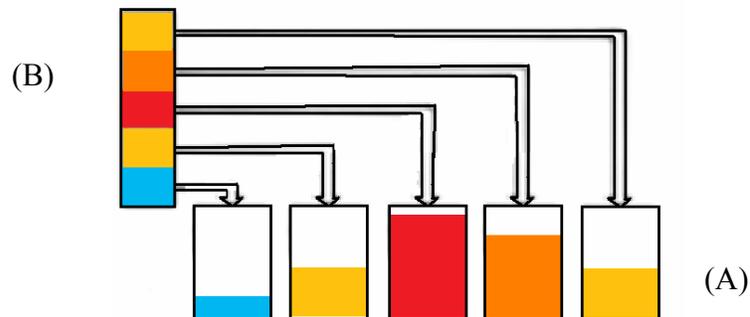
Figure 37: **(A) Demonstrating the frequency bins for the corresponding power spectral density on a frequency (or velocity) spectrogram (B).**

Also, using the Doppler formula in Equation (13), the velocity can be estimated and plotted in place of the frequency. Thus the ultrasound display usually shows a greyscale (or colour-scale) map of the velocity of the sample volume as a function of time. Once the velocity spectrogram is determined, it is important to estimate the displacements of the moving structure. This is accomplished by calculating the mean velocity curve and performing the velocity-time-integral (VTI). Referring to Figure 36, there are several frequencies (or velocities) present at each moment in time, corresponding to the sample volume size of the moving object. In order to find the mean velocity curve, the mean velocity at each small time interval is calculated. This is achieved by calculating an intensity-weighted mean velocity (IWMV), i.e.:

$$ IWMV = \frac{\sum\limits_{i} V_i p_i}{\sum\limits_{i} p_i} \tag{16} $$

Where:

V_i is the estimated velocity of the ith data point, with a power spectral density of p_i at the time t.

Once the IWMV is calculated for each time interval, a mean velocity curve can be fit to these points. Once the curve is fit, it is integrated to estimate the displacement of the moving structure.

5.2.3   Errors and Approximations:

It is important to summarize all of the problems, approximations and errors involved in obtaining and processing the Doppler shifted signal. Firstly, the transmitted signal suffers from many forms of attenuation. This limits the practical imaging depth. Also, when the signal is received, other errors incur because of circuitry noise and analogue to digital conversions.

When it comes to PW Doppler errors, perhaps the most prominent problem is the uncertainty involved with estimating the sample volume's flow velocity. There are two major causes of this error. Primarily, there are resolution issues with the STFT. This stems from the type of window chosen, the length of this window, the number of window

overlaps, and the number of Fourier transforms performed. This determines the "bin" length and width (or the resolution) of each small frequency and time interval on the spectrogram. Secondly, when these frequencies are used to determine the velocities with the Doppler formula, the Doppler angle must be determined. Referring to the Doppler formula (Equation (13)), the greatest frequency shift occurs when the transmitted wave is parallel to the flow axis. If the ultrasonic wave intersects a sample at an angle, only the component of the flow velocity vector that is along the wave path contributes to the Doppler Effect. Therefore as the angle increases, the frequency shift decreases. When the angle reaches 90 °, the Doppler shift is virtually non-existent. This is demonstrated by substituting *cos(90 °)* into Equation (13).

Most importantly, the Doppler angle presents a significant error if incorrectly determined. If the operator introduces an error ε into the cosine term, the measured velocity V_m is shown in Equation (17) [121]:

$$V_m = \frac{f_d c}{2 f_t \cos(\theta + \varepsilon)} \tag{17}$$

The error in the measured velocity can be expressed in terms of a ratio between V_m and the actual velocity V, and is shown in Equation (18):

$$\frac{2 f_t V_m \cos(\theta + \varepsilon)}{c} = \frac{2 f_t V \cos(\theta)}{c} \tag{18}$$

Rearranging the ratio,

$$\frac{V_m}{V} = \frac{\cos(\theta)}{\cos(\theta + \varepsilon)} \tag{19}$$

For example, if the actual flow was at $\theta = 50$ ° and the operator introduced a 3 ° error, a 6% velocity error is introduced. Similarly, if an error of 5 ° was introduced to the actual angle of 80 °, a 99.2% velocity error occurs (Table 9). It is therefore recommended to keep the Doppler angle between 30 ° and 60 ° to minimize the error [115].

Table 9: The cosine and speed errors when determining the Doppler angle [115].

True Angle (degrees)	Cosine Error (%)		Speed Error (%)	
	+2 degrees	+5 degrees	+2 degrees	+5 degrees
0	-0.1	-0.4	0.1	0.4
10	-0.7	-1.9	0.7	3.0
20	-1.3	-3.6	1.4	3.7
30	-2.1	-5.4	2.1	5.7
40	-3.0	-7.7	3.1	8.3
50	-4.2	-10.8	4.4	12.1
60	-6.1	-15.5	6.5	18.3
70	-0.6	-24.3	10.7	32.1
80	-19.9	-49.8	24.8	99.2

Other problems that exist with PW Doppler systems include aliasing and spectral broadening. When aliasing occurs, there is a misrepresentation of the frequency shift, magnitude and direction. This phenomenon is mainly encountered with high velocity flow and is described by the Nyquist limit and the Theorem on Sampling. These state that for unambiguous results, the maximum frequency must not exceed half of the sampling rate (or pulse repetition frequency) [115]. Other phenomena such as spectral broadening describe the thickening of the frequency peak on the frequency plot (Figure 38). This can be due from disturbed or turbulent flow and can possibly be indicative of a pathologic condition. Spectral broadening can also occur artificially by excessive Doppler gain, beam spreading and wide aperture arrays.
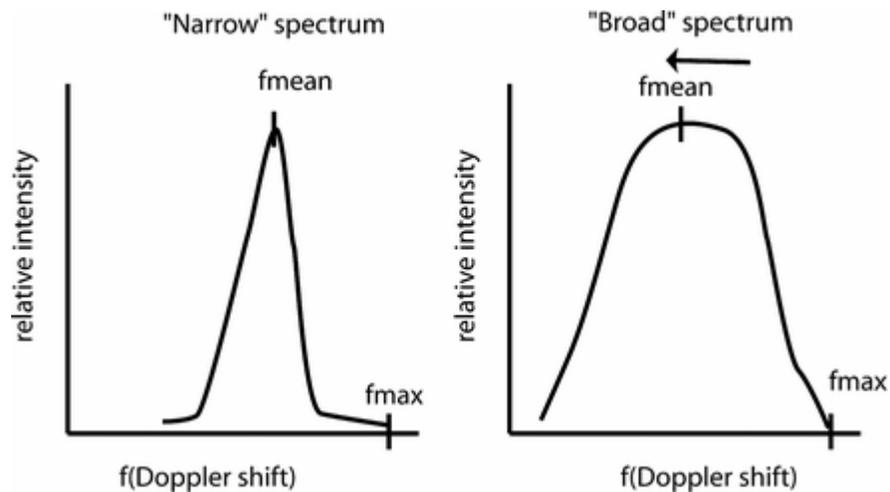
Figure 38: **Spectral broadening [119].**

Error also incurs when determining the mean velocity values for displacement estimation. Usually, a PW Doppler spectral processor employs a lower cut-off velocity (or frequency) filter to remove unwanted low frequency noise or slow moving objects. This filter is referred to as a Wall filter and is usually used to remove the signal from the slow moving heart wall in order to determine the blood displacement. It is important to select appropriate threshold values for this filter. An incorrect threshold value would ultimately affect the outcome of the displacement estimation because there would be excessive weighting to the higher amplitude frequencies (or velocities). This is because the mean frequency (or velocity) at a given time is calculated using Equation (16). This equation weights the velocities according to the amplitude of their power spectral density. Using an inappropriate frequency (or velocity) cut-off would result in an inaccurate mean velocity curve, velocity-time integral and thus, displacement.

Chapter 6

Proposed Techniques and Methodology

6.1   Introduction

As an alternative to other non-invasive methods, ultrasound scanners have shown remarkable accuracy when assessing tendon damage as well as tendon excursion [89-97]. Commercially available ultrasound scanners have many built-in imaging and Doppler functions which can reveal information about tissues, organs and flow estimations. In order to determine tendon excursion from ultrasonic grayscale images, tracking algorithms have been previously implemented [92]. These methods use block matching or cross-correlation techniques to scan each image in a cine-loop in order to detect and track the moving tendon. These processes usually require a lengthy offline analysis with a lower success rate due to resolution and computational issues. However, Pulsed-Wave or Color Doppler functions have shown improved accuracy in determining tendon excursions. These built-in functions of a typical off-the-shelf ultrasound scanner display real-time velocity spectrograms of the moving tendon and can allow for offline velocity-time-integration (VTI) to estimate the total excursion. Furthermore, because the tendon's frequency-shifted Doppler signals returning to the scanner are in the audible range, most ultrasound machines allow for real-time audible output of the signal to the on-board speakers. This audible output occurs at approximately the same time as the displayed velocity spectrograms.

One of the most desirable functions on ultrasound machines for research purposes is a completely open-architecture system for easy data access. This means that the signal can be obtained at any point in the system's processing phases so that the researchers can experiment with their own processing methods. These machines are quite remarkable, but very expensive. Some of the more affordable machines allow for a software development kit (SDK) that will allow for some data access. The off-the-shelf Doppler ultrasound scanner used in this thesis has the SDK capability, but it is non-trivial for usage by non-

Software Engineers. Also, this machine will only allow for raw data access before any system processing has taken place (demodulation, filtering, etc).

Unfortunately, most commercial Doppler ultrasound scanners do not allow for any raw data access in order to capture this audible signal in real-time. To address this issue, one research group has created acquisition software that uses an A/D converter to transfer the signal from the ultrasound machine to a PC for analysis [90]. However, their reliability study may be plagued with resolution issues from using a lower frequency transducer with the ultrasonic scanner. Other resolution issues in their study may be due to noise from the A/D converter as well as error accumulations from their choice of processing using zero-crossings. Although cost-effective, zero-crossing detectors have significant limitations when dealing with low velocities or a small sample size [116]. Both of these events occur when dealing with real-time tendon data acquisition and processing. Furthermore, the calculated tendon displacement cannot be reliably compared to the actual tendon displacement. This is because the actual tendon displacement is estimated using unreliable methods such as joint rotation angles and moment arms of the finger for non-invasive measurements [90].

Perhaps an easier method exists to acquire real-time echo data from an ultrasound machine that does not have data access capabilities. Referring to Figure 29, before the demodulated and filtered echo data is sent for spectral processing, it is relayed to the speakers. This audible signal is a direct representation of the Doppler shift frequencies (and flow velocities) and is displayed as an amplitude as a function of time (Figure 30). The signal can be acquired in real time by a soundcard (or other recording software), and then processed to find the spectral waveform. This is an efficient and inexpensive way to obtain the demodulated and filtered Doppler data from an ultrasound machine in real-time. Alternatively, one can use an expensive open-architecture ultrasound system to obtain the Doppler shift data at any processing step. This ensures that the ultrasound machine's software doesn't over-filter the data. However, for the purposes of the research presented in this thesis, the real-time Doppler signal output from an off-the-shelf ultrasound machine is obtained from the soundcard and processed using the Matlab^{TM} script presented in Section 6.4.

6.2   Experimental Objectives

The aim of this thesis is to address the need for an improved method to detect user intention for the ultimate purpose of hand exoskeleton control. The following experiments realize this objective by:

- Testing the accuracy of the original sensing strategy using PW Doppler and B-Scan ultrasound to detect the velocity and displacement of a moving "tendon-like" string and a beef flexor tendon. This novel sensing strategy obtains the Doppler shift signals from the moving object in real-time using the audible data from the soundcard. This signal is then processed using the tailor-made Matlab^{TM} script described in Section 6.4

- Demonstrating how the PW Doppler signal taken from a flexor tendon in a human index finger can control a robotic finger test-bed to mimic its motion. The tendon's Doppler shifted signal is obtained from the soundcard and processed by the tailor-made Matlab^{TM} script described in Section 6.4

6.3   Experimental Overview

6.3.1   Displacement Measurement Accuracy Test

In order to realize the above objectives outlined in Section 6.2, these first experiments initially address the need for an improved method to access and process Doppler-shift data from ultrasound scanners. In these first experiments, the displacement measurement accuracy of the proposed audio-based Fourier analysis technique which is described in Section 6.4 is compared against that of onboard software of a commercial PC-based ultrasound scanner. This is a feasibility study to show the accurate and real-time displacement estimation capability of the proposed processing technique. In order to achieve this objective, this experiment is separated into the following two parts:

1)   To first test the displacement accuracy of a moving "tendon-like" string by comparing the proposed processing technique against the commercial ultrasound machine, and

2)   To repeat this experiment with replacing the moving string with a biological flexor tendon from a cow.

6.3.2   Robotic Finger Demonstration Using the Proposed Processing Technique

In order to conclusively determine if the proposed processing technique can interpret user intention for robotic control, the following experiment is devised. Referring to Chapter 3, each FDS tendon attaches to the individual PIP joints in each of the fingers. The FDS tendon is responsible for PIP joint rotation towards the palm of the hand. An example of this type of joint rotation is the hook grip in Figure 17 H. For this experiment, the PIP joint in the index finger is allowed to rotate through a pre-determined set of joint rotation angles. The commercial ultrasound scanner will detect the FDS tendon's velocity and the proposed processing technique will estimate the tendon's displacement. As before, the tendon displacements calculated from the ultrasound scanner will be compared against the displacements calculated by the proposed processing technique and accepted models. The tendon displacements calculated by the proposed processing technique will then be translated into joint rotation angles because the robot finger's software requires the input to be in this form. These rotation angles will then be transferred offline (for simplicity sake) to the robotic finger in order for the robot to mimic the index finger's joint rotation. This study is a demonstration of the capabilities of the new processing technique to detect user intended finger motion and then to control a robotic device.

6.4   The Proposed Processing Technique Using Matlab^{TM}

The feasibility experiments in this thesis require an inexpensive method to acquire the real-time displacements vs. time data of a moving object. This Doppler shifted data is obtained from an off-the-shelf ultrasound machine and the soundcard. As in Figure 29, this Doppler-shifted signal is sent to the speakers and the ultrasound machine's spectral processor in real-time. The proposed Matlab^{TM} script uses the inexpensive approach by obtaining the signal from the soundcard because raw data access is not possible with the ultrasound machine chosen for these experiments.

The proposed spectral processing algorithm using Matlab^{TM} is based on the general Pulsed-Wave (PW) Doppler signal processing guidelines described in Section 5.2. For all experiments, the demodulated and filtered signal from the soundcard is first

filtered with an n-point moving average filter to remove some of the noise, where n-samples is chosen to optimize the data in each experiment. In order to determine the displacements of the moving object as a function of time, the Matlab^{TM} script then performs Fourier spectral analysis to first determine the Doppler shift frequencies in each small time interval. This is accomplished by first separating the signal into 512 samples (0.0116 seconds) and applying the Hamming window. The number of Fourier transforms performed on each window directly affects the resulting frequency and time resolution. Referring to Figure 36, the frequency resolution is the height of the "bin" sides on the frequency spectrogram. Using a variation of the Fourier transform from Section 5.2 (Equation (15)), the built-in Fourier transform function in Matlab^{TM} performs 2048 transforms per window using Equation (20):

$$X(k) = \sum_{j=1}^{N} x(j) \ e^{-\frac{2\pi i}{N}(j-1)(k-1)} \qquad (20)$$

Where:
   $X(k)$ is the signal in the frequency domain
   $x(j)$ is the signal in the time domain
   N is the number of Fourier transforms
   $i = \sqrt{-1}$
   $j = 1, 2, 3, \ldots, N$
   $k = 1, 2, 3, \ldots, N$

Because there are only 512 samples per window, the signal is zero-padded. This means that the 513th to the 2048th data points are zeros added to the end of the sampled signal in the window. Using this technique, the frequency resolution is calculated as 21.5 Hz by using Equation (21). Hence the "bin" height is 21.5 Hz (Figure 39).

$$\text{Frequency Resolution} = \frac{\text{Sampling rate from the soundcard (samples/second)}}{\text{Number of Fourier transforms/window (samples)}} \qquad (21)$$
$$= \frac{44100 \text{ samples/s}}{2048 \text{ samples}}$$
$$= 21.5 \text{ Hz}$$

To improve the time resolution, each window is overlapped by 50%. Therefore, instead of the time resolution being 0.0116 seconds, the resolution becomes 0.0058 seconds. This means that the "bin" lengths are 0.0058 seconds (Figure 39).

The Fourier transforms determined by Equation (20) are used to determine the power spectral density (PSD) of each "bin". The PSD is determined by applying Equation (22)

to each $X(k)$ determined by Equation (20) in each window and converting to the decibel scale (Figure 39). PSD and frequency threshold filters are also employed to remove unwanted amplitude and frequency noise.

$$PSD = |X(k)|^2 \quad \text{and} \quad PSD\ db = 10\ \log_{10} |X(k)|^2 \qquad (22)$$
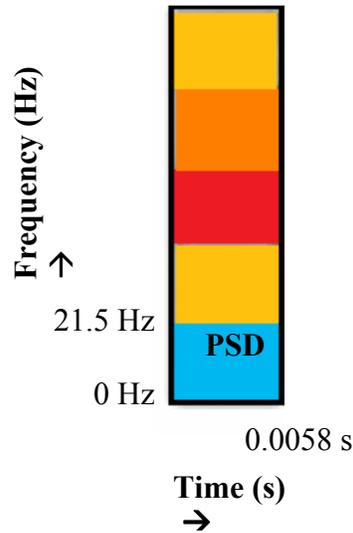
Figure 39: Demonstrating the frequency and time resolution on the spectrogram. Here, the time resolution is 0.0058 seconds, and the frequency resolution is 21.5 Hz, representing the "bin" length and height, respectively.

The resulting frequency spectrogram reveals the Doppler frequencies present at each time interval with a given PSD amplitude. These frequencies are converted to velocities using the Doppler Equation in Section 4.2 (Equation (13)), with the following parameters:

$f_T = 12$ MHz
$\theta =$ determined manually on the B-Scan image before the experiment starts
$c = 1540$ m/s

Because there are several velocities present at each small time interval (corresponding to the different moving areas of the sample region), Equation (16) from Section 5.2 is employed in order to determine the intensity-weighted-mean-velocity (IWMV) in each time interval. A cubic spline curve is then fit to the mean-velocity points using a built in function and toolbox in Matlab^{TM}. A cubic spline is a type of interpolation that uses piecewise polynomials on small chosen time intervals. This curve is then integrated in order to reveal the displacement vs. time of the moving object.

Chapter 7

Displacement Measurement Accuracy Test

7.1 String Displacement Measurement Accuracy Test

7.1.1   Experiment Set-Up

As shown in Figure 40 and Figure 41, the experimental setup consists of a moving string and pulley system that mimics biological tendon motion by allowing the string to slide by a known displacement under an off-the-shelf Doppler ultrasound scanner (LogicScan 128^{TM} by Telemed). The LogicScan^{TM} scanner collects the shift frequencies from the moving string with a 12 MHz transducer, which relays the signal to the portable scanner that is connected to a PC (Figure 42). The transducer is set on top of two ultrasound gel pads with a cut-out standoff wedge (Aquaflex^{TM} by Cone Instruments). The proper positioning of the transducer is first obtained by moving the string under the LogicScan's Color-Doppler Mode, which highlights the moving areas onscreen. Once the proper position is obtained, the scanner then amplifies, demodulates and digitizes the echo signal. This is done so that the signal can travel to a PC via USB for further onboard processing and displaying purposes. Simultaneously, the scanner's software on the PC will output an audible shift-signal to the PC's soundcard and will display the velocity spectrogram. The soundcard is an integrated SigmaTel^{TM} card with a sampling frequency of 44.1 kHz. The audible signal is obtained in real-time, processed and analyzed by the Matlab™ script described in Section 6.4. This signal represents the spectrum of velocities that are contained in the selected sample volume positioned on top of the string. For the purpose of determining the accuracy of estimating the string displacement, the scanner's onboard processing and the proposed audio-based processing techniques are tested using 20 experimental trials. For each trial, the string and stopper is manually pulled by 9.1 cm ± 0.1 cm to get into a starting position, and is then allowed to move under gravity with the mass and pulley system (Figure 40).
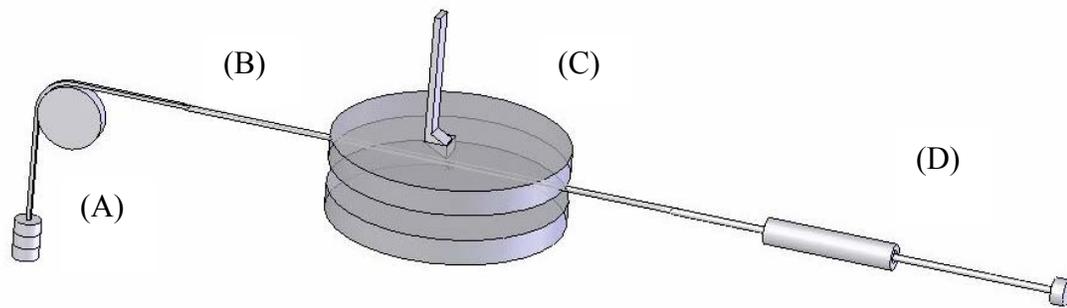
Figure 40: **Schematic diagram of the experimental setup with (A) the 100 g mass, pulley and string, (B) the string, (C) 2 Aquaflex gel pads with cut-out wedge and transducer, and (D) string guide and stopper.**
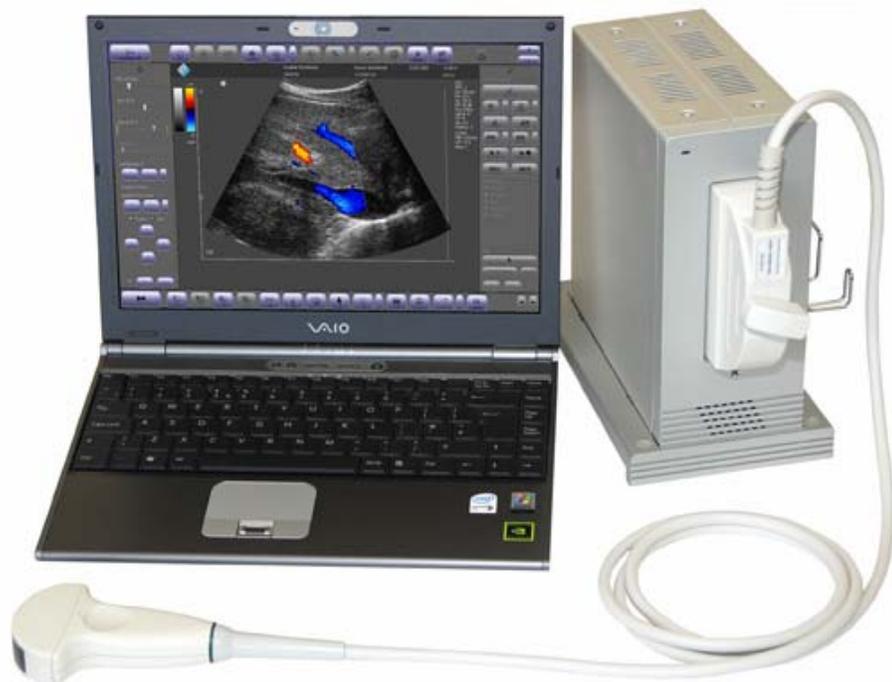
Figure 41: **The LogicScan 128^{TM} scanner and transducer by Telemed connected to a PC [86].**
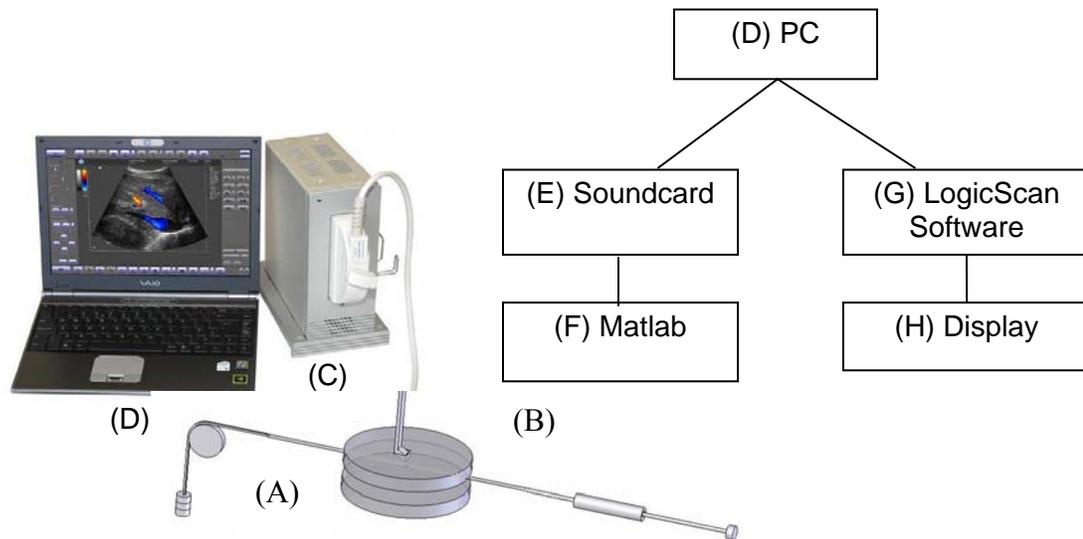
Figure 42: **Schematic of the ultrasound scanner's Doppler signal processing technique: (A) Doppler shifted signal from the moving tendon, (B) 12 MHz transducer, (C) LogicScan^{TM} scanner which is connected by a USB cable to the PC in (D), (E) the unprocessed Doppler shifted signal is sent to the soundcard where it is collected by Matlab™ in (F), and, simultaneously, the unprocessed Doppler shifted signal is sent to the scanner's software in (G) for spectral processing and (H) display.**

7.1.2 LogicScan^{TM} Scanner's Onboard Software

The string is first located with LogicScan's transducer and several modes are tested in order to determine optimal settings. The final ultrasound settings of LogicScan^{TM} are shown in Table 10. During the 20 trials, the string is displaced by 9.1 cm ± 0.1 cm. Figure 43 shows the resulting velocity spectrogram of the string displayed by LogicScan™ scanner's onboard software for Trial 1. The onboard software then performs the velocity-time-integral (VTI) to obtain the estimated displacements. The estimated displacements for the 20 trials are shown in Table 11. The mean estimated displacement for these trials is 8.59 cm with a standard deviation of 0.50 cm, in the case of using LogicScan's onboard software.

Table 10: Selected settings on LogicScan™ ultrasound scanner.

Pulse Frequency = 2 kHz	Correction Angle = 59º
Gain = 33%	Sample Size = 1 mm
Power Level = 28%	Wall Filter = 7%
Steering Angle = -10º	Dynamic Range = 30dB
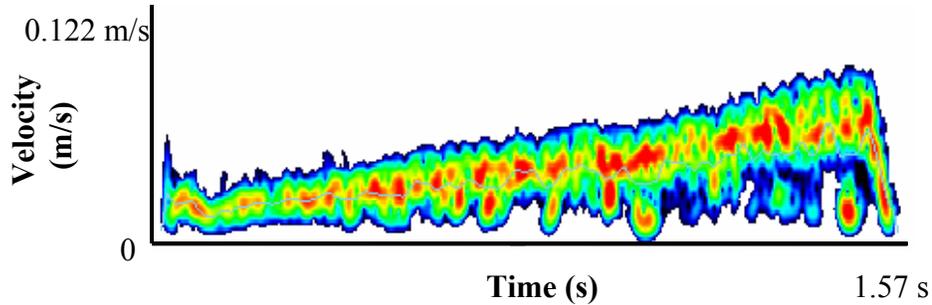
Figure 43: LogicScan™ scanner's velocity spectrogram for Trial 1's string velocity vs. time.

Table 11: String displacement estimation using LogicScan's onboard software.

Trial No.	Displacement (cm)	Trial No.	Displacement (cm)
1	8.76	11	8.65
2	7.47	12	8.58
3	7.13	13	8.80
4	8.25	14	8.80
5	8.50	15	8.69
6	8.53	16	9.13
7	8.67	17	8.72
8	8.73	18	8.78
9	8.72	19	9.13
10	8.68	20	9.17

7.1.3 Audio-based Doppler Signal Acquisition and Processing

For the previous 20 trials, the Doppler-shifted signal is obtained in real-time from the PC soundcard with a written script in Matlab™ which was described in Section 6.4. The signal (shown in Figure 44) is then processed offline (only for the sake of simplicity) in order to determine the feasibility of the proposed techniques. Note that this signal

contains noise from previous digitization step in the LogicScan^{TM} scanner as well as from the soundcard. The noise is reduced by a factor of 10 using a 100-point moving average filter. Since a moving average filter ultimately alters the characteristics of the signal, discretion is used in choosing a suitable sample size of the filter.

In order to determine the frequency content of the signal during small time intervals, a Short-Term Fourier Transform (STFT) is performed using 2048 transforms per window, 512 sample window size, and a 256 sample window overlap. The STFT script populates a frequency matrix for each time interval, with a given power level.

In order to determine if the audible data set is a feasible approach to real-time data acquisition and displacement measurement, the mean velocity curve and displacements need to be estimated. In order to determine the mean velocity curve, the Doppler equation (Equation (13)) is used, which transforms the shift frequencies into flow velocities. There are several frequencies (or velocities) present at each moment in time, corresponding to the sample volume size of the moving object. In order to find the mean velocity curve, the mean velocity at each small time interval is calculated. This is achieved by calculating an intensity-weighted mean velocity (IWMV) using Equation (16) for each moment in time. The power spectral density filter is set to be greater than 70 dB to neglect low amplitude noise.

The resulting data set contains the mean velocity of the moving string as a function of time. A cubic spline curve is first fit to this data, and then integrated so that the string displacement can be estimated. Matlab^{TM} has many built-in functions to perform the STFT, fitting a cubic spline and performing the velocity-time integral. Using this custom Matlab™ script, the mean velocity points, fitted mean velocity curve and displacements (via integration) are estimated, as shown in Figures 45 and 46 for Trial 1. Using the proposed technique, the mean displacement is 9.14 cm with a standard deviation of 0.28 cm. The estimated displacements for all 20 trials are shown in Table 12.
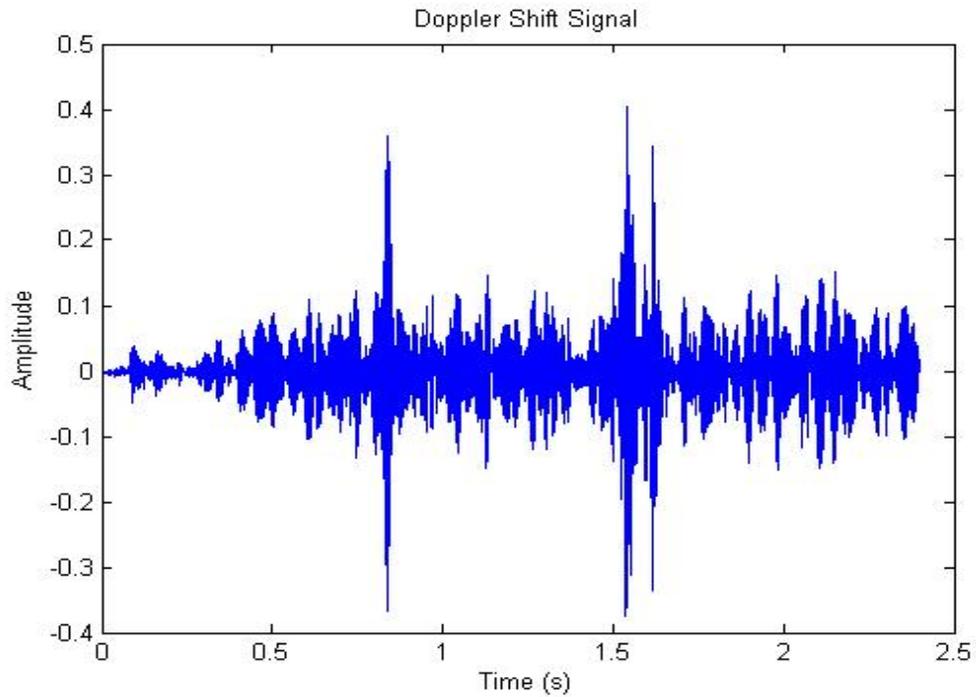
Figure 44: Demodulated Doppler shifted audio signal.
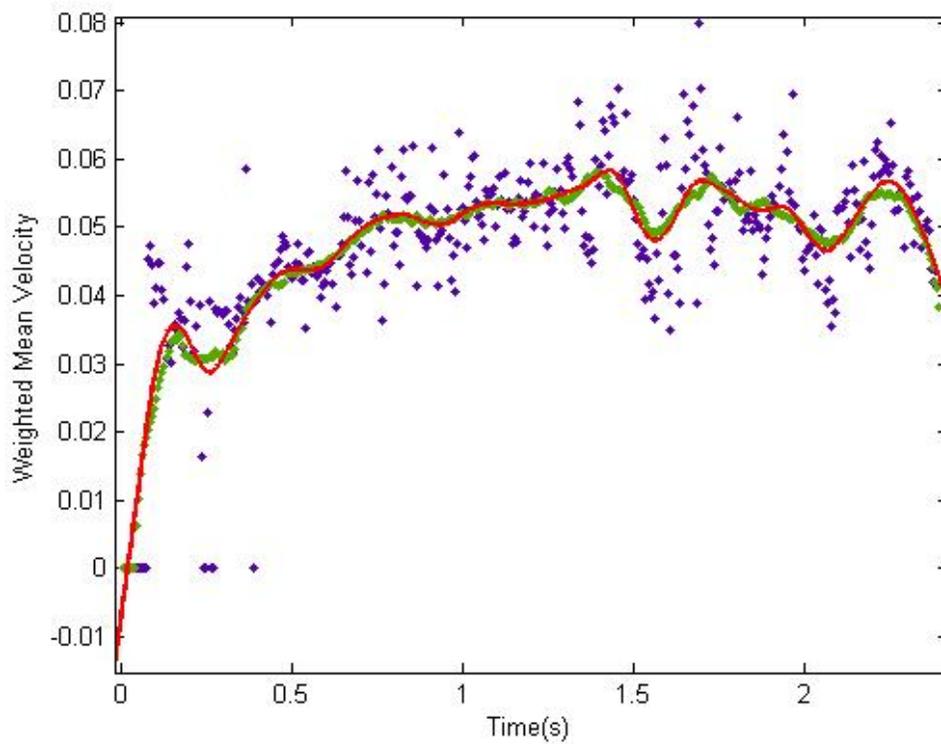
Figure 45: Mean velocity data points (in m/s) and fitted curve for Trial 1.
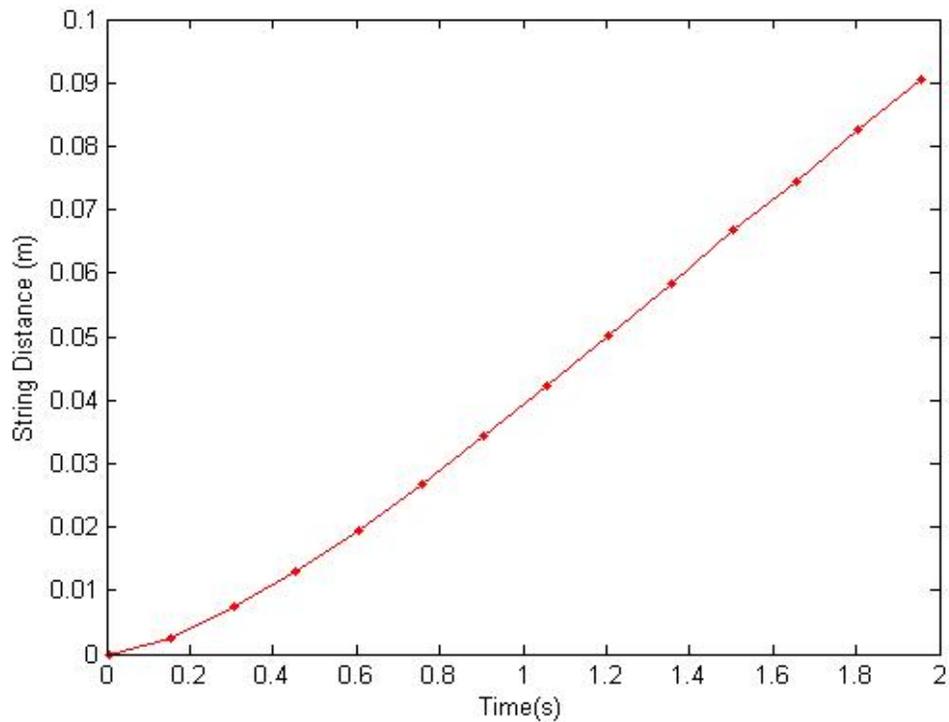
Figure 46: Integrated mean velocity (i.e. displacement) curve for Trial 1, showing a string displacement of 9.14 cm.

Table 12: String displacement estimation using proposed audio-based Fourier analysis technique.

Trial No.	Displacement (cm)	Trial No.	Displacement (cm)
1	9.14	11	9.05
2	9.30	12	9.22
3	8.40	13	9.10
4	8.60	14	9.03
5	9.03	15	8.93
6	9.60	16	9.32
7	9.57	17	8.99
8	9.43	18	9.08
9	9.24	19	9.27
10	9.14	20	9.30

7.2   Beef Flexor Tendon Displacement Measurement Accuracy Test

7.2.1   Experiment Set-Up

Similar to the previous experiment in Section 7.1, the experimental setup consists of a moving beef flexor tendon and pulley system that mimics the hand's tendon motion by allowing the beef tendon to slide by a known displacement under the LogicScan[TM] scanner (Figure 47). For the purpose of determining the accuracy of estimating the tendon displacement, the scanner's onboard processing and the proposed audio-based processing techniques are tested using 15 experimental trials. For each trial, the tendon is manually displaced by 3.0 cm ± 0.1 cm, and allowed to move under gravity as before.
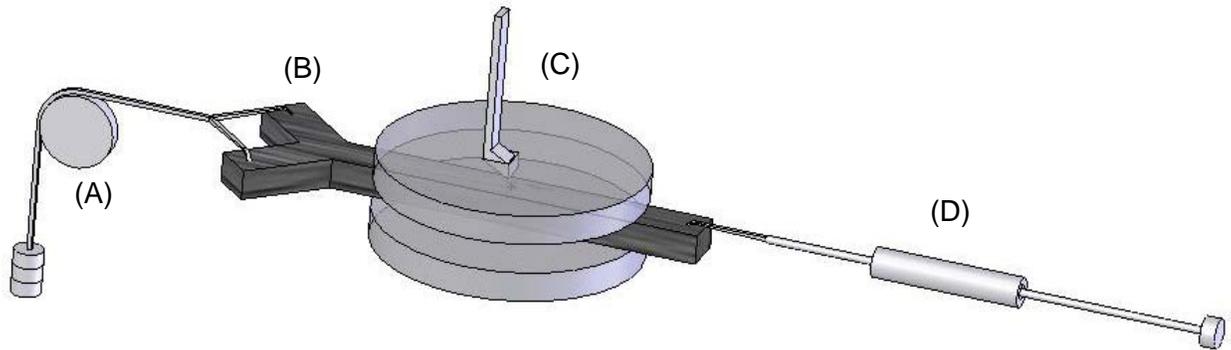

Figure 47: Schematic diagram of the experimental setup with (A) the 100 g mass, pulley and string, (B) the beef tendon, (C) 2 Aquaflex gel pads with cut-out wedge and transducer, and (D) string guide and stopper.

7.2.2   LogicScan[TM] Scanner's Onboard Software

The beef tendon is first located with LogicScan's transducer using the settings in Table 10. During the 15 trials, the beef tendon is displaced by moving the string and stopper 3.0 cm ± 0.1 cm. Figure 48 shows the resulting velocity spectrogram of the tendon displayed by LogicScan™ scanner's onboard software for Trial 1. The onboard software then performs the VTI to obtain the estimated displacements. These excursions for the 15 trials are shown in Table 13. The mean estimated displacement using LogicScan's onboard software for these trials is 2.91 cm with a standard deviation of 0.07 cm.
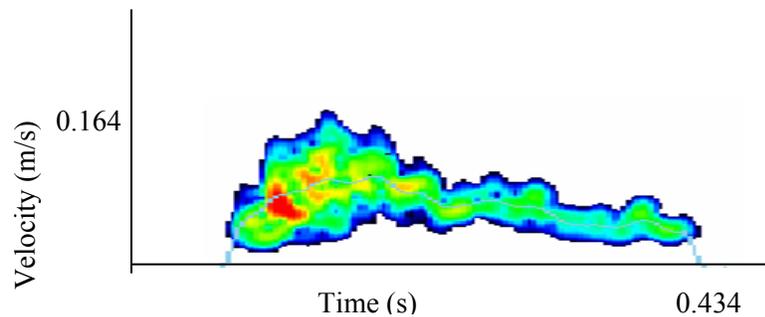
Figure 48: **LogicScan™ scanner's velocity spectrogram for Trial 1: tendon velocity vs. time.**

Table 13: Tendon displacement estimation using LogicScan's onboard software.

Trial No.	Displacement (cm)	Trial No.	Displacement (cm)
1	2.87	*9*	2.92
2	2.96	*10*	2.93
3	2.75	*11*	2.90
4	2.91	*12*	2.89
5	2.86	*13*	2.89
6	3.10	*14*	2.91
7	2.92	*15*	2.88
8	2.97		

7.2.3 Audio-based Doppler Signal Acquisition and Processing

For the previous 15 trials, the Doppler-shifted audio signal (shown in Figure 49) is simultaneously obtained in real-time using the Matlab™ data acquisition script presented in Section 6.4. The signal is then processed offline (only for the sake of simplicity) in order to determine the feasibility of the proposed techniques. Note that this signal contains noise from previous digitization step in the LogicScan™ scanner as well as from the soundcard. The noise is reduced by a factor of $\sqrt{30}$ using a 30-point moving

average filter. Since a moving average filter ultimately alters the characteristics of the signal, discretion is used in choosing a suitable sample size of the filter.

In order to determine the frequency content of the signal during small time intervals, a Short-Term Fourier Transform (STFT) is performed using the same methods as described in Section 6.4. The Doppler shifted velocities, intensity-weighted mean velocity (IWMV) and mean velocity curves are also obtained using the same methods as described in Section 6.4. For this experiment, the power spectral density is set to be greater than 80 dB to neglect low amplitude noise. Also, a lower frequency threshold is set at 150 Hz to eliminate low frequency noise. Using this custom Matlab™ script, the mean velocity points, fitted mean velocity curve and displacements (via integration) are estimated, as shown in Figures 50 and 51 for Trial 1. Using the proposed technique, the mean displacement from these trials is 2.98 cm with a standard deviation of 0.09 cm. The estimated displacements for all 15 trials are shown in Table 14.
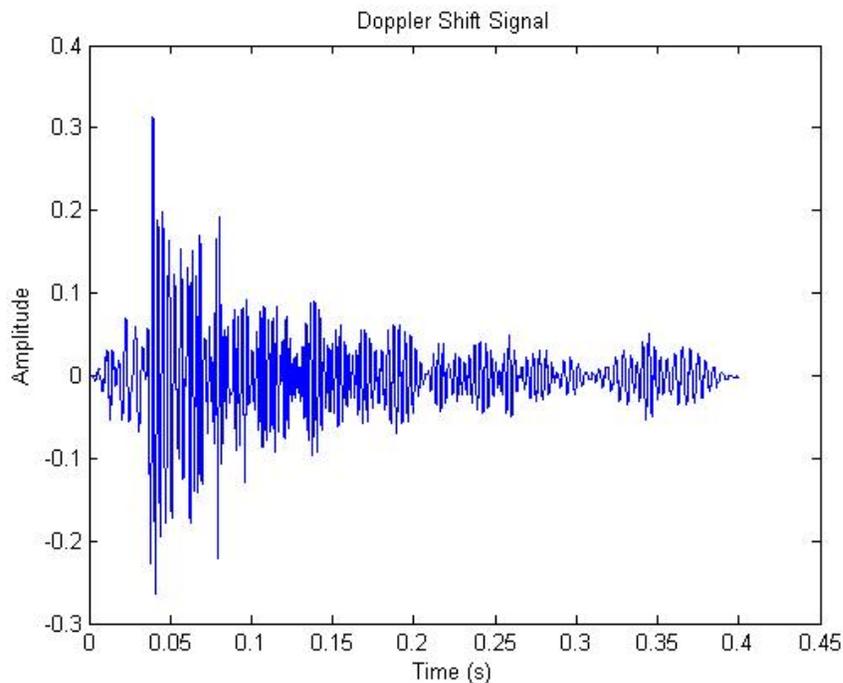
Figure 49: **Demodulated Doppler shifted audio signal.**
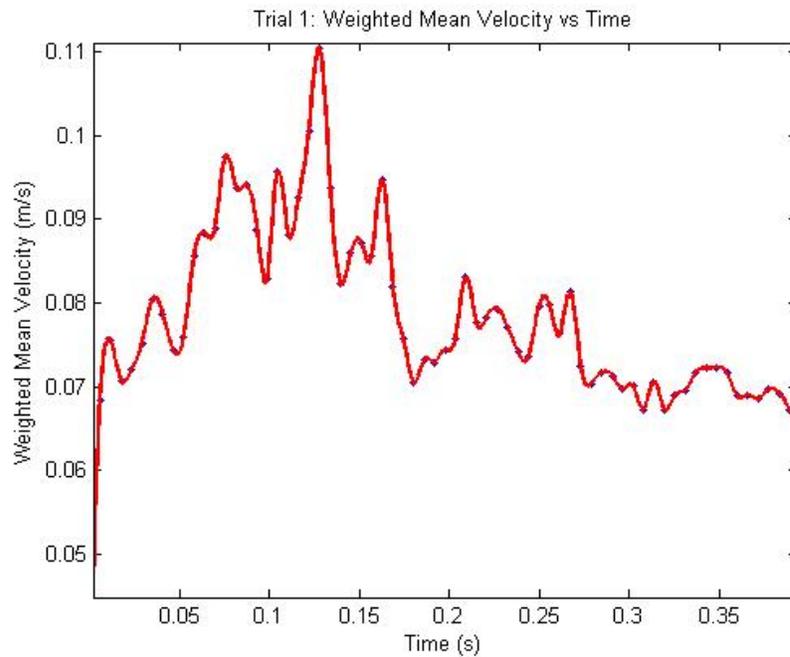
Figure 50: Mean velocity data points and fitted curve for Trial 1.
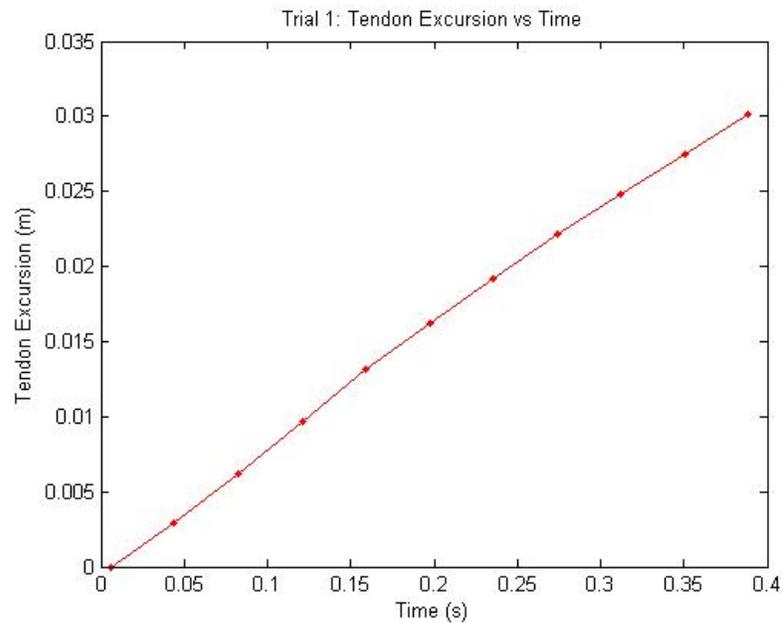
Figure 51: **Integrated mean velocity (i.e. displacement) curve for Trial 1, showing a tendon displacement of 3.02 cm.**

Table 14: Beef Tendon displacement estimation proposed audio-based Fourier analysis technique.

Trial No.	Displacement (cm)	Trial No.	Displacement (cm)
1	3.02	9	3.08
2	2.90	10	3.02
3	3.09	11	2.83
4	2.99	12	2.83
5	3.07	13	3.03
6	2.94	14	2.92
7	2.89	15	3.03
8	3.12		

Chapter 8

Robotic Finger Demonstration Using the Proposed Processing Technique

8.1   Acquiring, Processing and Validating the User-Intended Tendon Motion Signal

8.1.1   Experimental Set-Up

In order to estimate the tendon excursion experienced during the PIP joint rotation, the LogicScan^{TM} Doppler ultrasound scanner detects the Doppler shifted signal of the moving tendon (Figure 52). The LogicScan™ scanner collects the shift frequencies from the moving tendon with a 12 MHz transducer, which relays the signal to the portable scanner that is connected to a PC (as before). The transducer is set on top of an Aquaflex ^{TM} standoff wedge and holder. This signal is processed similarly to the previous experiments. The signal is filtered with a 50-point moving average filter and then a Short-Term Fourier Transform (STFT) is performed using the same methods as described in Section 6.4. The Doppler shifted velocities, intensity-weighted mean velocity (IWMV) and mean velocity curves are also obtained using the same methods as described in Section 6.4. For this experiment, the power spectral density is set to be greater than 85 dB to neglect low amplitude noise. Also, a lower frequency threshold is set at 100 Hz to eliminate low frequency noise.
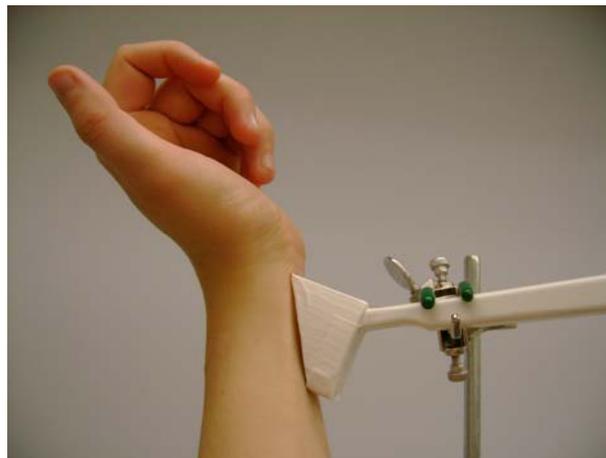
Figure 52: **Transducer and wedge placement on wrist.**

After the tendon is properly located (Section 8.1.2), the first part of the experiment obtains and processes the Doppler signal from the moving tendon (Section 8.1.3). Then, Section 8.1.4 and Section 8.1.5 contains a verification of the proposed Matlab^{TM} script by comparing its tendon excursion results to those estimated by standard models.

8.1.2   Locating the Index Finger's FDS Tendon

The LogicScan 128™ ultrasound machine and 12 MHz Linear Array transducer probe are set up as in Figure 52. The probe is positioned over the FDS tendon at the wrist level. Optimal transducer location is determined by using the Colour Doppler Mode on the ultrasound machine. This setting highlights the moving parts of a sample volume on the B-Scan image. By moving the index finger back and forth, the FDS tendon is highlighted in red and blue, respectively (Figure 53 A, B and C). The probe is moved along the tendon until an optimal Doppler angle could be used. This is difficult because the majority of the tendon's motion is perpendicular to the ultrasound beam. Therefore, a stand-off wedge is used between the probe and the skin surface to allow for a better Doppler angle. The acquiring site is at the wrist level because the FDS tendon changes direction slightly allowing for an estimated 59 º ± 1 º Doppler angle. The depth of the tendon is estimated using the ultrasound's software as 6.2 mm ± 0.2 mm below the skin's surface. Because of this shallow imaging depth, a 12 MHz transducer with a built-in smoothing filter is used. The other PW Doppler parameters used are shown in Table 15.

Table 15: Selected settings on the LogicScan ultrasound scanner.

Pulse Frequency = 1.5 kHz	Correction Angle = 59º
Gain = 88%	Sample Size = 1 mm
Power Level = 55%	Wall Filter = 7%
Steering Angle = -10º	Dynamic Range = 30 dB

(A)   (B)
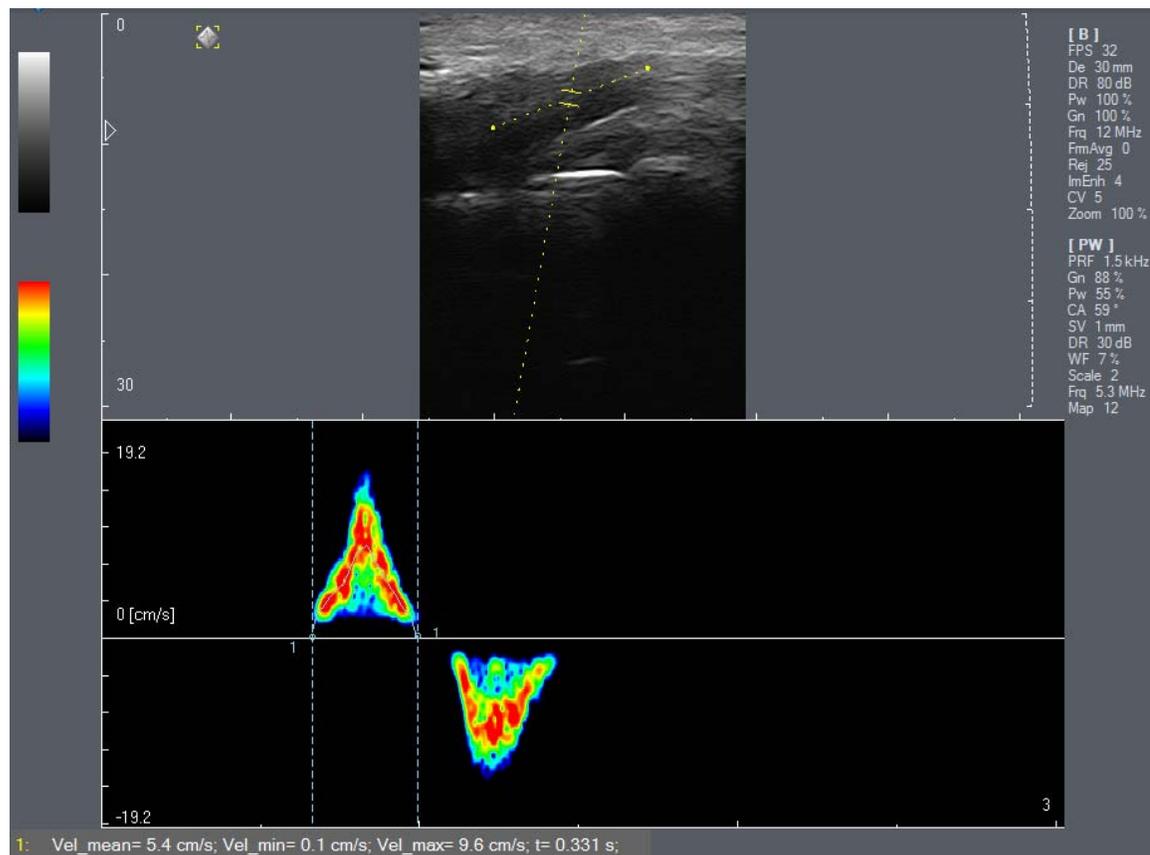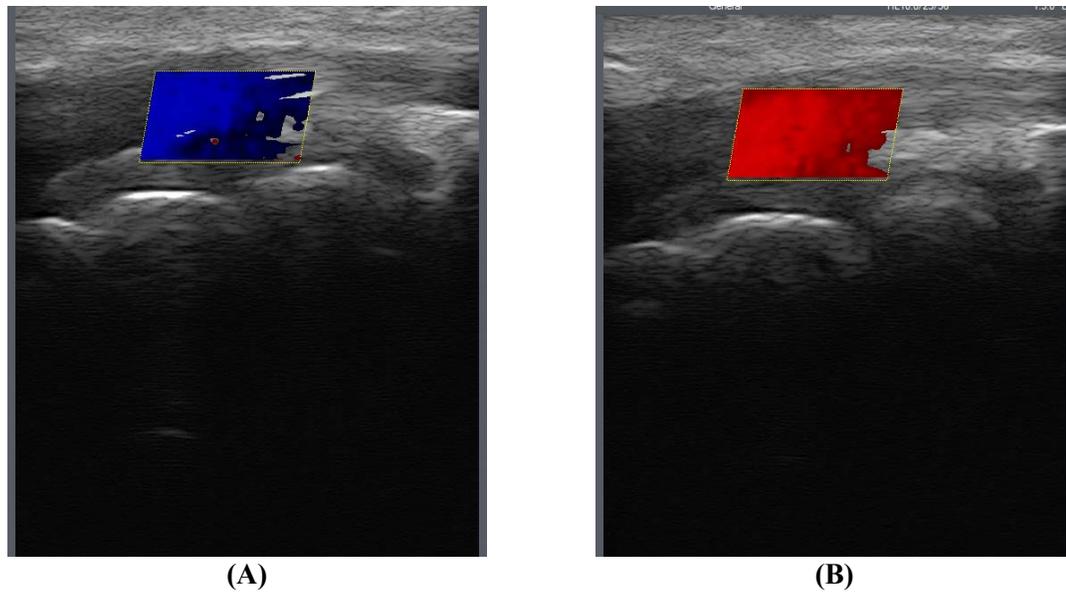
(C)

Figure 53: Colour Doppler image showing the tendon moving away (A) and towards (B) the transducer. A typical screen shot of the Duplex mode on the LogicScan™ display is shown in (C). Here, the moving FDS tendon is imaged and the resulting PW Doppler spectrogram is displayed.

8.1.3 The Doppler Shift Signals Obtained by the LogicScan[TM] and the Proposed Matlab[TM] Script

In order to further demonstrate the accuracy of the Matlab[TM] script, the PIP joint in the index finger is separately rotated from 0° to 35°, from 0° to 70°, from 0° to 80°, from 0° to 100° and from 0° to 110°. The DIP joint is kept passive and the MCP joint is fixed at 0°. The final angle for each total rotation is measured with a goniometer locked into the desired position since an active angle monitoring system like Visualeyez [TM] is not available for this experiment (Figure 54). Using the goniometer, the measured final rotation angles for each data set have an accuracy of ±2°. The LogicScan[TM] software detects the Doppler shifted signal of the moving tendon. The onboard software then performs the VTI to obtain the estimated displacements as before. This method is repeated in order to obtain 3 comparison trials, i.e., 3 sets of excursion and time data are obtained for the total rotation angle of 35°, 70°, 80°, 100°, and 110°. Figure 55 shows the resulting velocity spectrogram of the tendon displayed by the LogicScan's onboard software for 80° of total rotation in Trial 2. The total excursions for the total joint rotations of 35°, 70°, 80°, 100°, and 110° for the 3 trials are shown in Table 16 along with the mean estimated total displacement and standard deviation using LogicScan's onboard software.
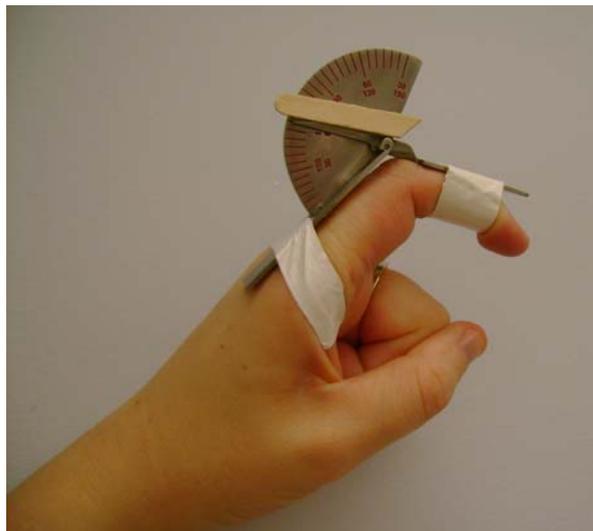
Figure 54: Goniometer placement. The MCP joint is suppressed, and the total angular rotation is fixed at the required angle.

0.113 m/s

Velocity (m/s)

0.234 s

Time (s)
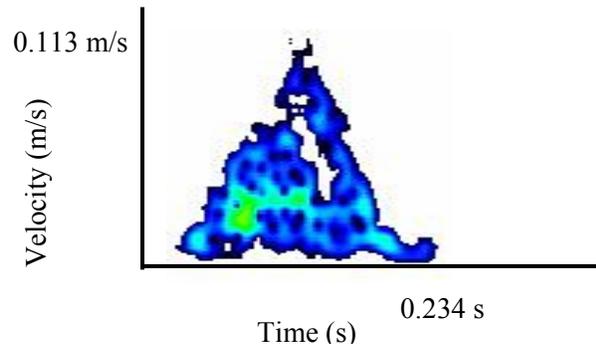
Figure 55: **The LogicScan^{TM} scanner's velocity spectrogram for 80 degrees of rotation in Trial 2**

Table 16: Total tendon displacement estimation using LogicScan's onboard software.

TRIAL 1	35° PIP Rotation	70° PIP Rotation	80° PIP Rotation	100° PIP Rotation	110° PIP Rotation
Total Tendon Excursion (mm)	3.3	6.7	8.0	8.2	11.5
TRIAL 2	35° PIP Rotation	70° PIP Rotation	80° PIP Rotation	100° PIP Rotation	110° PIP Rotation
Total Tendon Excursion (mm)	3.2	7.3	7.7	8.1	12.1
TRIAL 3	35° PIP Rotation	70° PIP Rotation	80° PIP Rotation	100° PIP Rotation	110° PIP Rotation
Total Tendon Excursion (mm)	3.3	6.7	8.5	7.8	12.1
Mean Total Displacement (mm)	3.27	6.90	8.07	8.03	11.90
Standard Deviation (mm)	0.06	0.35	0.40	0.21	0.35

For the previous 3 trials of joint rotation data, the Doppler-shifted audio signal is simultaneously obtained in real-time using the data acquisition script in Matlab™. The signal is then processed offline (only for the sake of simplicity) in order to determine the feasibility of the proposed techniques. As mentioned earlier, the raw Doppler signal contains noise, which is mostly filtered out using a 50-point moving average filter. Using the previously described custom Matlab™ script, the Doppler shifted signal, the velocity spectrogram, the mean velocity points, fitted mean velocity curve and displacements (via integration) are estimated, as shown in Figures 56-59 for the 80° joint rotation data in Trial 2. The total tendon excursions for the total joint rotations of 35°, 70°, 80°, 100°, and 110° for the 3 trials are shown in Table 17. The mean estimated total displacement and standard deviation using the proposed processing method for these trials are summarized at the end of Table 17. Overall, there is less variability in the tendon excursions that are processed with the proposed method (Table 17) in comparison to the LogicScan's displayed results (Table 16). In the subsequent sections, the validity of the tendon excursions estimated by both methods is tested by comparing them to the tendon excursions that are estimated by standard models (Section 8.1.4 and 8.1.5).
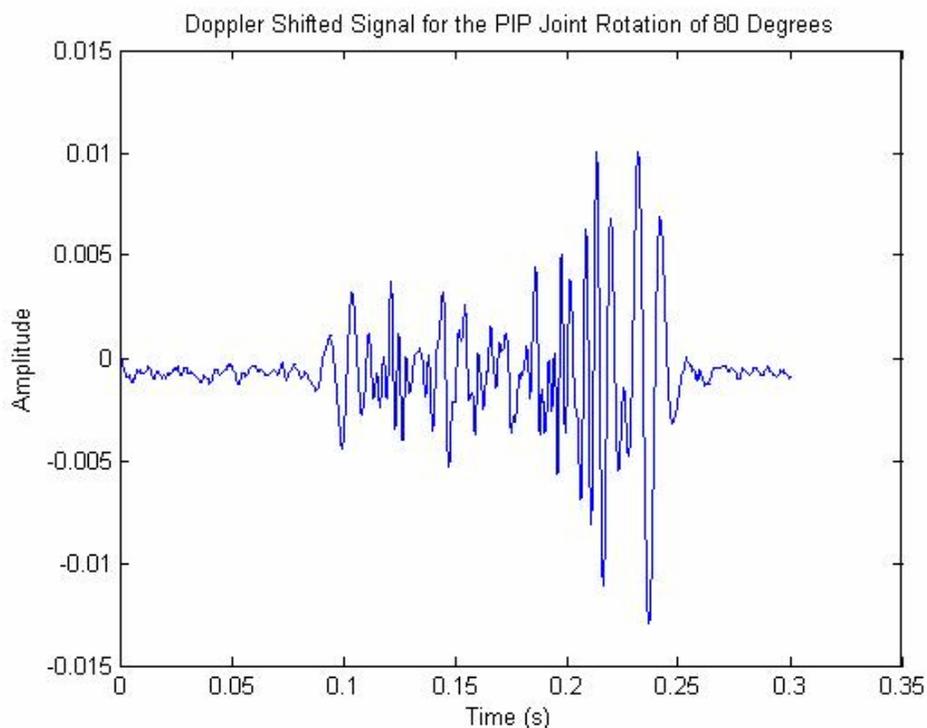
Figure 56: Demodulated Doppler shifted Signal for the PIP joint rotation of 80 ° for Trial 2.
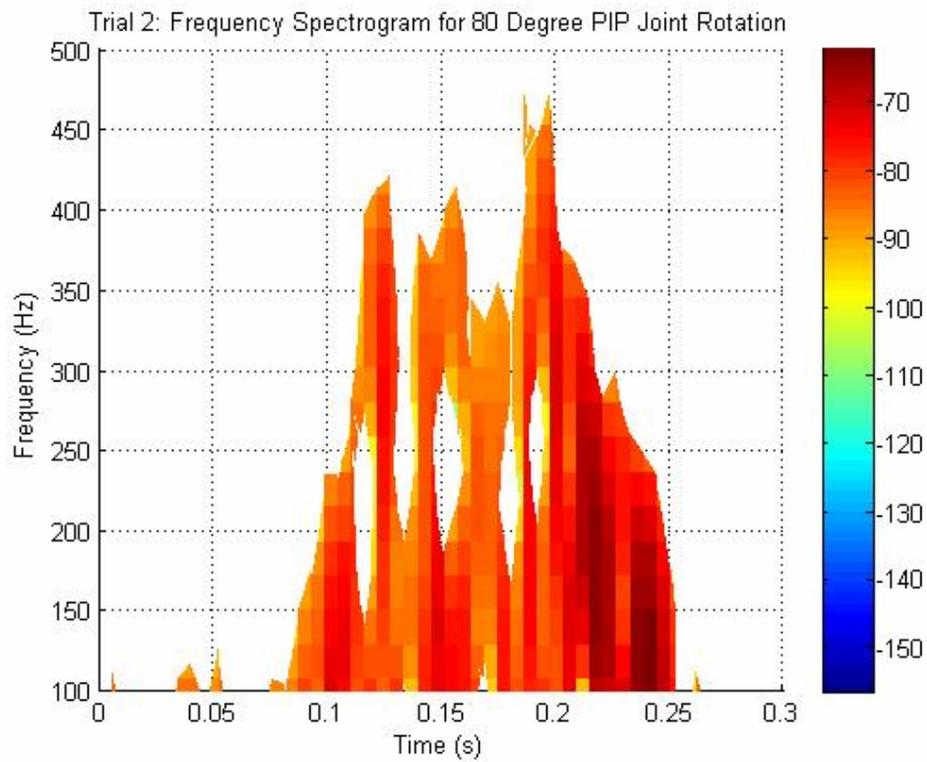
Figure 57: **Frequency Spectrogram for the 80 degree PIP Joint Rotation for Trial 2.**
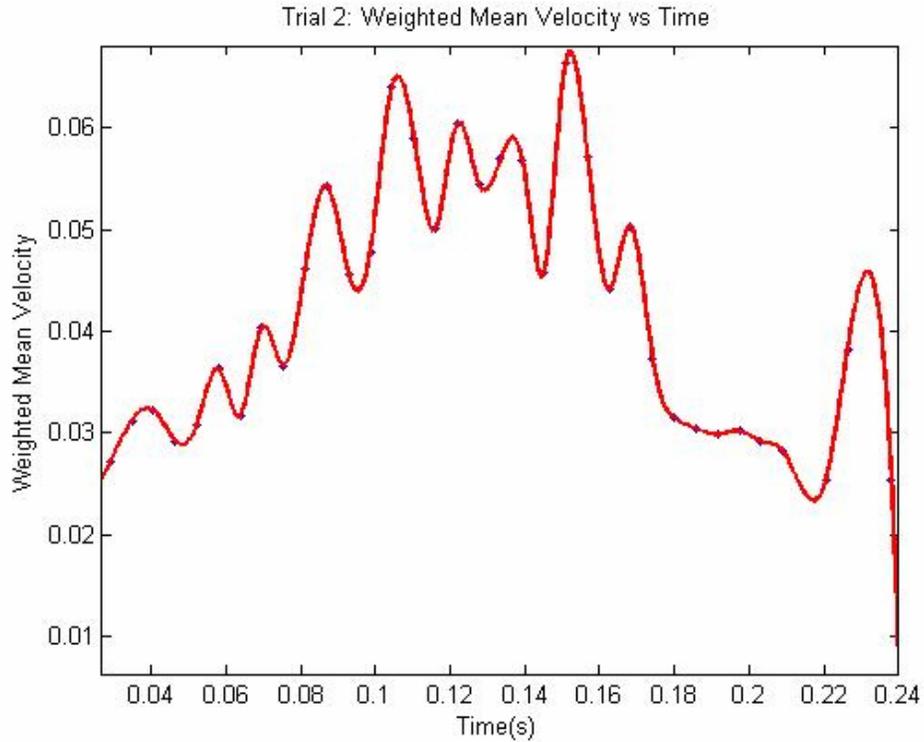
Figure 58: Weighted mean velocity data points and fitted mean velocity curve for the 80 degree PIP Joint Rotation for Trial 2.
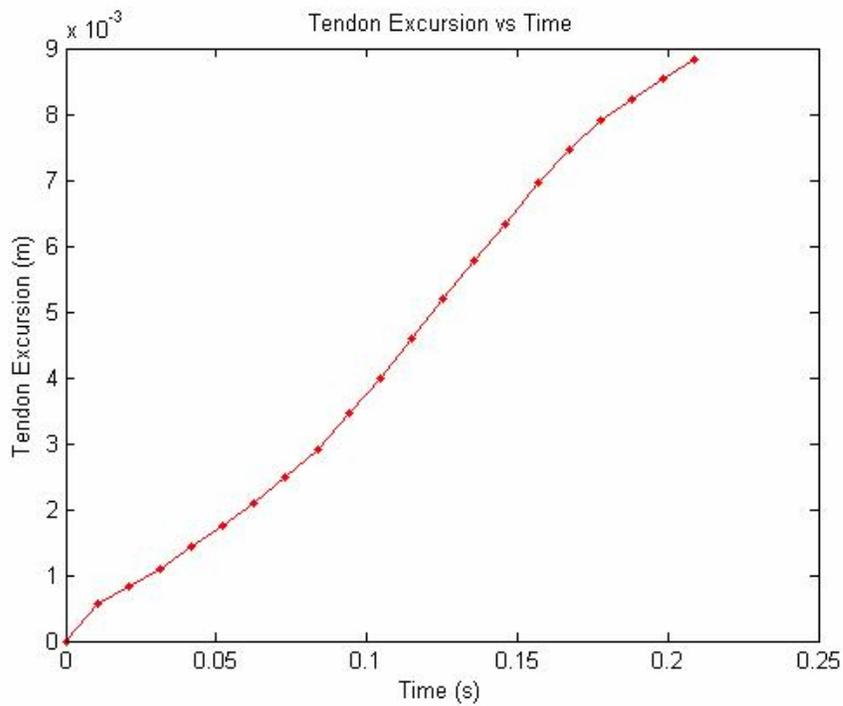
Figure 59: **Integrated mean velocity (i.e. displacement) curve for the 80 degree PIP Joint Rotation for Trial 2, showing a tendon displacement of 8.8 mm**

Table 17: Total tendon displacement estimation using the proposed processing Matlab™ method

TRIAL 1	35° PIP Rotation	70° PIP Rotation	80° PIP Rotation	100° PIP Rotation	110° PIP Rotation
Total Tendon Excursion (mm)	3.6	7.1	8.4	10.4	11.5
TRIAL 2	35° PIP Rotation	70° PIP Rotation	80° PIP Rotation	100° PIP Rotation	110° PIP Rotation
Total Tendon Excursion (mm)	3.4	7.3	8.8	10.2	11.7
TRIAL 3	35° PIP Rotation	70° PIP Rotation	80° PIP Rotation	100° PIP Rotation	110° PIP Rotation
Total Tendon Excursion (mm)	3.7	7.6	8.8	10.3	11.8
Mean Total Displacement (mm)	3.57	7.33	8.67	10.3	11.67
Standard Deviation (mm)	0.15	0.25	0.23	0.1	0.15

8.1.4 Brand and Hollister Model: Correlating Tendon Excursion to PIP Joint Rotation Angles

In order to further validate the total tendon excursions that are estimated using the proposed Matlab™ script (or the LogicScan™ software), the estimated total tendon displacements should be compared to the actual total displacements experienced from PIP rotation. This is a complicated task because the actual tendon displacements can only be measured non-invasively in these experiments. However, an accepted model in the literature correlates the rotation angle of the joint with the tendon excursion experienced

[107]. Referring to Figure 60, the rotation angle θ can be estimated if the tendon excursion D and radius m of the joint (moment arm) is known. This model assumes that the tendon is free to move and is not limited by adhesions and interconnections.

$$D = m\theta \tag{23}$$

Where:

θ is the rotation angle in radians

D is the tendon excursion

m is the moment arm (joint radius and tendon thickness)
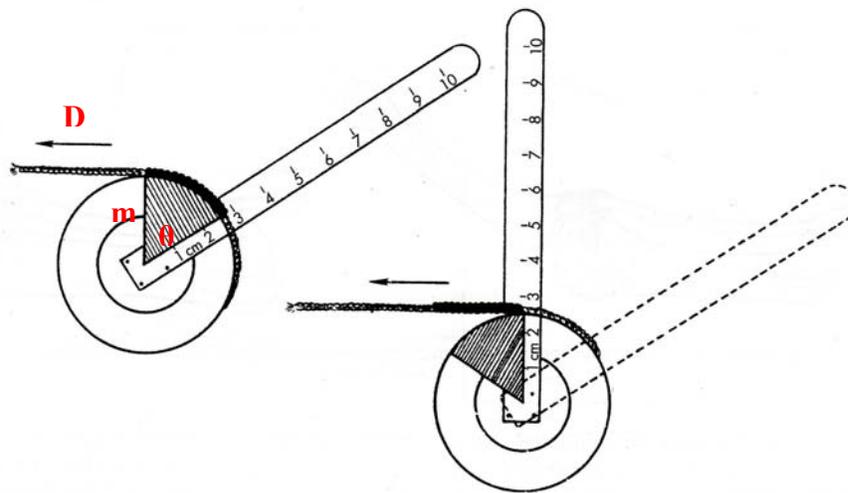
Figure 60: **Lengthwise tendon excursion from joint rotation [107].**

Using the tendon pulley model described by Equation (23), the total tendon excursions can be estimated by using the final rotation angles measured with the goniometer and an approximated moment arm. The simplest approximation of the moment arm of the PIP joint is to measure the joint, tendon and skin diameter with a digital calliper. This moment arm is half of this measured diameter. The digital calliper estimates this diameter as 12.07 mm, giving an estimated moment arm of 6.04 mm ± 0.01 mm. Using this moment arm, Equation (23) and the rotation angles measured with the goniometer (35°, 70°, 80°, 100°, and 110°), the total tendon excursions can be estimated and compared to the Matlab™ and LogicScan™ estimations. As shown in Table 18, the total tendon displacements that are estimated by this method are most comparable to

those processed by the script in Matlab^{TM}.

Table 18: Total tendon displacement estimation using the Brand and Hollister model [107].

	35° PIP Rotation	70° PIP Rotation	80° PIP Rotation	100° PIP Rotation	110° PIP Rotation
Total Tendon Excursion (mm)	3.69	7.38	8.43	10.54	11.60

For comparison, the moment arm can also be approximated using the total tendon excursions estimated by the proposed processing script in Matlab^{TM}. For each of the 3 trials, the total tendon excursion estimated by the Matlab^{TM} script is plotted against its corresponding final rotation angle (measured with the goniometer) using Table 17 (Figures 61-63). A linear interpolation is fit to these plots in order to estimate the slope (or moment arm), as is shown in Table 19. Using Equation (23) and the slope on each plot, the average moment arm is estimated as 6.03 mm with a standard deviation of 0.058 mm. This is comparable to the moment arm that is estimated by the digital calliper.

Table 19: The estimated moment arms from Figures 59-61.

Trial	Estimated Moment Arms (mm)
1	6.0
2	6.0
3	6.1
Mean	**6.03 mm (standard deviation 0.058 mm)**
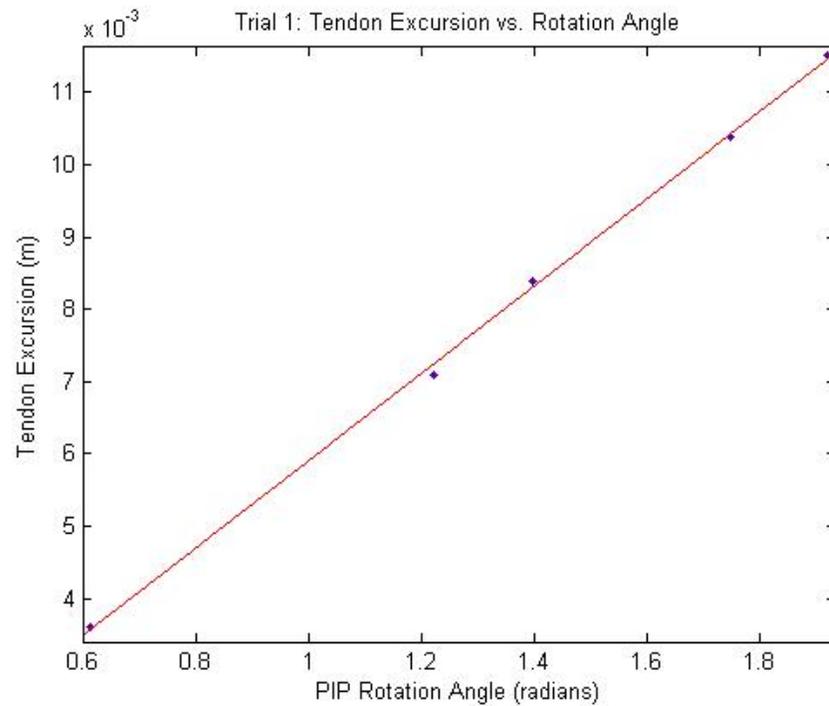
Figure 61: Tendon Excursion (m) vs. PIP Rotation Angle (radians) plot for Trial 1. The fitted linear polynomial estimates a moment arm of 6 mm.
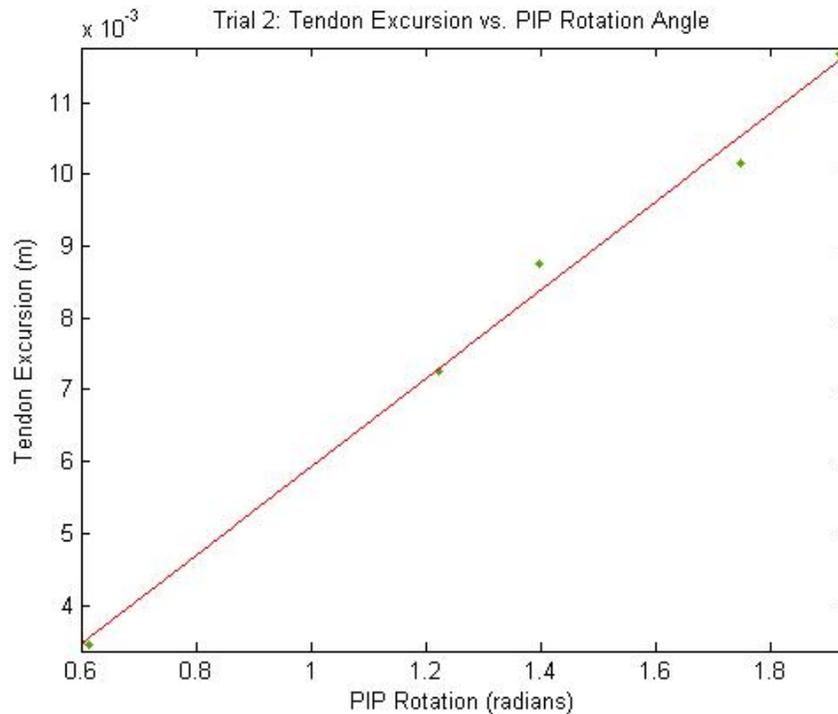
Figure 62: Tendon Excursion (m) vs. PIP Rotation Angle (radians) plot for Trial 2. The fitted linear polynomial estimates a moment arm of 6 mm.
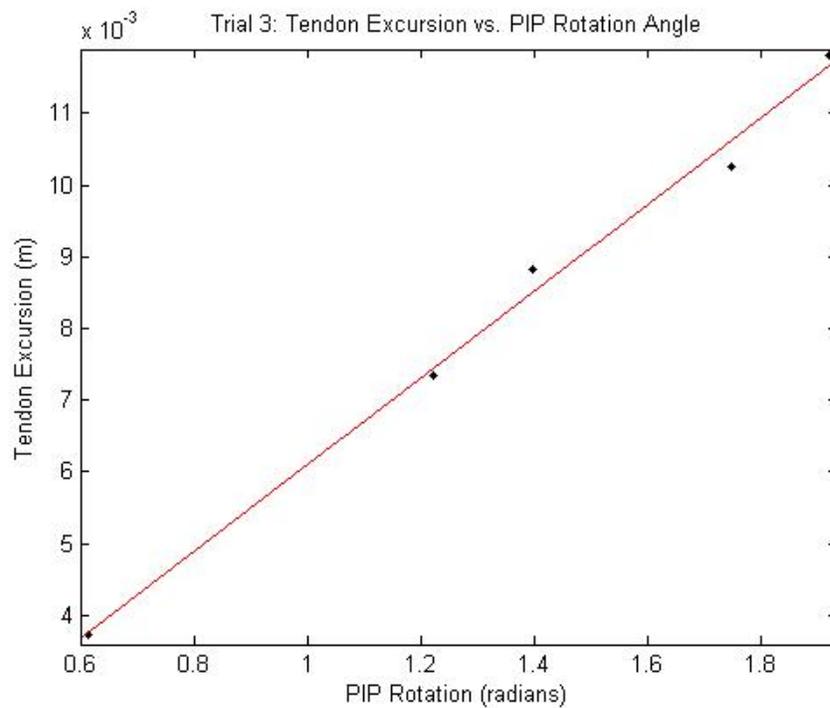
Figure 63: Tendon Excursion (m) vs. PIP Rotation Angle (radians) plot for Trial 3. The fitted linear polynomial estimates a moment arm of 6.1 mm.

8.1.5   Minimum Jerk Profile

In order to further validate the tendon excursions estimated by the proposed processing Matlab^{TM} script, the tendon excursions can be compared to another accepted model. As described by Bundhoo et.al. [122], jerk is an accepted quantity of evaluating motor smoothness of the human limbs. It is defined as the time derivative of acceleration, and each joint should smoothly follow a trajectory that minimizes the sum of the square jerk, i.e:

$$\text{minimize } J = \frac{1}{2} \int_{t1}^{t2} \dddot{\theta}(t)^2 \, dt \tag{24}$$

Where:

J is the jerk, and $\dddot{\theta}$ is the jerk of the trajectory $\theta(t)$

The general solution to equation is:

$$\theta(t) = A_0 + A_1 t + A_2 t^2 + A_3 t^3 + A_4 t^4 + A_5 t^5 \tag{25}$$

Where:

A_0 to A_5 are constant parameters

By setting $D = t_f - t_i$ in Equation (25) and using the conditions $\theta(t_i) = \theta_i$ and $\theta(t_f) = \theta_f$, Equation (25) becomes:

$$\theta(t) = \theta_i + (\theta_f - \theta_i) * \left(10 \left(\frac{t}{D} \right)^3 - 15 \left(\frac{t}{D} \right)^4 + 6 \left(\frac{t}{D} \right)^5 \right) \tag{26}$$

For the sake of simplicity, the tendon excursions as a function of time processed by the proposed Matlab[TM] script for the third 70 ° trial are used for comparison to the Minimum Jerk model (Table 20). The tendon excursions as a function of time determined by the Matlab[TM] script are translated into rotation angles as a function of time using the Brand and Hollister approximation and the average moment arm determined in Section 8.1.4 (6.03 mm) for the Matlab[TM] processed excursions. The corresponding rotation angles are shown in Table 21. The final rotation angle is estimated as 73.0 degrees using this method. This value is comparable to the total rotation angle measured by the goniometer (70°±2°).

Table 20: Tendon excursions and time for the third trial of 70 degree rotation, showing a total tendon displacement of 0.764 cm. The total rotation took place in 0.205 seconds.

Tendon Excursion (cm)	Time (s)	Tendon Excursion (cm)	Time (s)
0.000	0.000	0.449	0.105
0.005	0.005	0.489	0.110
0.007	0.010	0.529	0.115
0.002	0.015	0.577	0.120
0.013	0.020	0.625	0.125
0.006	0.025	0.662	0.130
0.026	0.030	0.692	0.135
0.046	0.035	0.718	0.140
0.071	0.040	0.743	0.145
0.098	0.045	0.757	0.150
0.119	0.050	0.764	0.155
0.140	0.055	0.777	0.160
0.165	0.060	0.777	0.165
0.194	0.065	0.784	0.170
0.224	0.070	0.775	0.175
0.251	0.075	0.790	0.180
0.281	0.080	0.792	0.185
0.316	0.085	0.786	0.190
0.348	0.090	0.779	0.195
0.375	0.095	0.784	0.200
0.408	0.100	**0.764**	**0.205**

Table 21: Estimated angular positions of Trial 3's 70 degree (goniometer) rotation. The total rotation estimated by the Matlab^{TM} script is 73.0 degrees.

Angular Position (degrees)	Time (s)	Angular Position (degrees)	Time (s)
0.00	0.000	42.88	0.105
0.50	0.005	46.68	0.110
0.70	0.010	50.52	0.115
0.20	0.015	55.08	0.120
1.24	0.020	59.64	0.125
0.61	0.025	63.19	0.130
2.52	0.030	66.04	0.135
4.39	0.035	68.54	0.140
6.76	0.040	70.94	0.145
9.35	0.045	72.30	0.150
11.32	0.050	73.00	0.155
13.34	0.055	74.20	0.160
15.72	0.060	74.20	0.165
18.53	0.065	74.90	0.170
21.36	0.070	74.00	0.175
23.99	0.075	75.40	0.180
26.87	0.080	75.60	0.185
30.16	0.085	75.10	0.190
33.19	0.090	74.40	0.195
35.81	0.095	74.90	0.200
38.98	0.100	**73.00**	**0.205**

Using Equation (26), the total time, and the data presented in Table 21, the Minimum Jerk profile and the proposed Matlab^{TM} method is compared for accuracy. The Minimum Jerk's angular profile is shown in Table 22 (using the same time steps as in the Matlab^{TM} script) and displayed in Figure 64 along with the proposed method's angular profile for comparison.

Table 22: Calculated minimum jerk rotational position using the same time steps as the Matlab[TM] method in Table 21. The total rotation angle is estimated as 70.8 degrees.

Angular Position (degrees)	Time (s)	Angular Position (degrees)	Time (s)
0.00	0.000	37.02	0.105
0.01	0.005	40.24	0.110
0.08	0.010	43.41	0.115
0.25	0.015	46.51	0.120
0.57	0.020	49.51	0.125
1.06	0.025	52.37	0.130
1.76	0.030	55.08	0.135
2.68	0.035	57.60	0.140
3.84	0.040	59.93	0.145
5.24	0.045	62.04	0.150
6.88	0.050	63.92	0.155
8.76	0.055	65.56	0.160
10.87	0.060	66.96	0.165
13.20	0.065	68.12	0.170
15.72	0.070	69.04	0.175
18.43	0.075	69.74	0.180
21.29	0.080	70.24	0.185
24.29	0.085	70.55	0.190
27.39	0.090	70.72	0.195
30.56	0.095	70.79	0.200
33.78	0.100	**70.80**	**0.205**
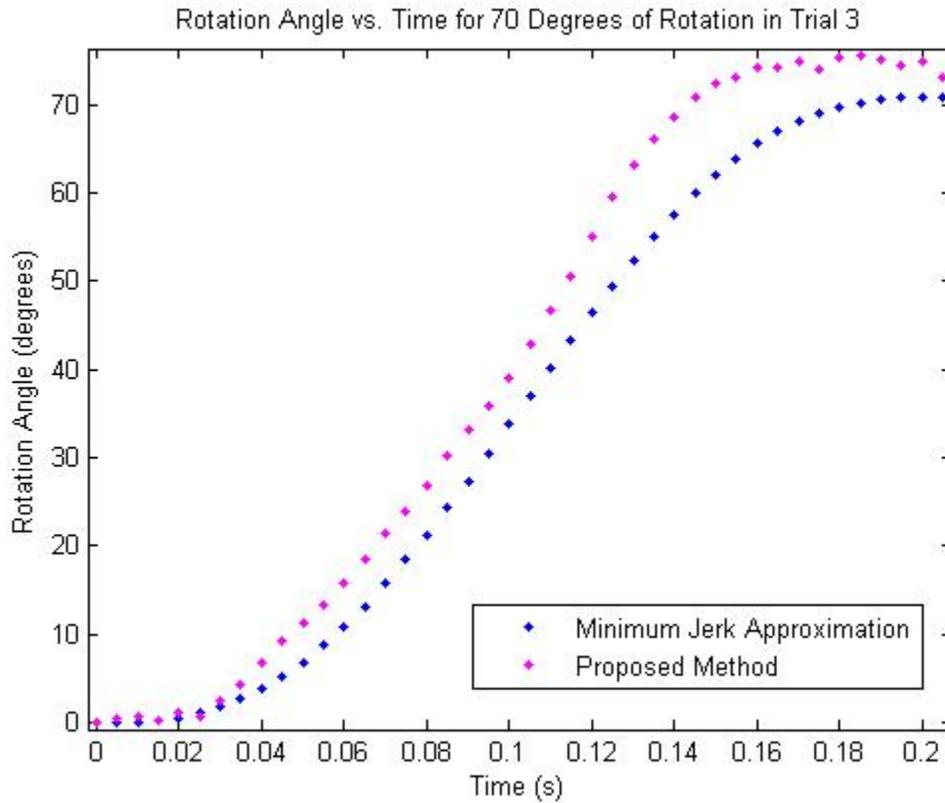
Figure 64: **The angular profile of the proposed sensing method in comparison to the angular profile of the Minimum Jerk approximation.**

For the proposed method, the initial and final rotation data points in Figure 64 are not as smooth as the Minimum Jerk approximation's angular profile. This is mainly due to the fact that the moment arm is assumed to be constant throughout rotation (Brand and Hollister model) when translating the tendon excursion into rotation angles for the proposed method in Matlab^{TM} . Therefore, the rotation angles that are calculated using Equation (23) will have inaccuracies in the regions where the moment arm is not constant. This is discussed further in Chapter 9.

8.2   Controlling the Robotic Finger

8.2.1   The Robotic Finger System

As shown in Figures 65 A and B, the robotic finger testbed used in this demonstration is a 4 degree-of-freedom (DOF) biomimetic design with shape memory alloy (SMA) actuation [122]. The testbed itself is kinematically and anthropomorphically accurate physical model of the natural human hand. The artificial index finger has 2 degree-of-freedom articulations of the MCP joint. The PIP and DIP joints are modeled as hinge joints since they are 1 degree-of-freedom joints with articulations in the plane perpendicular to the palmar hand surface (Figure 66).The range of motion of these joints are summarized in Table 23.
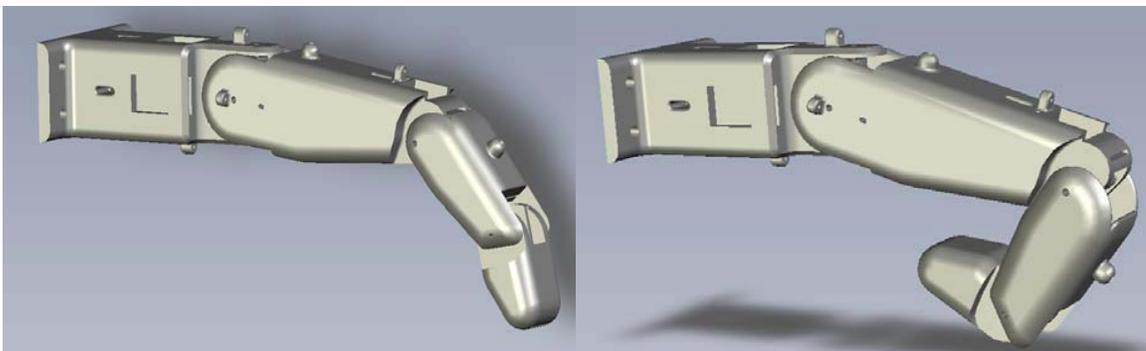
Figure 65: (A) the normal resting state of the robotic finger, and (B) the flexed state [122].
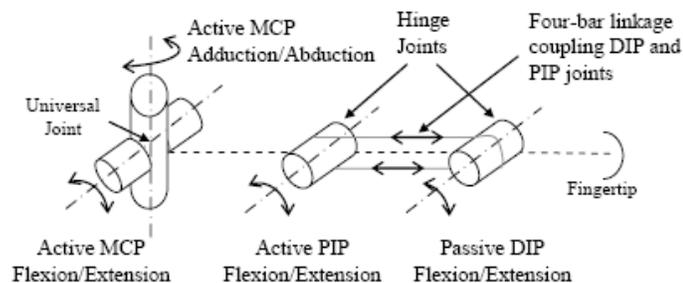
Figure 66: **Kinematic architecture of the artificial finger [122].**

The experimental set up includes the artificial finger, SMA actuators, a tendon mimicking microfibre line, a proportional controller, optical breadboard, data acquisition board, and a computer with LabVIEW™ software (Figures 67 A,B).
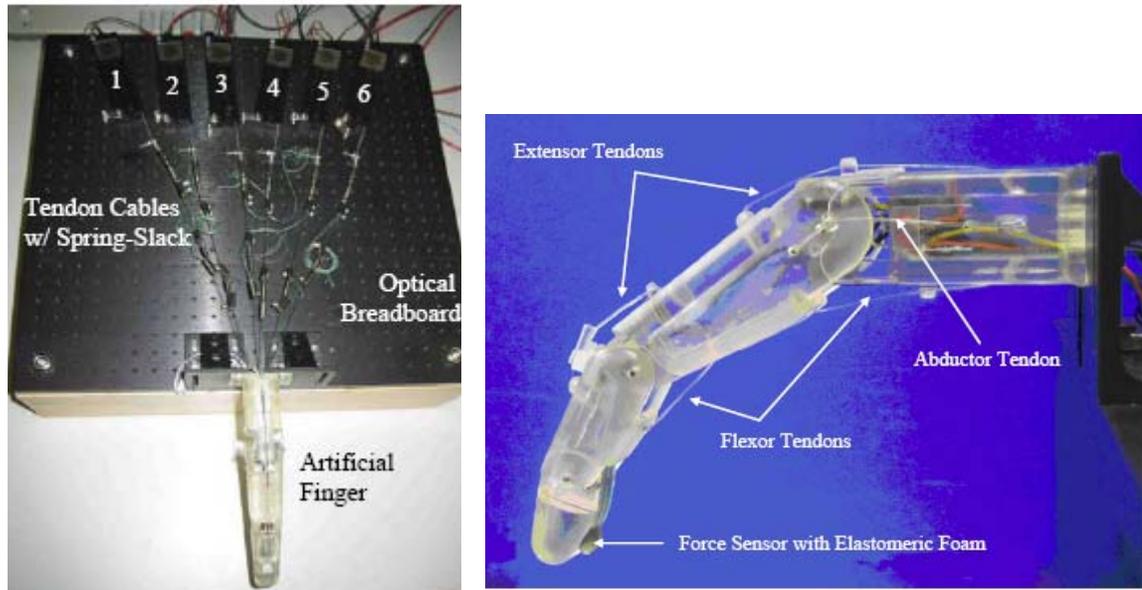
Figure 67: (A) Artificial finger and 6 SMAs mounted on an optical board, and (B) the artificial finger prototype [122].

Table 23: Range of motion of the artifical finger [122].

Joint	Range of Motion (Degrees)
MCP Adduction/Abduction	40
MCP Flexion/Extension	90
DIP Flexion/Extension	100-110
PIP Flexion/Extension	80

8.2.2   Calibrating the Robotic Finger

To provide a validation of the new sensing strategy presented in this thesis, the robotic finger's PIP rotation must be calibrated in order to have a proper comparison method. Because the robotic finger's software interprets angular position in terms of analogue-to-digital (A/D) counts, a calibration method must be devised to correlate A/D counts to rotational position. This calibration will allow for the input of data in Table 21

(from the proposed sensing method), as well as the robotic finger's output data to be converted to angular position for comparison.

Therefore, the calibration of the various joint angle sensors is performed using a goniometer designed for human finger joint angle measurement. The artificial finger's PIP joint is moved to 0°, 10°, 20°, 30°, 40°, 50°, 60°, and 70° in separate trials (each with accuracy ± 1°) and the corresponding A/D counts are recorded and shown in Table 24. By plotting the robot's PIP rotation angles as a function of A/D counts and fitting an exponential curve in Matlab^{TM}, the calibration is achieved and the relationship between A/D counts and rotation angle is known (Figure 68). This will allow for the robot's output of A/D counts to be converted into rotation angles for comparison. The fitted exponential equation that correlates rotational position to A/D counts is shown in Equation (27):

$$\theta(C) = e^{-\left(\frac{C-562.8}{55.83}\right)}$$
(27)

Where:

$\theta(C)$ is the angular position (degrees)

C is the A/D counts

Table 24: A/D counts and rotational angles for calibrating the robot finger

Angular Position (degrees)	A/D Counts
0	622
10	433
20	391
30	370
40	359
50	346
60	335
70	324
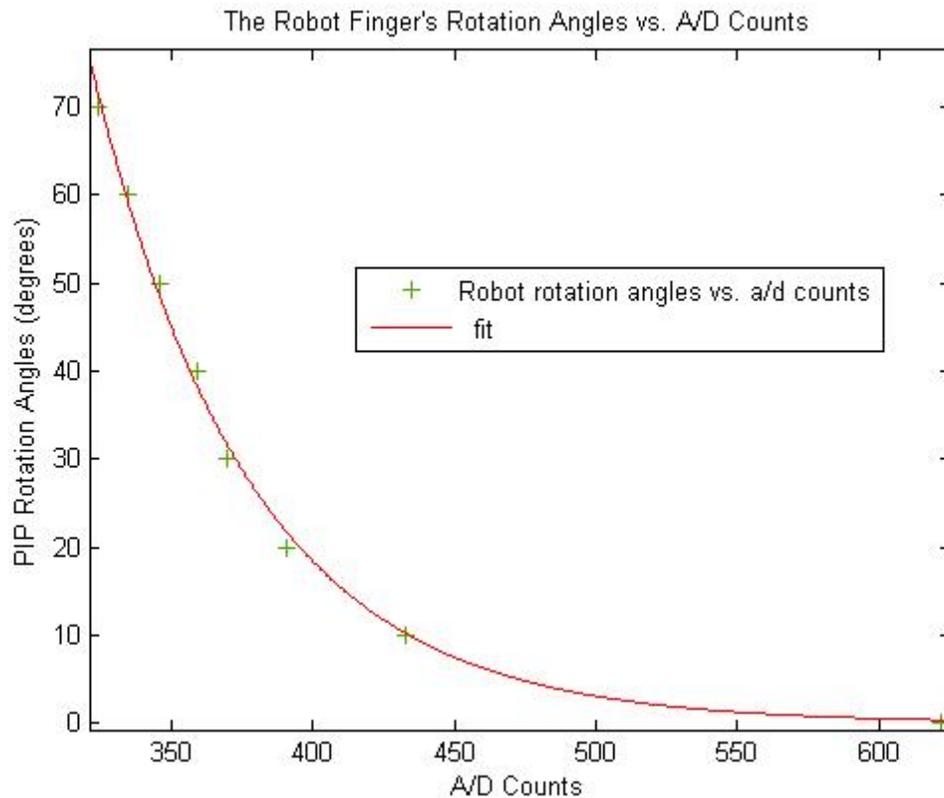
Figure 68: **Correlating the robot finger's output rotation angles and A/D Counts by fitting an exponential curve.**

Similarly, the A/D counts as a function of rotation angle must be known in order to input the proposed method's angular information to the robot's software. The robot finger's data from Table 24 is plotted and a natural logarithmic curve is fit (Figure 69). The fitted logarithmic equation that correlates A/D counts to rotational position is shown in Equation (28):

$$C(\theta) = -55.83\ln(\theta) + 562.6 \tag{28}$$

Where:

$\theta(C)$ is the angular position (degrees)

C is the A/D counts

Not surprisingly, Equation (27) and Equation (28) are inverses of each other.
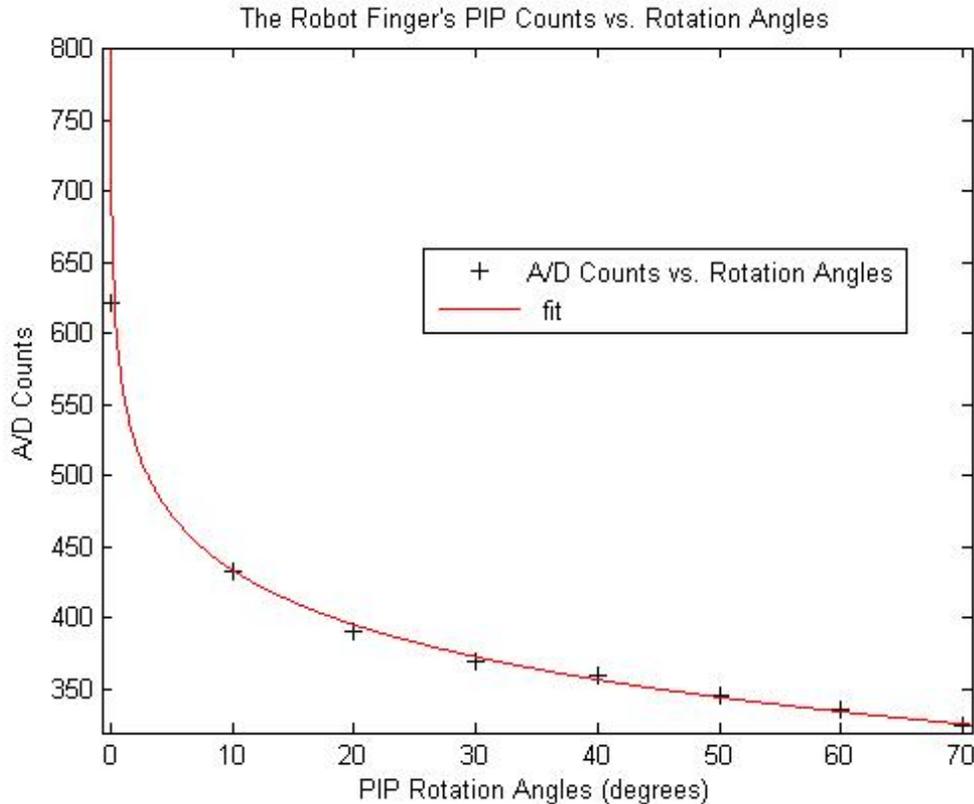
Figure 69: Correlating the robot finger's A/D Counts to rotation angles by fitting logarithmic curve.

The rotation angles that are estimated from the processed user intended tendon motion signal in Table 21 are used as an input to control the robotic finger. This is because in order to demonstrate robotic finger control, the input signal data should be from one set of tendon excursion vs. time data that is converted to rotation angles vs. time using the estimated moment arm and Equation (23). This is because the eventual goal of this work is to automate the entire process and have real-time acquisition, processing and robotic control. Also, the robotic finger's software is set up to have rotation angles converted to A/D counts as an input.

These angles from the third 70° trial are converted to A/D counts using Equation (28), and are shown in Table 25 and Figure 70.

Table 25: A/D counts and rotational angles for calibrating the input data using the proposed method

Angular Position (degrees)	A/D Counts	Angular Position (degrees)	A/D Counts
0.00	640	42.88	353
0.50	601	46.68	348
0.70	583	50.52	344
0.20	652	55.08	339
1.24	550	59.64	334
0.61	591	63.19	331
2.52	511	66.04	329
4.39	480	68.54	327
6.76	456	70.94	325
9.35	438	72.30	324
11.32	427	73.00	323
13.34	418	74.20	322
15.72	409	74.20	322
18.53	400	74.90	322
21.36	392	74.00	322
23.99	385	75.40	321
26.87	379	75.60	321
30.16	372	75.10	321
33.19	367	74.40	322
35.81	363	74.90	322
38.98	358	73.00	323
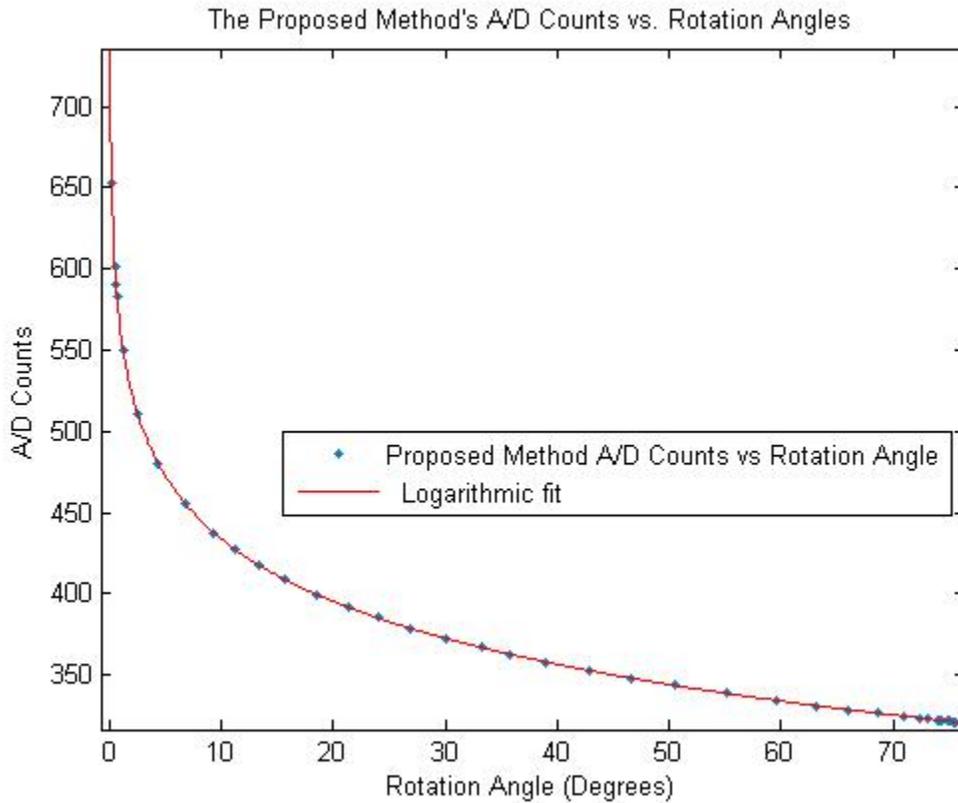
Figure 70: Correlating the proposed method's A/D counts to rotation angles by using the fitted logarithmic curve.

8.2.3   Controlling the Robotic Finger

The rotation angles that are estimated from the processed user intended tendon motion signal are used as an input to control the robotic finger. These angles from the third 70° trial are converted to A/D counts using the calibration method described in Section 8.2.2, and are entered into a lookup table on the LabVIEW™ software. The robotic finger's software interprets this data and rotates to the specified locations with SMA actuation. This is accomplished by applying a voltage to heat the SMA wire internals.

Once the robot's PIP flexion is completed, a vector of A/D counts over the joint's range of motion is produced from LabVIEW™. The protocol for this demonstration is to use the fitted exponential curve (Equation (27)) from the calibration section 8.2.2 to convert these A/D counts back to joint rotation angles. The resulting A/D counts and rotation angles for this trial is displayed in Table 26. A comparison plot is then produced

to show the rotation angles from the processed tendon motion (Table 21) and minimum

jerk approximation (Table 22), with the rotation angles estimated from the robot finger.

Because the robot finger and the human finger all rotate at different rates, the slopes from

the curves will be different. Furthermore, the robot finger took 17.9 s to complete

rotation, and the proposed method took 0.205 s. A scaling factor is applied to the time on

the x-axis (illustrated in Figure 71) for better comparison.

Table 26: The robot finger's output A/D counts and rotation angles of the Matlab^{TM} input data.

Counts	Rotation Angle (degrees)	Counts	Rotation Angle (degrees)	Counts	Rotation Angle (degrees)
638	0.26	634	0.28	365	34.36
638	0.26	629	0.31	364	35.44
638	0.26	621	0.35	363	36.12
638	0.26	603	0.49	361	37.42
639	0.26	581	0.72	359	38.45
638	0.26	562	1.02	358	38.88
638	0.26	540	1.51	357	39.58
638	0.26	523	2.03	356	40.43
638	0.26	500	3.08	356	40.93
638	0.26	469	5.40	355	41.52
638	0.26	445	8.32	354	42.36
638	0.26	432	10.34	353	43.02
638	0.26	424	12.08	352	43.66
638	0.26	414	14.40	351	44.65
638	0.26	407	16.37	349	45.96
638	0.26	401	18.04	349	46.26
637	0.26	398	19.02	348	47.06
638	0.26	394	20.38	346	48.30
637	0.26	390	21.97	345	49.19
638	0.26	387	23.17	345	49.72
637	0.26	385	24.26	344	49.92
638	0.26	382	25.29	344	50.67
638	0.26	381	26.08	343	51.60
638	0.26	378	27.39	342	51.94
638	0.26	376	28.62	341	52.93
637	0.26	374	29.63	341	53.18
639	0.26	372	30.57	341	53.34
638	0.26	369	31.96	341	53.59
638	0.26	368	32.64	340	54.42
637	0.26	367	33.45	339	54.97

Table 26 continued

Counts	Rotation Angle (degrees)	Counts	Rotation Angle (degrees)	Counts	Rotation Angle (degrees)
339	54.94	332	62.53	325	71.01
339	55.20	331	62.46	325	70.66
338	56.05	331	63.38	324	70.83
338	55.89	331	63.76	325	71.25
338	56.08	331	63.65	324	71.93
337	56.79	330	63.99	324	71.34
337	56.99	330	64.55	324	71.59
337	56.85	330	64.87	324	71.76
337	57.09	327	67.88	324	72.32
336	57.81	327	68.32	323	72.19
336	58.15	327	68.61	324	72.10
336	57.77	327	68.01	324	72.78
336	58.63	326	68.08	323	72.10
335	59.04	327	68.77	323	72.19
335	59.12	326	69.14	323	72.87
335	59.36	326	68.65	323	73.57
334	60.04	326	68.94	323	72.82
334	60.39	326	69.22	323	73.52
334	60.32	326	69.51	323	73.78
334	60.42	326	69.06	323	73.31
333	61.25	325	69.35	323	73.69
333	61.36	326	70.08	323	73.61
333	61.43	325	70.21	323	73.18
333	61.14	325	70.12	324	72.91
332	62.01	325	70.17	324	73.31
332	62.60	325	70.59		

The total estimated rotation angle for the robot finger's output is 73.3 degrees. For comparison, the input rotation angle from the proposed method is 73.0 degrees. The difference between the curves in Figure 71 is mainly due to the mechanical issues of the robotic finger. This is further discussed in Chapter 9. This study conclusively demonstrates the capabilities of the proposed PW Doppler sensing and processing method.
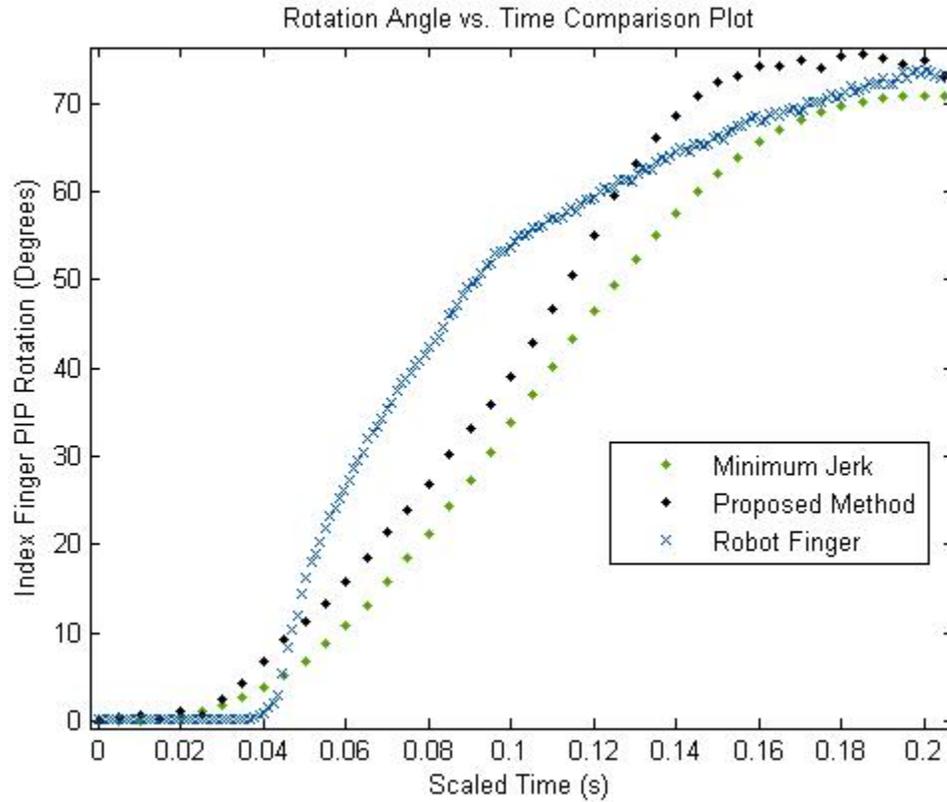
Figure 71: **Comparison of the rotation angles vs. time for the three robot finger trials, the proposed method's and the minimum jerk's angular information. Here, the time axis is scaled such that the curves all start and stop at the same time.**

Chapter 9

Discussion

In this thesis, a feasibility study was presented in order to conclusively determine if the real-time Doppler audio from an ultrasound scanner can accurately detect tendon motion for eventual assistive exoskeleton uses. By first moving a tendon mimicking string 9.1 cm ± 0.1 cm under the LogicScan™ scanner's transducer, the scanner's software displayed the velocity spectrogram, and the resulting Doppler-shifted frequencies was output and collected as an output signal in real-time. The scanner's onboard software estimated the mean string displacement to be 8.59 cm with a standard deviation of 0.50. These results present poor accuracy and high variability.

In this experiment it was also shown that the Doppler shifted frequencies of the moving string are also in the audible range and can be transformed into audio signals. Using the audible signals from a soundcard is an inexpensive way to obtain the Doppler frequency information in real-time since most commercial scanners do not allow for data access. This audio signal was obtained in real-time and processed in Matlab™. Using the proposed audio-based Fourier analysis, the estimated mean string displacement was 9.14 cm with a standard deviation of 0.28 cm. These results were quite accurate and within an acceptable range of the actual string displacements.

A second experiment was performed to extend this idea by using a biological tendon in order to further determine the feasibility. By moving a beef flexor tendon string 3.0 cm ± 0.1 cm under the LogicScan™ scanner's transducer, the scanner's software displayed the velocity spectrogram, and the resulting Doppler-shifted frequencies were output and collected as an output signal in real-time. The scanner's onboard software estimated the mean tendon displacement to be 2.91 cm with a standard deviation of 0.07 cm.

The second experiment shows that the Doppler shifted frequencies of the moving beef tendon were also in the audible range and can be transformed into audio signals. This audio signal was obtained in real-time and processed in Matlab™. Using the proposed audio-based Fourier analysis, the estimated mean tendon displacement was

found to be 2.98 cm with a standard deviation of 0.09 cm. These results were quite accurate, better than the ultrasonic scanner's measurements and within an acceptable range of the actual tendon displacements.

The variability in both the string and beef tendon experiments from the LogicScan's results were mainly due from the applied high-pass Wall Filter which eliminates 7% of the lowest frequencies in the range. This would ultimately affect the outcome of the displacement estimation because there would be excessive weighting to the higher amplitude frequencies (or velocities). This was because the mean frequency (or velocity) at a given time was calculated using Equation (16). This equation weights the velocities according to the amplitude of their power spectral density. Using an inappropriate frequency (or velocity) cut-off would result in an inaccurate mean velocity curve, velocity-time integral and thus, displacement. Furthermore, the ultrasound's software was factory calibrated to be used for many different applications, such as imaging deep and surface anatomical structures, fetal imaging and blood flow. Therefore, the types of filters and approximations implemented have to be general enough for these various uses. However, detailed error sources related to this are unknown because the software's approximations and processing methods are proprietary materials for the manufacturer. Furthermore, a fundamental error occurs with the Doppler correction angle. Recall that an ultrasound gel pad with a stand off wedge was used in the experiments in order to minimize the correction angle. This was because the tendon flow was not parallel to the ultrasound wavefront. The correction angle was visually determined on the B-Scan image as 59º. This error appears in both processing techniques whenever the Doppler equation in Equation (13) was employed. Therefore, because the tendon flow was not parallel to the transducer, the correction angle induces an approximate 6% error maximum, in all trials. This 6% error allows the ultrasound's calculated displacements to be within the limits of an acceptable range. Furthermore, there exist methods other than Fourier transforms in order to estimate the frequency content of the signal. This is discussed further in the Future Works section (Chapter 10).

The successful feasibility study presented in the first two experiments show that Pulsed Wave (PW) Doppler can accurately measure the small velocity and displacements of a moving human "tendon-like" object (string and beef tendon). Furthermore, real-time

Doppler data access from an ultrasound machine was made possible by using the audio output. The processed audio has also shown to be more accurate than the ultrasound scanner's software-based results in both experiments.

Now that the ability of the proposed sensing and processing method has been demonstrated, the feasibility study was extended further to include displacement monitoring of biological human tendons to access hand functions and to control a robotic device. After first locating the tendon, 3 trials containing the tendon excursion data were collected by the LogicScan™ ultrasound scanner for the total PIP joint rotations of 35°, 70°, 80°, 100°, and 110°. The onboard software then performed the VTI to obtain the estimated displacements. The mean estimated total displacements and standard deviation using LogicScan's onboard software for these trials is summarized in Table 27.

Table 27: Mean tendon displacements and standard deviation using LogicScan's onboard software for the 3 trials.

Rotation Angle	35° PIP Rotation	70° PIP Rotation	80° PIP Rotation	100° PIP Rotation	110° PIP Rotation
Mean Total Displacement (mm)	3.27	6.90	8.07	8.03	11.90
Standard Deviation (mm)	0.06	0.35	0.40	0.21	0.35

For the previous 3 trials of joint rotation data, the Doppler-shifted audio signal was simultaneously obtained in real-time using a data acquisition script in Matlab™. Using the previously described custom Matlab™ script, the Doppler shifted signal, the velocity spectrogram, the mean velocity points, fitted mean velocity curve and displacements (via integration) were estimated. The mean estimated total displacement and standard deviation using the proposed processing method for these trials are summarized in Table 28. For comparison, the invasive mean total tendon excursion measurements of the FDS tendon in active excursion was estimated in the literature as 14 mm in cadavers and 10 mm during surgery, each having the PIP joint rotate 90° [112].

However, it is important to note that the tendon excursion experienced during rotation is highly individualistic. Overall, there was less variability in the tendon excursions that were processed with the proposed method (Table 28) in comparison to the LogicScan's displayed results (Table 27).

Table 28: Mean tendon displacements and standard deviation using the proposed processing method for the 3 trials.

Rotation Angle	35° PIP Rotation	70° PIP Rotation	80° PIP Rotation	100° PIP Rotation	110° PIP Rotation
Mean Total Displacement (mm)	3.57	7.33	8.67	10.3	11.67
Standard Deviation (mm)	0.15	0.25	0.23	0.1	0.15

In order to further validate the tendon excursions that were estimated using the proposed Matlab^{TM} script (or the LogicScan^{TM} software), the estimated tendon displacements should be compared to the actual displacements experienced during PIP rotation. This was a complicated task because the actual tendon displacements can only be measured non-invasively in these experiments. An accepted model in the literature, called the Brand and Hollister tendon-pulley model, correlated the rotation angle of the joint with the tendon excursion experienced [107]. Using this tendon pulley model described by Equation (23), the total tendon excursions were estimated by using the final rotation angles measured with the goniometer and an approximated moment arm. The simplest approximation of the moment arm of the PIP joint was measured with a digital calliper and estimated as 6.04 mm ± 0.01 mm. Using this moment arm, Equation (23) and the rotation angles measured with the goniometer (35°, 70°, 80°, 100°, and 110°), the tendon excursions were estimated and compared to the Matlab^{TM} and LogicScan^{TM} estimations. As shown in Table 29, the total tendon displacements estimated by this method are most comparable to those processed by the script in Matlab^{TM}.

Table 29: Tendon displacement estimation comparison

Total Tendon Excursion (mm) for:	35° PIP Rotation	70° PIP Rotation	80° PIP Rotation	100° PIP Rotation	110° PIP Rotation
LOGICSCAN	3.27	6.90	8.07	8.03	11.90
MATLAB	3.57	7.33	8.67	10.30	11.67
BRAND AND HOLLISTER:	3.69	7.38	8.43	10.54	11.60

For comparison, the moment arm was also approximated using the total tendon excursions estimated by the proposed processing script in Matlab™. For each of the 3 trials, the total tendon excursion estimated by the Matlab™ script was plotted against its corresponding final rotation angle (measured with the goniometer), a linear interpolation was fit, and the slope was determined. Using Equation (23) and the slope on each plot, the average moment arm was estimated as 6.03 mm with a standard deviation of 0.058 mm. This was comparable to the moment arm that is estimated by the digital calliper.

Essentially, Equation (23) was also used in the literature to compare their estimated tendon excursions to those calculated by this equation [90]. Generally, this technique has limitations because it assumes the tendon was without interconnections, free to move, and constant throughout the rotation of the finger [107]. In actuality, the tendons have interconnections which will alter the actual displacement of a tendon during rotation. Furthermore, there is much debate on the role of tendon excursion with full index finger flexion. This is because there are discrepancies in the reported literature of the contributions of flexors and intrinsic muscles to MCP flexion, for example [113,123-

124]. To temporarily avoid this problem, the protocol presented in this thesis does not consider MCP flexion; the active PIP and passive DIP flexion was only considered. Nevertheless, the tendon excursion results presented in this thesis are consistent with the literature for full PIP and DIP flexion [90,112].

It is important to note that the *total* displacements determined by the proposed method were compared to the ultrasound machine's *total* estimated displacements and the model's *total* displacements. This was because continuous displacement vs. time results were not available for the ultrasound machine (the total displacements were just reported). Also, an active external displacement monitoring system was not available for the experiments. Therefore, only the total displacements estimated by each method were compared. However, the proposed script does allow for continual displacement vs. time measurements (as shown in Table 20). Continual displacement vs. time measurements is an important property for real-time control of an exoskeleton.

In order to further validate the tendon excursions estimated by the proposed processing Matlab^{TM} script, the tendon excursions were compared to another accepted model called the Minimum Jerk approximation. As described by Bundhoo et.al. [122], jerk is an accepted quantity of evaluating motor smoothness of the human limbs (Equation (25)).

For the sake of simplicity, the tendon excursions as a function of time processed by the proposed Matlab^{TM} script for the third 70 ° trial were used for comparison to the Minimum Jerk model. The tendon excursions as a function of time were translated into rotation angles as a function of time using the Brand and Hollister approximation and the average moment arm determined in Section 8.1.4 (6.03 mm) for the Matlab^{TM} processed excursions. The final rotation angle was estimated as 73.0 degrees using this method. This value was comparable to the total rotation angle measured by the goniometer (70°±2°). As previously discussed, the main error sources using the proposed processing method in Matlab^{TM} included noise from the soundcard, the Doppler angle uncertainty and the choice of a cut-off frequency threshold and power spectral density threshold.

Using Equation (26), the Minimum Jerk profile and the proposed Matlab^{TM} method were compared for accuracy. The Minimum Jerk's angular profile was shown in

Table 22 (using the same time steps as in the Matlab^TM script) and displayed in Figure 64 along with the proposed method's angular profile for comparison. Although their angular profiles were comparable, there exists the ability to improve the experimental curve by performing a different data acquisition method with increased accuracy. It would be more accurate to use an optical motion tracking system such as Visualeyez^TM to measure rotational data as a function of time with simultaneous tendon excursion estimations using the proposed technique. This would estimate a moment arm with increased accuracy. For the proposed method in Matlab^TM, the initial and final rotation data points in Figure 64 were not as smooth as the Minimum Jerk approximation. This was mainly due to the fact that the moment arm was assumed to be constant throughout rotation (Brand and Hollister model). Therefore, the rotation angles that were calculated using Equation (23) will have inaccuracies in the regions where the moment arm was not constant. Furthermore, there exist other rotational profiles which should be used in order to correlate tendon excursion to angular rotation (other than the one used in Equation (23)). This is because the moment arms of the joints are actually not constant throughout rotation [113]. Using an improved correlation between rotation angles and tendon excursion will allow for increased accuracy. These improvements are further described in the Future Works section (Chapter 10). Nevertheless, the curves in Figure 64 using the Matlab script and the Minimum Jerk approximation were comparable. The final rotation angle estimated by the Minimum Jerk approximation was 70.8 degrees. This was compared to the goniometer estimation of 70.0 degrees and the Matlab^TM method estimation of 73.0 degrees. Overall, the results determined by the proposed processing script in Matlab^TM were shown to represent an accurate depiction of a tendon excursion event.

In order to demonstrate robotic finger control, the input signal data should be from one set of tendon excursion vs. time data that was converted to rotation angles vs. time using the estimated moment arm and Equation (23). This was because the eventual goal of this work is to automate the entire process and have real-time acquisition, processing and robotic control. Also, the robot finger's software requires the input data to initially be in terms of rotation angles. For the sake of simplicity, the rotation angles that

were estimated from the processed user intended tendon motion signal in Table 21 were used as an input to control the robotic finger.

Since the robotic finger's software interprets angular position in terms of A/D counts, a calibration method was devised to correlate A/D counts to rotational position. This calibration allows for the input of data from the proposed sensing method, as well as the robotic finger's output data to be converted back to angular position for comparison. The artificial finger's PIP joint was moved to 0°, 10°, 20°, 30°, 40°, 50°, 60°, and 70° in separate trials and the corresponding A/D counts were recorded and shown in Table 24. By plotting the robot's PIP rotation angles as a function of A/D counts and fitting an exponential curve in Matlab ^{TM}, the calibration was achieved and the relationship between rotation angle and A/D counts was known (Figure 68). This will allow for the robot's output of A/D counts to be converted into rotation angles for comparison. The fitted exponential equation that correlates rotational position to A/D counts was shown in Equation (27).

Similarly, the A/D counts as a function of rotation angle must be known in order to input the proposed method's angular information to the robot's software. The robot finger's data from Table 24 was plotted and a natural logarithmic curve was fit (Figure 69). The fitted logarithmic equation that correlates A/D counts to rotational position was shown in Equation (28). The fitted curves (Equations (27) and (28)) were inverses of each other, as expected.

The rotation angles that were estimated from the processed user intended tendon motion signal in Table 21 were used as an input to control the robotic finger. These angles from the third 70° trial were converted to A/D counts using Equation (28), and were shown in Table 25 and Figure 70.

The angles from the third 70° trial that were converted to A/D counts in the previous section were entered into a lookup table on the robot's LabVIEW^{TM} software. The robotic finger's software interprets this data and rotated to the specified locations with SMA actuation. Once the robot's PIP flexion was completed, a table of A/D counts over the joint's range of motion was produced from LabVIEW^{TM}. Using Equation (27), these counts were converted back to rotation angle for comparison. The resulting A/D counts and rotation angles for these trials were displayed in Table 26. Because of the

accumulation of error in calibrating rotation angle to counts, the total rotation angle of the robot finger's output data was estimated as 73.3 degrees. The estimated total angular rotation expected was 73.0 degrees from the input data. The main reason for the variability in each data set in comparison to the actual rotation was the accumulation of error from the calibration technique. Here, rotational position and A/D counts was measured inefficiently and inaccurately. It would be more accurate to use Visualeyez^{TM} to measure rotational data as a function of time, with simultaneous measurements of A/D counts using the robot's software. This calibration technique was used in the literature more effectively [122]. Furthermore, the operating voltage of the robotic finger was increased until it would reach full rotation, and the string was tightened in order to improve the rotational rate. In addition, because the robot finger and the human finger all rotate at different rates, the slopes from all of the rotation angle vs. time curves will be different. A scaling factor was applied to the time data on the x-axis for better comparison (Figure 71). The main difference between the curves in Figure 71 is that the robot finger took longer to begin rotating and had a different angular acceleration rate in the middle and end region in comparison the Minimum Jerk or proposed method's data. This was mainly due to the mechanical issues of the robot finger. For example, due to the quality of the SMA actuators, the finger takes longer to begin rotating and will have a different rotation rate. Also, the artificial tendon string used on the robot finger has tension problems at the higher rotation angles. It is also important to note that the robotic finger has been broken and repaired several times. Previous performance testing of the robot before the accidents demonstrated increased accuracy because it followed the Minimum Jerk model more closely [122]. Alternatively, a linear encoder can be used on the robot finger which will allow for the direct input of the estimated tendon excursions vs. time determined by the proposed method. This will increase the accuracy by eliminating the need to translate the estimated excursions into rotation angles using an accepted model. Overall, the curves in Figure 71 were comparable and demonstrate the successful use of control from the new sensing method.

Chapter 10

Conclusion and Future Works

The human hand is perhaps the most dexterous device that is quite daunting to mechanically replicate. Rarely can mechanical parts go un-serviced for many years like the human hand usually does. Hands can heal themselves, work in many weather conditions and touch things with delicate care or overpower rugged rocks. Consequently, because hands get injured and diseased, engineers design wearable robots to supplement the patient's disability. Even though the most sophisticated of robotic hands do not replace the exquisite natural hand mechanism, several wearable devices throughout history were created. Current wearable robotic technologies that are designed as an assistive device have limited usability, thus inspiring a new approach to sensing and control in this thesis.

The primary goal of the research presented in this thesis was to introduce a novel sensing strategy using Pulsed-Wave (PW) Doppler ultrasound for detecting user intended hand grasping. This new bio-sensing strategy is developed here specifically for the application of hand exoskeleton motion for disabled patients with some residual hand control. The successful feasibility study presented in this thesis shows that PW Doppler can accurately measure the small velocity and displacements of a moving string, beef tendon and human biological tendon. Furthermore, the signal from a moving human tendon is shown to control a robotic finger. In addition, real-time Doppler data access from an ultrasound machine is possible by using the audio output. This presents an inexpensive way to obtain Doppler data access which otherwise wouldn't be possible. Overall, the processed audio has also been shown to be more accurate than the ultrasound scanner's software-based results in all cases.

In particular, the following objectives have been successfully addressed in this thesis:

1) To determine the difficulties in the current strategies to sense user intention for bio-robotic control, based on a thorough literature review.

2) To identify the anatomical and functional capabilities of a healthy hand in order to determine an optimal sensing strategy to restore some of the motor abilities in disabled patients.

3) To develop an original sensing strategy using Pulsed-Wave (PW) Doppler ultrasound to detect the velocity and displacement of a moving tendon in the wrist for the eventual use on an assistive exoskeleton.

4) To develop a signal processing technique to test the feasibility of this new bio-sensing method.

5) To perform three experiments in order to test the accuracy of the new signal processing technique. These experiments include:

(i) accurately measuring the small velocity and displacements of a moving string,

(ii) accurately measuring the small velocity and displacements of a moving beef tendon, and

(iii) accurately measuring the small velocity and displacements of a human biological tendon and demonstrating the control of a robotic finger test-bed using the acquired measurements.

The primary areas of emerging science explored here is the successful detection of user intention and the control of a bio-robotic device. Although this initial proof of principle demonstrates significant feasibility, there is room for an improved study. Primarily, the human and robotic PIP joint rotations in the final experiment should be monitored by an external motion tracking system. The processing method proposed in this thesis can also be improved by investigating other digital signal processing methods. This includes an improved method of noise removal as well as improving the frequency resolution by using other techniques like Wavelet Transforms [125]. The overall accuracy of the proposed sensing and processing technique should also be estimated. This is where an open-ended research based ultrasound machine like UltraSonix 500 RP [TM] (Ultrasonix Medical Corporation) would be useful [126]. Using such a system will allow for raw data access at any stage, and the algorithm or other system protocols can be tested for accuracy.

After the initial feasibility of this sensing strategy is improved, a portable/wearable prototype design will be implemented. This next stage includes an exoskeleton mechanism for the finger, an improved data acquisition board, piezoelectric devices, and improved software to allow for real-time acquisition and control.

Overall, the proven ability to detect tendon motion with PW Doppler ultrasound has significant academic contributions to current research in bio-robotic control and other medical sciences. For example, hand surgeons have interest in the post-operative conditions of tendons in order to quantify excursions. Most clinicians and researchers presently use inaccurate methods such as goniometers for non-invasive measurements. The proposed algorithm presented in this thesis has shown to accurately quantify such measurements and can replace existing methods. Also, many areas of research require raw Doppler data from affordable commercial ultrasound machines. The proposed processing method that was presented in this thesis will allow access to the demodulated Doppler shift signals through the audio output of a soundcard. Researchers can then test their processing algorithms or filter designs on these signals and compare them to the output of the scanner. Most importantly, the new sensing and processing technique that was presented in this thesis has demonstrated feasibility for bio-robotic control. This new sensing method using Pulsed Wave Doppler to detect tendon motion has the ability to replace existing techniques using EMG sensing. This is because there are several different tendon sites in which Doppler shift data can be acquired from. Being able to obtain more information from the human user will directly correlate to the sophistication and the degrees-of freedom of the robotic device. Overall, the research presented here has contributed to current research in several areas and has the ability to expand in technique and applications for future works involving exoskeleton control.

Bibliography

[1] Thurston, AJ (2007). "Paré and prosthetics: the early history of artificial limbs". ANZ Journal of Surgery. 77(12), pp. 1114-1119.

[2] Touch Bionics. "The i-Limb Hand". Retrieved July 3rd, 2009 at Internet URL: http://www.touchbionics.com/

[3] Lin, LR and Huang HP (1998). "NTU Hand: A New Design of Dexterous Hands". J. Mech. Des. 120, pp. 282

[4] Shadow Robot Company (2003), "Design of a dextrous hand for advanced clawar applications". Climbing and Walking Robots and the Supporting Technologies for Mobile Machines: CLAWAR 200, pp. 691-698.

[5] BBC News (2007). "Cairo toe earliest fake body bit." Retrieved July 3rd, 2009 at Internet URL: http://news.bbc.co.uk/2/hi/health/6918687.stm

[6] Science Museum. "Roman artificial leg, c. 300 BC". Retrieved July 3rd, 2009 at Internet URL: http://www.sciencemuseum.org.uk/objects/classical_and_medieval_medicine/A646752.aspx

[7] University of Iowa Medical Museum (2006). "History of Prostheses". Retrieved July 3rd, 2009 at Internet URL: http://www.uihealthcare.com/depts/medmuseum/wallexhibits/body/histofpros/histofpros.html

[8] Shadow Robot Company. "Hand Pictures". Retrieved on July 3rd, 2009 at Internet URL: http://www.shadowrobot.com/hand/pictures.shtml

[9] Smith, EE (1934). "Triplanetary". Amazing Stories.

[10] Dellon, Brian et al.(2007). "Prosthetics, exoskeletons, and rehabilitation". IEEE robotics & automation magazine. 14, pp. 30-34.

[11] CYBERDYNE Inc. Retrieved July 3rd, 2009 at Internet URL: http://www.cyberdyne.jp/English/index.html

[12] Wege, A and Hommel, G (2005), "Development and control of a hand exoskeleton for rehabilitation of hand injuries". 2005 IEEE/RSJ International Conference on Intelligent Robots and Systems. pp. 3046-3051.

[13] Ruiz, AF, Forner-Cordero, A, Rocon, E and Pons, JL (2006)."Exoskeletons for Rehabilitation and Motor Control". Biomedical Robotics and Biomechatronics, 2006. The First IEEE/RAS-EMBS International Conference. pp. 601 – 606.

[14] Worsnopp, TT, Peshkin, MA,Colgate, JE and Kamper, DG (2007). "An Actuated Finger Exoskeleton for Hand Rehabilitation Following Stroke". Rehabilitation Robotics IEEE 10th International Conference. pp. 896-901

[15] Kiguchi, K, Imada, Y and Liyanage, M (2007). **"EMG-Based Neuro-Fuzzy Control of a 4DOF Upper-Limb Power-Assist Exoskeleton".** Engineering in Medicine and Biology Society. 29th Annual International Conference of the IEEE. pp. 3040 – 3043

[16]Fleischer C, Wege A, Kondak K, Hommel G (2006)."Application of EMG signals for controlling exoskeleton robots". Biomed Tech (Berl). 51(5-6), pp. 314-319.

[17] Mulas, M, Folgheraiter, M, and Gini, G (2005). "An EMG-controlled exoskeleton for hand rehabilitation". Rehabilitation Robotics, 9th International Conference, pp. 371-374.

[18] Lucas L,. DiCicco M, and Matsuoka Y (2004). "An EMG-Controlled Hand Exoskeleton for Natural Pinching". Journal of Robotics and Mechatronics, 16(5), pp. 482 - 488.

[19] "Hand Exoskeleton". Retrieved on July 3rd, 2009 from Internet URL: http://pdv.cs.tu-berlin.de/HandExoskeleton/HandExoIntro.html

[20] Feehan LM, Oxland T, Tang C (2007). "Early controlled passive motion improves early fracture alignment and structural properties in a closed extra-articular metacarpal fracture in a rabbit model". J Hand Surg. 32A(2), pp. 200-208.

[21] Feehan LM, and Basset K (2004). "Is there evidence for early motion following an extra-articular hand fracture?" J Hand Ther. 17(2), pp. 300-308.

[22] Lloyd-Jones D, Adams R, Carnethon M, De Simone G, et. al. (2009)."Heart disease and stroke statistics--2009 update: a report from the American Heart Association Statistics Committee and Stroke Statistics Subcommittee". Circulation. 119(3), pp. 21-181.

[23] Seo et al. (2009) "Delays in Grip Initiation and Termination in Persons With Stroke: Effects of Arm Support and Active Muscle Stretch Exercise". Journal of Neurophysiology. 101 (6), pp. 3108.

[24] Feehan LM, and Sheps S (2006). "Incidence and demographics of hand fractures in British Columbia , Canada : A population based study". J Hand Surg. 31A(7), pp. 1068-1074.

[25] Kinetic Muscles Inc. "The Hand Mentor". Retrieved on July 3rd, 2009 from Internet URL: http://www.kineticmuscles.com/handmentor.html

[26] Ford. "FORD SYNC™ – TODAY'S DRIVERS DEMAND STAYING CONNECTED". Retrieved on July 3rd, 2009 from Internet URL: http://media.ford.com/article_display.cfm?article_id=25169

[27] Dalton, A and Ellis, C (2003). "Sensing User Intention and Context for Energy Management". Proceedings of the 9th conference on Hot Topics in Operating Systems. 9, pp. 26-30.

[28] Freund R (2000). "Virtual Reality for intelligent and interactive operating-, training- and visualization systems". Sensor fusion and decentralized control in robotic systems III. Conference N°3. 4196, pp. 267-278.

[29] Stergiopoulos P, Fuchs P and Laurgeau, C (2003). "Design of a 2-Finger Hand Exoskeleton for VR Grasping Simulation". EuroHaptics 2003.

[30] Nakanishi H, Koizumi S, Ishida T and Ito H (2004) . "Transcendent Communication: Location-Based Guidance for Large-Scale Public Spaces". Proceedings of the SIGCHI conference on Human factors in computing systems. pp. 655 – 662.

[31] Topolsky J (2007). "Sarcos' military exoskeleton becomes a frightening reality". Retrieved July 3rd, 2009 at Internet URL: http://www.engadget.com/2007/11/25/sarcos-military-exoskeleton-becomes-a-frightening-reality/

[32] Pons JL, Ceres R , Rocon E, et. al. (2005). "Virtual reality training and EMG control of the MANUS hand prosthesis". Robotica, 23(3), pp. 311-317.

[33] Keesey, J (2005). "How Electric Fish Became Sources of Acetylcholine Receptor". Journal of the History of the Neurosciences. 14(2) , pp. 149-164.

[34] Zecca M and Micera S et al. (2002). "Control of Multifunctional Prosthetic Hands by Processing the Electromyographic Signal". Crit. Reviews in Biomedical Eng. 30(4-6), pp. 459-485.

[35] Masuda K, Masuda T, Sadoyama T, Inaki M and Katsuta S (1999). "Changes in surface EMG parameters during static and dynamic fatiguing contractions". J Electromyogr Kinesiol. 9(1), pp. 39-46.

[36] Chu JU, Moon I, et al. (2005). "Control of multifunctional myoelectric hand using real time EMG Pattern Recognition". Intelligent Robots and Systems, 2005. pp. 3511 – 3516.

[37] Otto Bock Inc. "The Sensor Hand". Retrieved on July 3rd, 2009 at Internet URL: http://www.ottobock.com/cps/rde/xchg/ob_com_en/hs.xsl/3652.html

[38] University Hospital Heidelberg (2008). "'Fluidhand': Each finger can be moved separately." Retrieved on July 3rd, 2009 at Internet URL: http://www.physorg.com/news128082539.html

[39] Kyberd P and Chappell P (1994). "The Southhampton Hand: An intelligent myoelectric prosthesis." J of Rehabilitation Research and Development. 31(4), pp. 326-334.

[40] Zheng YP, Chan MM, Shi J, Chen X, Huang QH (2006). "Sonomyography: monitoring morphological changes of forearm muscles in actions with the feasibility for the control of powered prosthesis". Med Eng Phys. 28(5), pp. 405-15.

[41] Guo JY, Zheng YP, Huang QH, and Chen X (2008). "Dynamic monitoring of forearm muscles using one-dimensional sonomyography system". J Rehabil Res Dev. 45(1), pp. 187-196.

[42] Takahashi K, NakaukeT, and Hashimoto M (2007). "Hands-Free Manipulation Using Simple Bio-Potential Interface System". Journal of System Design and Dynamics. 1(4), pp.691-702.

[43] Scientific American: News In Brief (2000). "Monkey See, Robot Do". Retrieved on July 3rd, 2009 at Internet URL: http://www.nicolelislab.net/Papers/Robot.pdf

[44] Pfurtscheller et al (2000). "Brain oscillations control hand orthosis in a tetraplegic". Neuroscience letters. 292, pp. 211-214.

[45] Mahmoudi, B and Erfanian, A (2002). "Single-channel EEG-based prosthetic hand grasp control for amputee subjects". Engineering in Medicine and Biology, 2002. 24th Annual Conference and the Annual Fall Meeting of the Biomedical Engineering Society EMBS/BMES Conference. Proceedings of the Second Joint. 3, pp. 2406- 2407.

[46] Guger, Schlogla, Walterspacher and Pfurtscheller (1999). "Design of an EEG-based brain-computer interface (BCI) from standard components running in real-time under Windows". Biomedizinische Technik. 44, (1-2), pp. 12-16.

[47] Freedman DH (2008). "Reality Bites". Retrieved on July 3rd, 2009 at Internet URL: http://www.inc.com/magazine/20081201/reality-bites.html.

[48] University of Reading (2008). "Robot with a Biological Brain: new research provides insights into how the brain works". Retrieved on July 3rd, 2009 at Internet URL:
http://www.reading.ac.uk/sse/about/News/sse-newsarticle-2008-08-18b.asp

[49] Cohen D and Cuffin BN (1983). "Demonstration of useful differences between the magnetoencephalogram and electroencephalogram". Electroencephalogr Clin Neurophysiol. 56, pp. 38-51.

[50] Waldert S, Preissl H, Demandt E, Braun C, Birbaumer N, Aertsen A, and Mehring C (2008) . "Hand movement direction decoded from MEG and EEG". J Neuroscience. 28(4), pp. 1000-1008.

[51] Kenney et. al. "Dimensional change in muscle as a control signal for powered upper limb prostheses: a pilot study". Medical Engineering & Physics. 21 (8), pp. 589 – 597.

[52] Canderle J, Kenney LPJ, Bowen A, Howard D, Chatterton H (2004). "A dual-task approach to the evaluation of the myokinemetric signal as an alternative to EMG".
Engineering in Medicine and Biology Society, 2004. 2 (6), pp. 4548 – 4551.

[53] Coburn JW, Housh TJ, Cramer JT, Weir JP, Miller JM, Beck TW, Malek MH, and Johnson GO (2005). "Mechanomyographic and electromyographic responses of the vastus medialis muscle during isometric and concentric muscle actions". J Strength Cond Res. 19(2), pp. 412–420.

[54] Madeleine P, Jørgensen LV, Søgaard K, Arendt-Nielsen L, Sjøgaard G (2002). "Development of muscle fatigue as assessed by electromyography and mechanomyography during continuous and intermittent low-force contractions: Effects of the feedback mode". Eur J Appl Physiol. 87(1), pp. 28–37.

[55] Weir JP, Ayers KM, Lacefield JF and Walsh KL (2000). "Mechanomyographic and electromyographic responses during fatigue in humans: Influence of muscle length". Eur J Appl physiology. 81(4), pp. 352-359.

[56] Silva J, Heim W, and Chau T (2005). "A self-contained, mechanomyography-driven externally powered prosthesis". Arch Phys Med Rehabil. 86(10), pp. 2066–2070.

[57] Orizio C (1993). "Muscle sound: Bases for the introduction of a mechanomyographic signal in muscle studies". Crit Rev Biomed Eng. 21(3), pp. 201–243.

[58] Jaskólska A, Brzenczek W, Kisiel-Sajewicz K, Kawczyski A, Marusiak J and Jaskólski A (2004). "The effect of skinfold on frequency of human muscle mechanomyogram". J Electromyogr Kinesiol. 14(2), pp. 217–225.

[59] Silva J and Chau T (2003). "Coupled microphone-accelerometer sensor pair for dynamic noise reduction in MMG signal recording". Electron Lett. 39(21), pp. 1496–1498.

[60] Barea R, Boquete L, Mazo M, and Lopez E (2002). "System for Assisted Mobility Using Eye Movements Based on Electrooculography". IEEE Transaction on Neual Systems and Rehabilitation Engineering. 10(4), pp. 209-218.

[61] Gu J, Meng M, Cook A and Faulkner G (2005). "Simulation study of artificial ocular movement with intelligent control". Control Engineering.13(4), pp. 509-518.

[62] Williams M and Kirsch R (2005). "The Feasibility of EEG as a Command Interface for a high Tetraplegia Neural Prosthesis". The 10th Annual Conference of the International Functional Electrical Stimulation Society.

[63] Nathan RH (1989). "An FNS Based System for Generating Upper Limb Function in the C4 Quadriplegic". Med. & Bio. Eng. & Comput. 27, pp. 549-556.

[64] Mazo M, Rodríguez F, Lázaro J, et. al. (1995). "Wheelchair for physically disabled people with voice, ultrasonic and infrared sensor control". Autonomous Robots, 2, pp. 203-224.

[65] Clark JA and Roemer RB (1977). "Voice controlled wheelchair". Arch Phys Med Rehabil. 58(4), pp. 169-175.

[66] Crabfu MotionWorks. "Swashbot". Retrieved on July 3rd, 2009 at Internet URL: http://www.crabfu.com/swashbot/

[67] Innovation First Inc. "HEXBUG". Retrieved on July 3rd, 2009 at Internet URL: http://www.hexbug.com/

[68] Chitwood WR and Nifong LW (2000). "Minimally invasive videoscopic mitral valve surgery: the current role of surgical robotics". J Card Surg. 15(1), pp. 61-75.

[69] Abboudi R, Glass C, Newby A , Flint J and Craelius W (1999). "A biomimetic controller for a multifinger prosthesis". Rehabilitation Engineering, IEEE Transactions 7(2), pp. 121 – 129.

[70] Curcie D, Flint J, Craelius W (2001). "Biomimetic finger control by filtering of distributed forelimb pressures". Neural Systems and Rehabilitation Engineering IEEE Transactions. 9(1), pp. 69 – 75.

[71] Andreasen D, Alien S and Backus D (2005. "Exoskeleton with EMG based active assistance for rehabilitation". Rehabilitation Robotics. pp. 333-336.

[72] Sarakoglou I, Tsagarakis N and Caldwell D (2004). "Occupational and physical therapy using a hand exoskeleton based exerciser". Intelligent Robots and Systems. 3, pp. 2973-2978.

[73] Heumer G, Amor H, Weber M and Jung B (2007) . "Grasp Recognition with Uncalibrated Data Gloves - A Comparison of Classification Methods".
Virtual Reality Conference. pp. 19-26.

[74] Shields BL, Main JA, Peterson SW and Strauss AM (1997). "An anthropomorphic hand exoskeleton to prevent astronaut hand fatigue during extravehicular activities". IEEE Trans Syst Man Cybern A Syst Hum. 27(5), pp. 668-673.

[75] Kieler H, Cnattingius S, Haglund B, Palmgren J and Axelsson J. "Ultrasound and adverse effects". Ultrasound in Obstetrics and Gynecology. 20(1), pp. 102-103.

[76] Salvesen KA, Vatten LJ, Eik-Nes SH, Hugdahl K and Bakketeig LS (1993). "Routine ultrasonography in utero and subsequent handedness and neurological Development". 307, pp. 159–164.

[77] Kieler H, Axelsson O, Haglund B, Nilsson S and Salvesen KA (1998). "Routine ultrasound screening in pregnancy and the children's subsequent handedness". Early Hum Dev. 50, pp. 233–245.

[78] Kieler H, Cnattingius S, Haglund B, Palmgren J and Axelsson O (2001). "Sinistrality— a side-effect of prenatal sonography: a comparative study of young men". Epidemiology. 12, pp. 618–623.

[79] Kieler H, Cnattingius S, Palmgren J, Haglund B and Axelsson O (2002). "First trimester ultrasound scans and left-handedness". Epidemiology (Letter).13, pp. 370–372.

[80] Aoudi W, H. Liebgott H and A. Needles. "Estimation methods for flow imaging with high frequency ultrasound". Ultrasonics. 44(1), pp. 135-140.

[81] Crowe J and O'Donnell M (2001). "Quantitative blood speed imaging with intravascular ultrasound". Ultrasonics, Ferroelectrics and Frequency Control IEEE Transactions. 48(2), pp. 477-487.

[82] Revell J, Mirmehdi M and McNally D (2003). "Ultrasound Speckle Tracking For Strain Estimation". Retrieved on July 3rd, 2009 at Internet URL: www.cs.bris.ac.uk/Publications/Papers/2000106.pdf

[83] Xu X, Zhou O, Ameri H, Gottlieb E, Lai B, et. al. (2006). "High-Frequency Pulsed-Wave Ultrasound Doppler System for Biomedical Applications with PMN-PT Needle Transducer and 30 MHz Linear Array". Ultrasonics Symposium. pp. 2234 – 2237.

[84] Krupa A, Fichtinger G and Hager GD (2007). "Real-time tissue tracking with B-mode ultrasound using speckle and visual servoing". Med Image Comput. 10(Pt 2), pp. 1-8.

[85] "The Principle of Medical Ultrasound". Retrieved on July 3rd, 2009 at Internet URL:
http://www.mrcophth.com/commonultrasoundcases/principlesofultrasound.html#A%20in%20A-scan%20stand

[86] TELEMED. Retrieved on July 3rd, 2009 at Internet URL: http://www.telemed.lt/

[87] Lee J and Healy J (2005). "Normal Sonographic Anatomy of the Wrist and Hand". RadioGraphics. 25, pp. 1577-1590.

[88] InSight Imaging Inc. "Expectant Mothers Guide". Retrieved on July 3rd, 2009 from Internet URL:
http://www.expectantmothersguide.com/profiles/InsightImaging/index.htm

[89] Holland W, Buyruk H, Hoorn E and Stam H (1999). "Tendon displacement assessment by pulsed Doppler tissue imaging: validation with a reciprocating string test target". Ultrasound in Medicine & Biology. 25(8), pp. 1229-1239.

[90] Soeters J, Roebroeck M, Holland W, Hovius S and Stam H (2004). "Non-invasive measurement of tendon excursion with a colour doppler imaging system: a reliability study in healthy subjects". Scand J Plast Reconstr Surg Hand Surg. 380, pp. 356–360.

[91] Grassi W and Filippucci E (2001). "Sonographic imaging of tendons." Arthritis & Rheumatism. 43(5), pp. 969–976.

[92] Revell J, Mirmehdi M and McNally D (2003). "Motion trajectories for ultrasound displacement quantification". Proc. 7th Medical Image Understanding and Analysis. pp. 193–196.

[93] Soeters J and Roebroeck M (2004). "Reliability of tendon excursion measurements in patients using a color Doppler imaging system." J Hand Surgery. 29(4), pp. 581-586.

[94] Hough A, Moore A and Jones M (2000). "Measuring longitudinal nerve motion using ultrasonography". Manual Therapy. 5(3), pp. 173-180.

[95] Buyruk HM, Holland WPJ, et al. (1998). "Tendon excursion measurements with Color Doppler Imaging: a calibration study on embalmed human specimens". J Hand Surg. 23B, pp. 350-353.

[96] Buyruk HM, Stam HJ, et al. (1996). "Color Doppler ultrasound examination of hand tendon pathologies". J Hand Surg. 21B, pp. 469-473.

[97] Cigali BS, Buyruk HM, et al. (1996). "Measurement of tendon excursion velocity with color Doppler imaging: a preliminary study on flexor pollicis longus muscle". Eur J Radiol. 23, pp. 217-221.

[98] Maulik D and Zalud I (2005). "Doppler Ultrasound in Obstetrics and Gynecology". Springer. 2nd rev. and hardcover enlarged edition. Chapters 2-3.

[99] Schieber M (1995). "Muscular Production of lndividuated Finger Movements: The Roles of Extrinsic Finger Muscles". The Journal of Neuroscience. 75(l), pp. 284-297.

[100] Ugbolue U, Hsu WH, Goitz R and Li ZM (2005). "Tendon and nerve displacement at the wrist during finger movements". Clinical Biomechanics. 20(1), pp. 50-56.

[101] Revell J, Mirmehdi M and McNally D (2002). "Applied review of ultrasound image feature extraction methods". The 6th Medical Image Understanding and Analysis Conference. pp. 173–176. Retrieved on July 3rd, 2009 at Internet URL: http://www.compsci.bristol.ac.uk/Publications/pub_master.jsp?id=1000641

[102] Lee SS, Lewis GS and Piazza SJ (2008). "An algorithm for automated analysis of ultrasound images to measure tendon excursion in vivo". J Appl Biomech. 24(1), pp. 75-82.

[103] Bohs LN, Geiman BJ, Anderson ME, Gebhart SC and Trahey GE (2000). "Speckle tracking for multi-dimensional flow estimation". Ultrasonics. 38(1-8), pp. 369-375.

[104] Huang O, Zheng Y, Chen X and Shi J (2005). "Development of a Synchronized System for Continuous Acquisition and Analysis of Ultrasound Joint Angle, and EMG". Engineering in Medicine and Biology Society, IEEE-EMBS 2005. pp. 989 – 992.

[105] Loram ID, Maganaris CN and Lakie M (2004). "Paradoxical muscle movement in human standing". J Physiol. 556(Pt 3), pp. 683-689.

[106] Freivalds A (2004). "Biomechanics of the Upper Limbs". CRC Press. Ch 2,3,5.

[107] Brand and Hollister (1999). "Clinical Mechanics of the Hand". 3rd Edition. Mosby Inc.

[108] Agnihotri A, Purwar B, Jeebun N and Agnihotri S (2006). "Determination Of Sex By Hand Dimensions". The Internet Journal of Forensic Science. 1(2).

[109] Henry Gray (1918). "Gray's Anatomy". Philadelphia Lea and Febiger, 1918 edition.

[110] Wilkinson D, Weghe M and Matsuoka Y (2003). "An Extensor Mechanism for an Anatomical Robotic Hand". Proceedings of the 2003 IEEE International Conference on Robotics & Automation. 1, pp. 238- 243.

[111] Mcphee S. "Functional hand evaluations: a review. The American Journal of Occupational Therapy". 41(3), pp. 158-163.

[112] Panchal J, Mehdi S, Donoghue JO, O'Sullivan ST, O'Shaughnessy M, O'Connor TP (1997). "The range of excursion of flexor tendons in Zone V: a comparison of active vs passive flexion mobilisation regimes". J Plast Surg. 50(7), pp.517-522.

[113] Deshpande AD, Balasubramanian R, Lin R, Dellon B and Matsuoka Y (2008).
"Understanding variable moment arms for the index finger MCP joints through the ACT hand".Biomedical Robotics and Biomechatronics. 2nd IEEE RAS & EMBS International Conference. pp.776-782.

[114] Hagberg L and Selvik G (1991). "Tendon excursion and dehiscence during early controlled mobilization". J Hand Surg, 16A, pp. 669-680.

[115] Kremkau F (1995). "Doppler Ultrasound: Principles and Instruments". W.B. Saunders Company. 2 Sub Hardcover edition (January 1995).

[116] Evans D and McDicken W (2000). "Doppler Ultrasound: Physics, Instrumental, and Clinical Applications". Wiley. 2 edition (March 14, 2000).

[117] "The Physical Principles of Doppler and Spectral Analysis". Retrieved on July 3rd, 2009 at Internet URL: http://www.medana.unibas.ch/eng/tcd/tcd7.htm

[118] Hoskins P, Thrush A, Martin K and Whittingam T (2003). "Diagnostic Ultrasound: Physics and Equipment". Cambridge University Press, 2003. pp. 57.

[119] Hangiandreou N (2007). "AAPM/RSNA Physics Tutorial for Residents: Topics in US: B-mode US: Basic Concepts and New Technology". RadioGraphics. 23, pp. 1019 - 1033.

[120] Smith J (2007). "Mathematics of the DFT with audio Applications"., W3K Publishing. 2nd edition (April 13, 2007).

[121] Yamamoto M, Carrillo J, Insunza A, Mari G and Ville Y (2006). "Letters to the Editor: Error introduced into velocity measurements by innappropiate Doppler angle assignment". Ultrasound Obstet Gynecol. 28. pp. 853-858.

[122] Bundhoo V, Haslam E, Birch B and Park EJ (2009). "A shape memory alloy-based tendon-driven actuation system for biomimetic artificial fingers, part i: Design and evaluation". Robotica. 27(1), pp. 131-146.

[123] Koh S, Buford W Jr, Andersen C and Viegas S (2006). "Intrinsic Muscle Contribution to the Metacarpophalangeal Joint Flexion Moment of the Middle, Ring, and Small Fingers". The Journal of Hand Surgery. 31(7), pp. 1111-1117,

[124] Kamper DG and Rymer WZ (2001). "A biomechanical simulation of the effect of the extrinsic flexor muscles on finger joint flexion". Engineering in Medicine and Biology Society, 2001. Proceedings of the 23rd Annual International Conference of the IEEE. 2, pp. 1256- 1259.

[125] Zhang Y, Guo Z, Wang W, He S, Lee T and Loew M (2003). "A comparison of the wavelet and short-time fourier transforms for Doppler spectral analysis". Medical Engineering & Physics. 25(7) pp. 547-557.

[126] Wilson T, Zagzebski J, Varghese T, Chen Q and Rao M (2006). "The ultrasonix 500RP: A commercial ultrasound research interface". Ultrasonics, Ferroelectrics and Frequency Control, IEEE Transactions. 53(10), pp.1772-1782.